Three Dimensional Nanoarchitectures by Atomic Layer Deposition for Energy-Related Applications

By

Zhaodong Li

A dissertation submitted in partial fulfilment of

the requirements for the degree of

Doctor of Philosophy

(Materials Engineering)

at the

UNIVERSITY OF WISCONSIN-MADISON

2016

Date of final oral examination: 05/09/2016

The dissertation is approved by the following members of the Final Oral Committee:

Xudong Wang, Associate Professor, Materials Science and Engineering

Dane Morgan, Professor, Materials Science and Engineering

Padma Gopalan, Professor, Materials Science and Engineering

Zhenqiang Ma, Professor, Electrical and Computer Engineering

Zhiyong Cai, Project leader, Forest Products Laboratory

Abstract

Atomic layer deposition (ALD), which mainly stems from the drive of semiconductor industry, is a cyclic, multi-step thin film chemical vapor deposition process based on sequential self-limiting surface reactions. It produces high quality, pinhole-free, and conformal thin films on complex nanostructured surfaces with precise thickness control down to the atomic level. Therefore, it has been widely applied in the fabrication of various three dimensional (3D) nanoscale morphologies. Recently, based on the ALD technique, our group developed a surface-reaction-limited pulsed chemical vapor deposition (SPCVD) technique that operates at high temperature with extended cycling time. This technique is able to create 3D hierarchical branched nanowire (NW) architecture with super high surface area density (total surface area/projected substrate area >1000) and good electronic transport properties. This new ALD-based nanomanufacturing technique demonstrated great potential to conduct large-area and low-cost fabrication of high-density 3D nanomaterials for energy harvesting and storage applications, such as photoelectrochemical (PEC) water splitting, solar cells, batteries and supercapacitors.

In this dissertation, a series of experimental work is presented regarding fundamental understandings and rational controls of the SPCVD process in branched nanorod (NR) synthesis. Further application potentials of 3D branched nanowire architectures are also explored and studied. First, the doping strategy of SPCVD was studied on nitrogen-doped

titanium dioxide nanorods (N-doped TiO_2 NRs) by introducing TiN growth cycles to TiO_2 growth process. Nitrogen was successfully introduced into TiO_2 NRs and the doping concentration was found related to the TiN cycle ratio. N-doped TiO_2 NR branches exhibited tailored band structure demonstrating an obvious visible light PEC activity (chapter 2). Chapter 3 discusses further application of SPCVD TiO_2 NR growth on nature cellulose nanofibers (CNFs) template. The 3D TiO_2 NW/nanotube architecture exhibited superior performances on photo-induced water splitting with enhanced surface area and improved behavior on light absorption and charge transport. Based on the CNF template, I further applied ALD to create mesoporous TiO_2 3D nanostructure as PEC photoanode. By integrating the strong capillary property of CNF film, a capillary PEC process was developed by performing water oxidation reactions outside of the body of electrolyte with enhanced reaction kinetics and higher efficiency (Chapter 4). Pt nanoparticle catalyst was then introduced to the 3D TiO_2 photoelectode and successfully produced hydrogen via the capillary photocatalytic system (Chapter 5). At last, SPCVD was applied to the growth of high-density vanadium oxide (VO_x) NR branches on Si NW backbones. Such a 3D hierarchical VO_x/Si NW structure exhibited enhanced performance as a supercapacitor. These achievements open a new avenue of ALD for large-area, low-cost, and green fabrication of materials, which would be used in solar energy conversion and electrical energy storage.

Acknowledgements

The author wishes to express his most sincere and profound appreciation to his advisor Prof. Xudong Wang, for his relentless guidance, assistance, and consistent encouragement. The author enjoyed the study experience and obtained extensive knowledge on nanoscience and nanotechnology, as well as exceptional skill in designing and assembling vacuum systems.

Sincere thanks are also extended to the author's PhD committees, Professors Padma Gopalan, Zhenqiang Ma, Dane Morgan and Dr. Zhiyong Cai for their great instructions/guidance. Appreciation is also given to the author's current and previous group mates, Jian Shi, Fei Wang, Matthew Starr, Dalong Geng, Ping Zhao, Arthur Meinig, Yanhao Yu, Xin Yin, Yanchao Mao, Zheng Zhang, Chunhua Yao, Geoff McConohy, Christopher Coaty, Qi Zhang, Shaoyang Wang, Zhiqiang Zhang, Guoquan Suo, Hongxia Li, Weiguang Yang, Zhiyi Zhang, Bing Yang, Qinyi Chen, Douglas Fraser, Lazarus German, Yin Long, Xiaobo Chen, Peng Tian, and Chuan-Pu Liu for their great cooperation, kind assistance and helpful discussion. In addition, the author would like to thank all collaborators, Zhiyong Cai, Chunhua Yao, Zhenqiang Ma, Munho Kim, Qi Ding, Wenjie Li, Susmit Roy, Gerald Brady, Robert Jacobberger, Jialiang Wang, Padma Gopalan, Jon Choi, Paul Voyles, Alexander Kvit, Yizhang Zhai, Congli Sun, Sundaram Gunasekaran, Yi-Cheng Wang, Katherine Rice, for their great collaborations and kind help.

The author also wishes to thank his family, especially, his father, Shuobi Li and his mother, Mingzhu Shan, for their unlimited support and inspiration.

Lastly, the author gives thanks and praises to all those not mentioned above but who assisted and supported him in his four-year study at University of Wisconsin-Madison.

Table of Contents

List of Figures

List of Tables

Chapter 1. Introduction

1.1 ALD on Nanotechnology

Along with the development of nanotechnology and semiconductor industry miniaturization, the conventional film growth techniques such as chemical vapor deposition (CVD) and physical vapor deposition (PVD) have met unprecedented challenges to achieve high quality, pinhole-free thin film down to the atomic level. The relatively high deposition temperature (>300 °C) of CVD and different thermal expansion coefficients of materials lead to stresses in deposited films which cause the mechanical instabilities in the deposited films.[1,2] The line-of-sight deposition of PVD results in the poor ability on step coverage for complex nanostructures.[3,4] ALD is a novel film growth technique which realizes the precise thickness control and conformal coating of thin films. Therefore, it has been considered as a powerful technique on microelectronics, optical thin films, catalytic engineering, as well as nanotechnologies.[5-8]

The history of ALD could date back to 1970s. Tuomo Suntola and his co-workers in Finland first demonstrated a film growth process to obtain polycrystalline ZnS films from Zn and S element sources for thin film electroluminescent displays (TFEL).[9] Epitaxial growth was observed during the growth process, and it was therefore named as Atomic Layer Epitaxy (ALE).[10-14] A breakthrough of this technique occurred in 1980s when the inert gas reactors were introduced. This enabled the use of compound reactants like metal chlorides, hydrogen sulfide and water vapor for performing the ALE process, and the

application of this technique also spread into the areas of photovoltaic devices and heterogeneous catalysts.[15-17] Since the early 2000s, driven by the necessity of continuous and ultrathin films in complex semiconductor devices, the most ALE processes started to use sequential, self-limiting surface reactions where the films were no longer epitaxially grew to their underlying substrates. Moreover, amorphous films were preferred for insulation or passivation applications. Thus, such promising thin film technique began to be more comprehensive and was well known as ALD.[18]

The schematic in Figure 1.1 illustrates the ALD film formation mechanism. In most ALD cases, the binary reaction sequences are involved in the process. When precursor A exposes, it dissociatively chemisorbs on the substrate surface and excess free molecules are removed out of the chamber. Subsequently, the introduced precursor B reacts with the previous precursor layer on the substrate. Since the gaseous chemicals would not react until in touch with the finite number of surface sites, every step of the chemisorption of the two precursors is self-limiting. It thus proceeds in a sequential fashion to conformally construct the film by atomic layers "up" from the surface. Such ALD films exhibit unique features such as high quality, crack- and pinhole-free, where its thickness, the structural and chemical characteristics can be precisely controlled in the atomic scale. Nowadays, it has been a paradigm of new nanomanufacturing for next generation electronics, such as high dielectric constant gate layer in the metal–oxide–semiconductor field-effect transistor (MOSFET),[19] high quality dielectrics for dynamic random-access memory(DRAM),[20] passivation surface for electrochemical devices,[21-24] copper diffusion

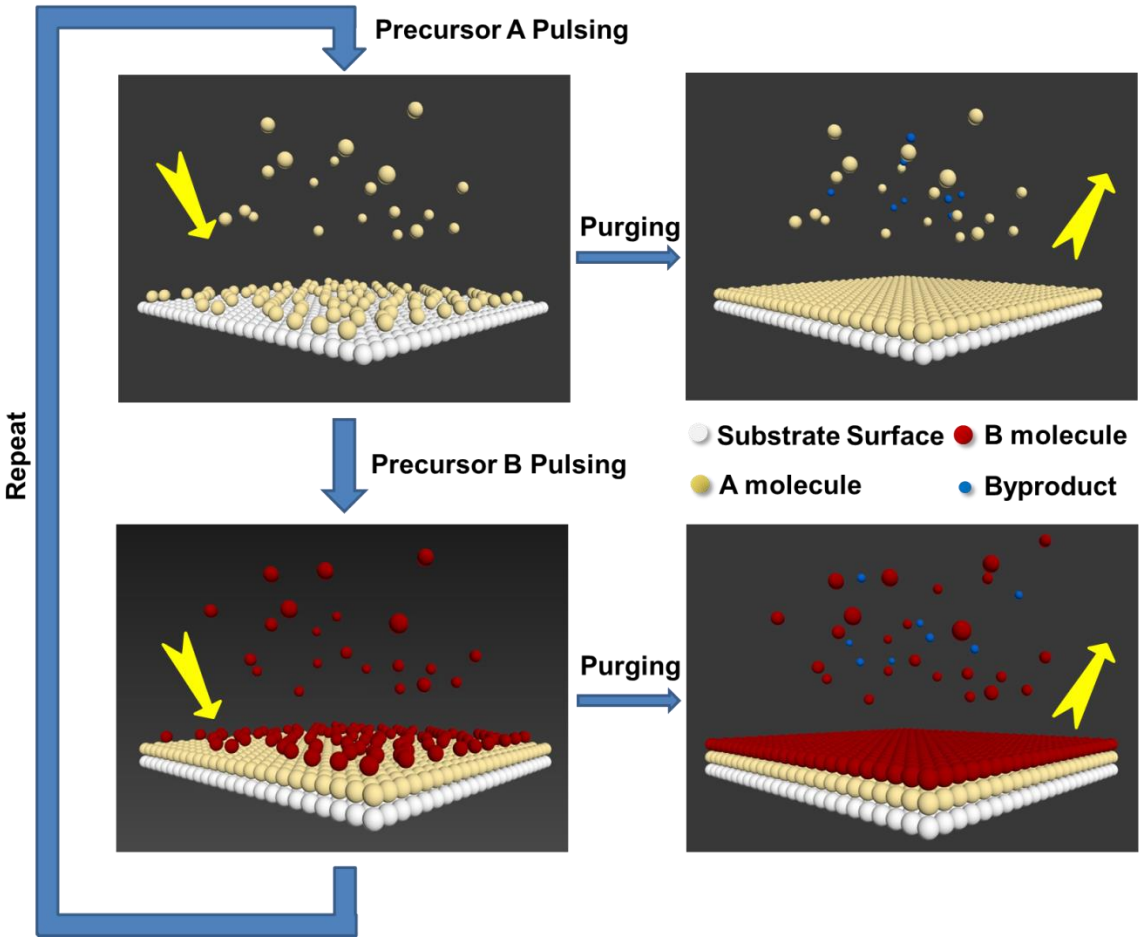

Figure 1.1. Schematic representation of ALD process using self-limiting surface chemistry and an AB binary reaction sequence.

barriers in backend interconnects,[18] and low electron leakage dielectrics for magnetic read/write heads.[25]

1.2 Application of ALD in Energy-Related Systems

Since the past decades, energy supply has become a more and more urgent issue over the world. Owing to the limitation of fossil fuel reserves as well as the increasingly serious pollution and greenhouse gases emission problem, developing green energy-related applications such as solar energy conversion devices and electrical energy storage devices holds great promises to tackle the energy crisis and global environment issue.[26] In the development of these energy-related devices, ALD stands out as an important nanomanufacturing technique owing to its unique film growth advantageous. For example, the ALD technique has performed attractive abilities on the developments of lithium-ion battery (LIB), supercapacitor, PEC cells, solar cell, and triboelectric nanogenerator.[27,28,29,21,30] Based on the relevancy to this thesis work, discussion here will be mostly focused on the applications of ALD in PEC electrodes and supercapacitor.

1.2.1 ALD on Photo-Induced Water Splitting Developments

Solar energy is experiencing explosive developments currently. By 2050, the total global photovoltaic (PV) capacity is estimated to provide 16% of the world's global electricity production, corresponding to 4600 gigawatts of cumulative installed PV capacity.[31] As an alternative solar energy harvesting approach, PEC water splitting is rapidly evolved in this decade and has motivated numerous efforts on studying and developing photoelectrode materials, interfaces and nanoscale architectures.[32-35] The

unique growth behavior and merits placed ALD among the leading fabrication tools for designing and creating high performance PEC electrodes. Generally, the applications of ALD in PEC water splitting include the aspects of active materials loading and surface modification.

The ALD for active materials loading stands on its unique nature of precise thickness control and conformal growth on complex nanostructures.[36] Materials including CdS, ZnS, CdSe, ZnSe, GaAs, ZnO, Ta_2O_5, $SrTiO_3$, and TiO_2 also have been successfully deposited by ALD for PEC electrode.[37,38] In order to develop a suitable ALD coating for high photoactive films, the influence of the film's microstructure properties on PEC performance of ALD TiO_2 films and was investigated (Figure 1.2). The TiO_2 films were grown by ALD at 200–500 ℃ using $TiCl_4$ and H_2O as precursors. Pure anatase phase was obtained at deposition temperatures below 400 ℃, whereas mixed phases of anatase and rutile were obtained at 500 ℃. The highest PEC performance was obtained from the anatase TiO_2 film with large grain size and low defect density.[39] Moreover, through taking the advantage of conformal coating capability by ALD, depositing photocatalytic thin films on highly-surface-area 3D nanostructured template is another common strategy to raise the PEC photocurrent density. A variety of highly conductive 3D "nanoskeletons" for ALD photocatalytic material coating have drawn much attention and been proved to improve the performance of PEC electrodes. For example, antimony-doped tin oxide (ATO) nanoparticle films,[29] indium tin oxide (ITO) NWs,[40] and Cl-doped ZnO NWs [35] were coated by ALD TiO_2 for PEC electrode (Figure 1.3). Si NWs and $TiSi_2$ nano-net

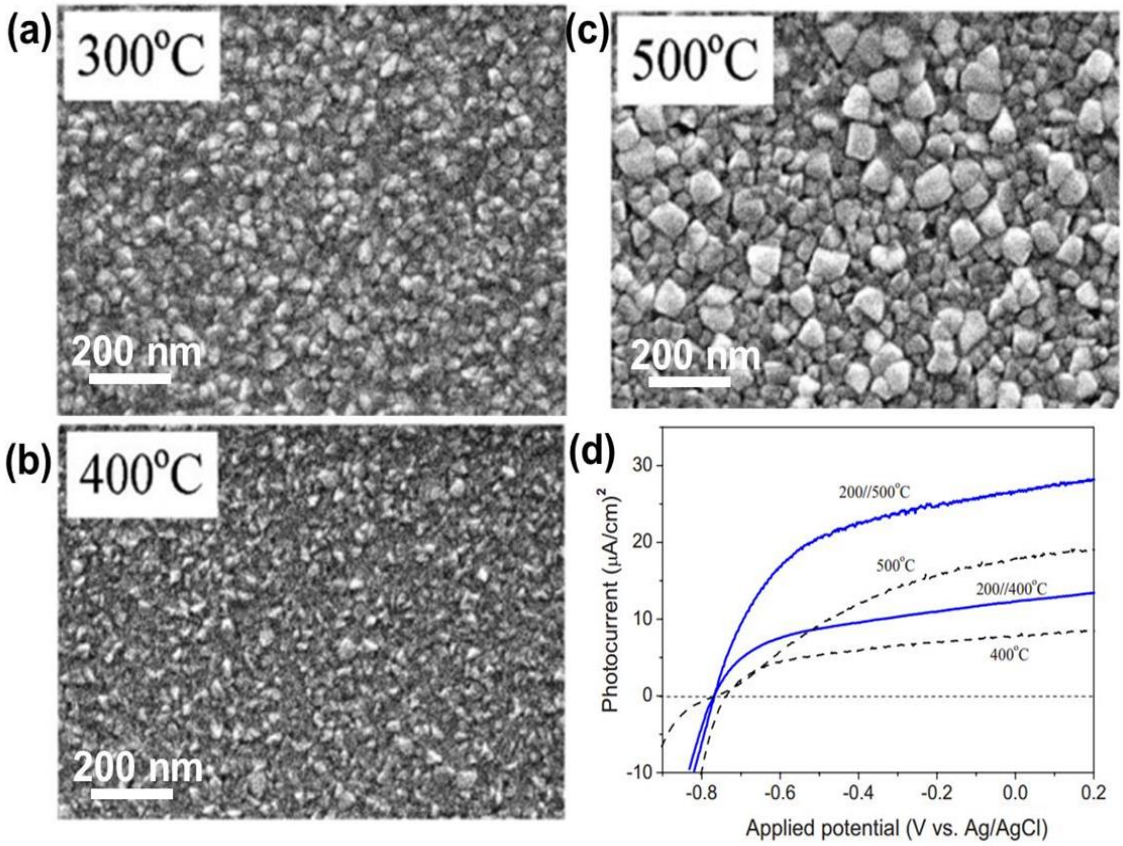

Figure 1.2. SEM images of TiO_2 films grown by ALD at (a) 300 ℃, (b) 400 ℃, and (c) 500 ℃. (d) *J*–*V* curves of two-stage-deposited TiO_2 films (solid blue lines). The 400 and 500 ℃ one-stage deposited films (dashed lines) are also shown for comparison.

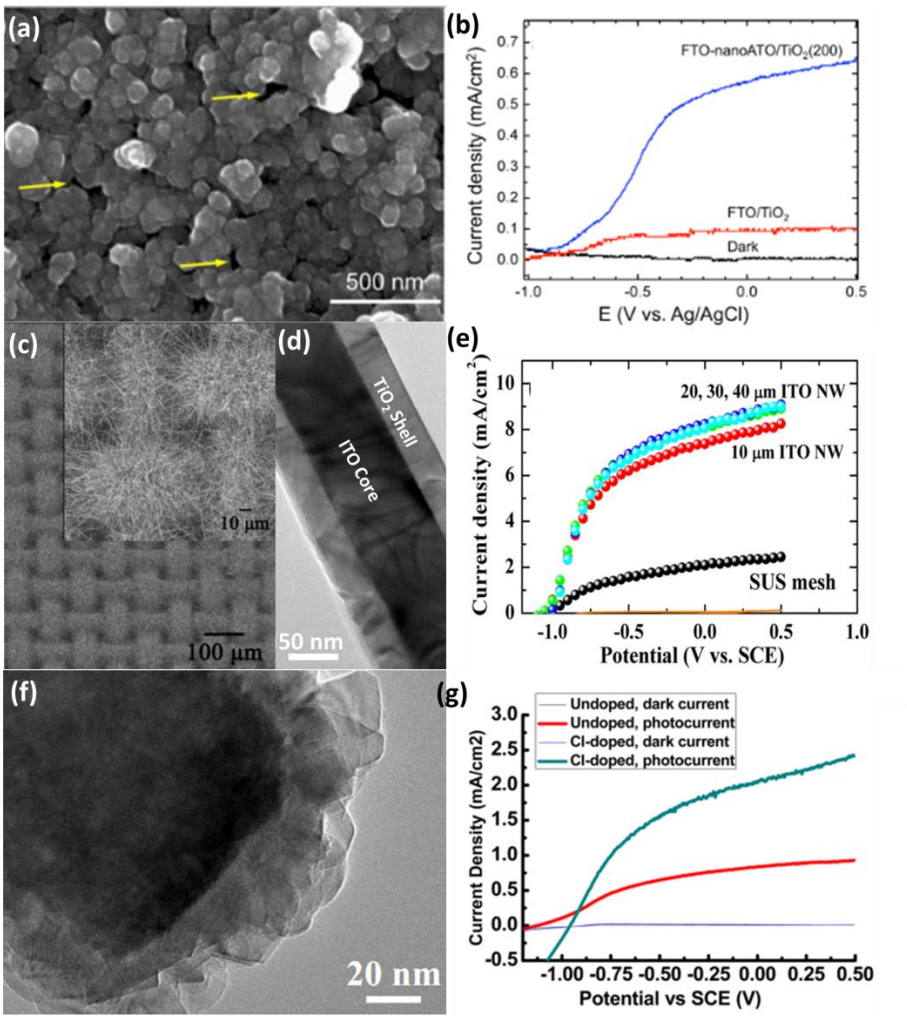

Figure 1.3. (a) NanoATO film with 600 cycles of TiO_2 ALD coating. (b) *J–V* characteristics of planar FTO/TiO_2 PEC electrode (red line) and FTO-nanoATO/TiO_2 electrodes (blue line), as well as the dark current curve (black line). (c) ITO NW arrays grown on a stainless steel mesh. (d) TEM image of an ITO core-TiO_2 shell NW. (e) *J–V* characteristics of the TiO_2/ITO core-shell NW photoanodes under different NW lengths. The orange curve is the dark currents of all the specimens. (f) TEM image of a Cl-doped ZnO NW fully coated with polycrystalline anatase TiO_2. (g)*J–V* characteristics of two photoanodes based on undoped and Cl-doped ZnO NW arrays.

were selected to coat Bi_2O_3 and Fe_2O_3 films for PEC applications, respectively.[41,42] Other than regular film coating, ALD also exhibits a powerful potential on tailoring the band structure of photoelectrode materials by periodically adding dopant cycles into the regular ALD growth cycles of the host material. Nitrogen-doped TiO_2 films and Mg doped Fe_2O_3 films have been produced by ALD, which demonstrated enhanced visible light activity and turn-on voltage reduction for enhanced PEC performance.[43,44]

Compared to the metal oxides which can be directly coated by ALD for PEC applications, narrow bandgap semiconductors (e.g. Si and III-V group of composites) are more promising candidates for constructing efficient photoelectrochemical electrodes for solar-driven H_2 production due to their effective light absorption and rapid charge separation.[45] The largest obstacle to practical solar-to-fuel conversion is their poor stability caused by the surface corrosion during the electrochemical reaction. One predominate strategy of alleviating this drawback is to protect the electrode surface with chemically-inert oxide thin films.[46-49] Among various deposition techniques, ALD can grow conformal and pinhole-free oxides with precisely controlled film thickness, which is critical for maximizing the protection performance. Thus, ALD is considered as one of the most suitable techniques for growing the electrode protective layers. As shown in Figure 1.4, by ALD depositing 2 nm-thick polycrystalline TiO_2 as the protective layer, the silicon (Si) photoanode achieved 8 hours stability in 1M alkaline solution. Such stability was further extended to more than 2200 hours with a 94 nm ALD amorphous TiO_2 overcoating on Si microwires.[50] This discovery of the protective ALD TiO_2 notably

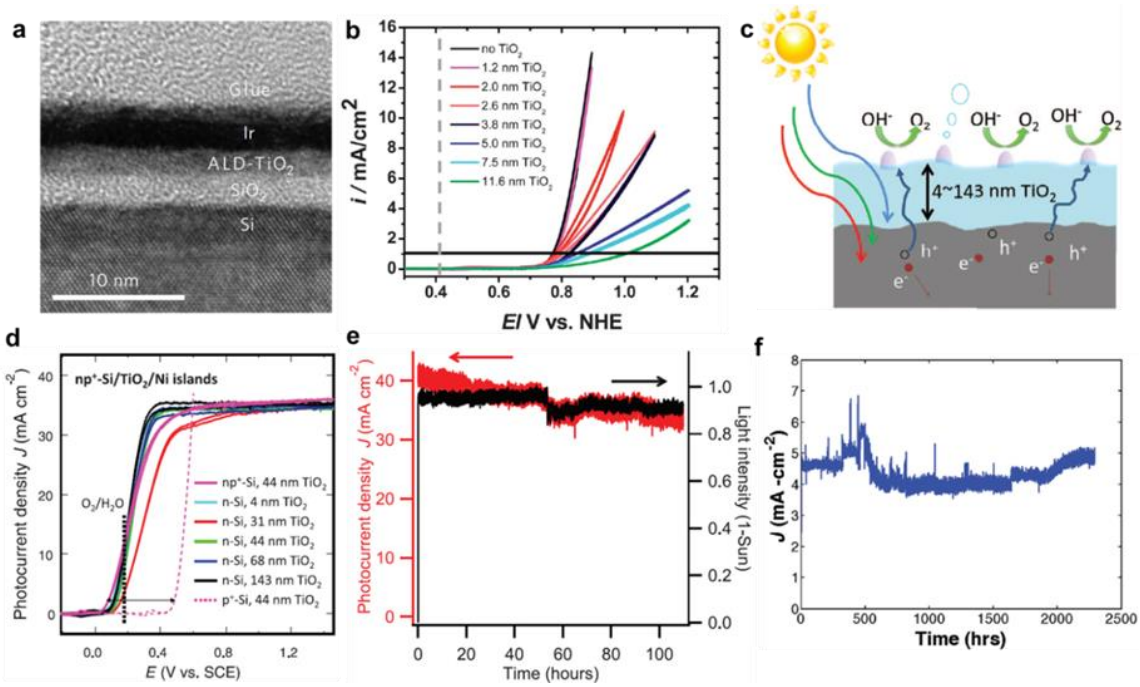

Figure 1.4. (a) Cross-sectional TEM image of the polycrystalline TiO_2 protected silicon photoanode. (b) *J-V* curves of the Ir/TiO_2/SiO_2/p^+-Si photoanodes with a series of TiO_2 thicknesses. (c) Schematic of a photoanode stabilized by a thick electronically defective layer of amorphous TiO_2 deposited by ALD. (d) *J-V* curves of Si photoanodes coated with protective TiO_2 with various thicknesses. (e) Chronoamperometry of a np^+-Si photoanode coated with 44 nm TiO_2 and Ni islands for over 100 hours in 1.0 M KOH at a constant bias of 0.93 V versus SCE. (f) Photourrent density versus time plot for a np^+-Si /TiO_2/$NiCrO_x$ microwire-array photoanode under 1 Sun illumination in 1.0 M KOH at a constant bias of 0.36 V vs. $E^{O'}(OH^-/O_2)$.

accelerated the evolution of PEC photoelectrodes and will be a great milestone in the solar fuel production development.

1.2.2 ALD on Supercapacitor Developments

As one of the most promising strategies for next generation energy storage, electrochemical supercapacitor has received considerable attention owing to its high-power density, fast charging/discharging, excellent cycling stability, and low maintenance. Generally, high-capacitance electrode materials possess a high surface area and good electrical conductivity since these properties are strongly related to the electrochemical double layer capacitance or electroactive surface for redox-reactions, resulting in pseudocapacitance within an electrode.[51-53] Therefore, a feasible synthesis method is required to produce the supercapacitor electrode with superior geometric structure, adequate charge transport properties, as well as suitable thickness and surface chemical properties. Owing to the unique processing merits, ALD is particularly useful for the development of supercapacitors, whose performance heavily relies on their macro-/nano-scale structures and surface properties.

Owing to the extraordinary capability of conformal and pinhole-free coating management, ALD has been increasingly used for directly depositing active materials on nanostructured templates for supercapacitor electrode fabrication.[54-56] The high quality ALD films are essential for controlling ion intercalation and diffusion into the bulk electrodes to achieve high capacity.[51,57] Free-standing carbon nanotube (CNT) thin films and graphene are the most commonly used ALD template for high-power supercapacitor

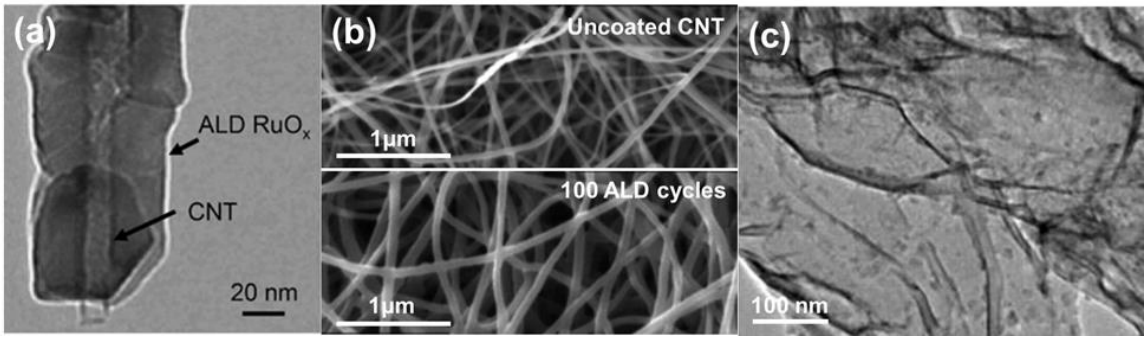

Figure 1.5. (a) TEM image of a RuO_x-coated CNT. (b) SEM images of uncoated CNTs (top), and CNTs coated with VO_x by 100 ALD cycles (bottom). (c) TEM image of TiO_2-Graphite composite.

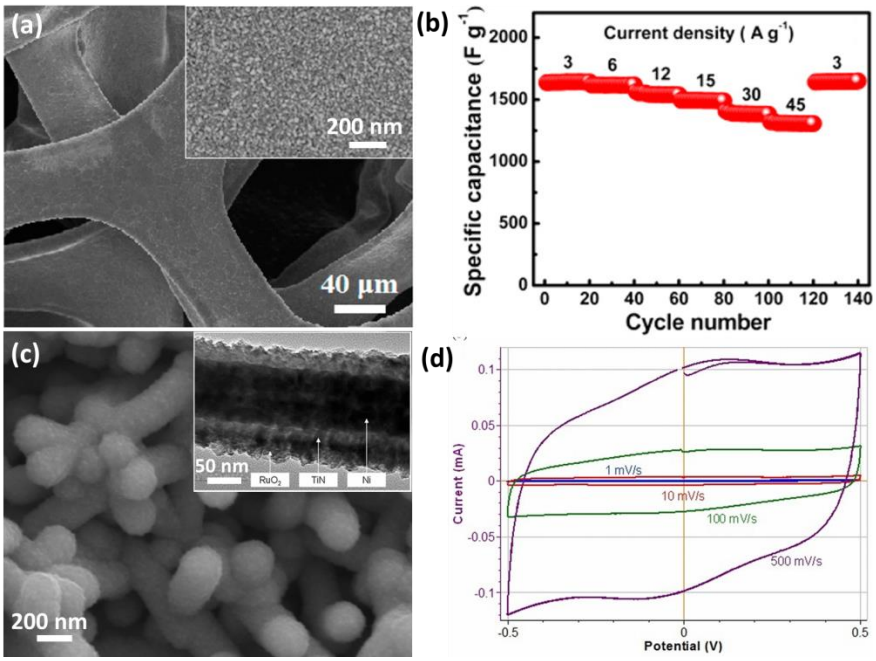

Figure 1.6. (a) SEM image of Co_9S_8/Nickel Foam electrode. Inset shows the polycrystalline Co_9S_8 film surface on nickel. (b) Rate performance of Co_9S_8/NF at sequentially varied current density. (c) SEM image of TiN and RuO_2 deposited by ALD on TMV-1Cys templated nickel. Inset is a TEM image revealing the multilayer structure of TMV-1Cys/Ni/TiN/RuO_2. (d) C-V measurement at different scan rates.

development due to their high porosity and excellent electrical and thermal conductivity.[58-61] In order to achieve conformal ALD coating, the carbon surfaces typically need to be acid treated to improve their affinity to ALD precursors. The metal oxides, such as RuO_2, VO_x, and TiO_2, were then overcoated for supercapacitor electrodes (Figure 1.5).[55,56,27,62] In addition to carbon-based materials, metal microstructures and nanostructured biotemplate, such as nickel foam and cysteine modified tobacco mosaic virus, were also used as ALD templates for supercapacitor development. The subsequent Co_9S_8 and RuO_2 thin films coating respectively led to the high stability of the as-synthesized supercapacitor electrodes due to the good crystallinity, high purity, and low surface roughness of the films (Figure 1.6).[54,63]

In supercapacitor electrode design and fabrication, a sacrificial layer could be introduced under the active material layer to create a promising disconnected core/shell or hollow nanostructure. After chemically or thermally removing the sacrificial layer, the nanoscale gap left in the structure could significantly enlarge the reaction area and facilitate the electrolyte contact with the active material. The open space could also effectively buffer the strain generated during the fast charge-discharge process, and thus the out layer in this structure preserved the structure integrity after long-time cycling reactions.

Since the sacrificial layer typically has very small thickness and requires high uniformity, ALD becomes the most suitable approach to realizing such hierarchical structures. The ALD coating of Al_2O_3 sacrificial layer has been reported for

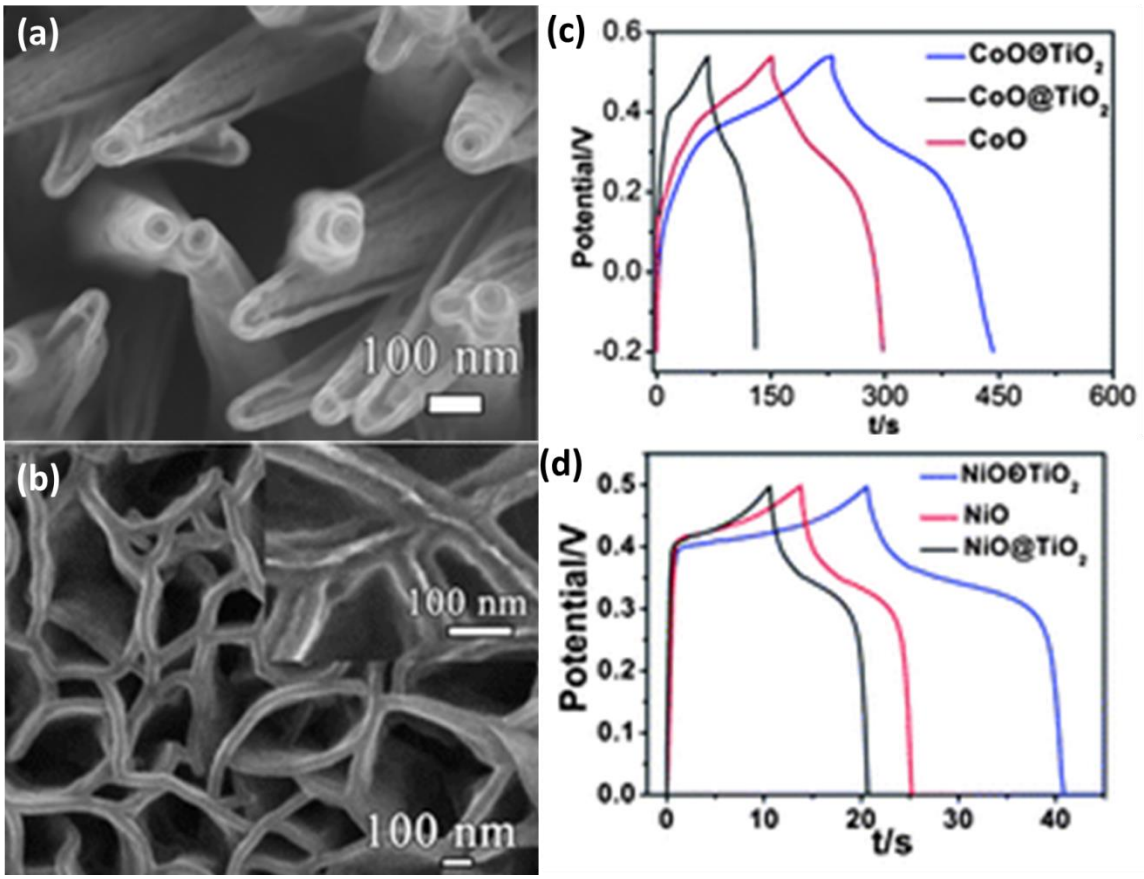

Figure 1.7. SEM images of CoO nanorods (a) and NiO nanowalls (b) enclosed by a TiO_2 shell. (c, d) Charge/discharge curve of the (c) TiO_2/CoO nanorods, and (d) TiO_2/NiO nanowalls. The charge/discharge curves of the solid core-shell structures and bare nanorod or nanowall structures are also shown for comparison.

supercapacitor electrode development.[64] The surface of CoO nanorods and NiO nanowalls were sequentially covered with Al_2O_3 and TiO_2 layer by ALD. After chemical etching the Al_2O_3 layer in alkaline solution, the CoO nanorods and NiO nanowalls were enclosed by a TiO_2 shell (Figure 1.7). Compared to the solid core-shell structures and bare nanorod or nanowall structures, such structures exhibited ~2 to 4 times higher capacitance, which was attributed to the enlarged specific surface areas and a shorter ion transport path between the disconnected core and shell materials.

1.3 Surface-Reaction-Limited Pulsed Chemical Vapor Deposition (SPCVD)

Based on the discussions in the previous part, the 3D NW network is an emerging and promising architecture that features an extremely large surface area, efficient optical/ion diffusion path, as well as tunable electronic properties. These merits make 3D NW architecture exceptionally advantageous for the photo-induced water splitting systems and electrochemical energy storage systems, whose performances are dependent on surface reactions and bulk charge transportation.[65-69] Synthesizing such a unique hierarchical nano-architecture faces a critical challenge – the coupling between the crystal growth rate and the precursor concentration, which always leads to large size variations inside narrow spaces. This challenge is intrinsic to almost all NW synthesis approaches, regardless of the phase of precursors. Recently, Shi *et al.* developed a SPCVD technique as a derivative of ALD.[70] By mimicking the self-limited growth mechanism of ALD, SPCVD uses separated precursor pulses and high deposition temperature (600 ℃). It effectively decouples the crystal growth from precursor

concentration while retaining anisotropic 1D growth. Through this technique, TiO_2 NRs can be grown on a variety of surfaces inside confined spaces. As indicated in Figure 1.8, branched TiO_2 NRs were uniformly grown among different dense and deep material matrixes, such as anodic aluminum oxide (AAO) nanochannels, Si NW arrays, and inverse opal structures.[34,70] The as-synthesized 3D TiO_2 NR architectures offered a roughness factor of 3000, which is nearly ten times higher than that of typical NW arrays.

Moreover, in order to achieve rational control of 3D NR growth, atomic-level observations was arranged to study the crystal nucleation and growth of TiO_2 at different stages of SPCVD process.[71] By applying aberration-corrected scanning transmission electron microscopy (STEM) and transmission electron microscopy (TEM) characterizations, evolution of TiO_2 nanostructures in ALD was found following a path from amorphous layers to amorphous particles to metastable crystallites and ultimately to stable crystalline forms, where the Ostwald−Lussac law was the governing rule in high-temperature TiO_2 ALD nanostructures (Figure 1.9 a-d). The amorphous−crystalline mixture was also observed to enable a unique anisotropic crystal growth behavior at high temperature forming TiO_2 NR via the principle of vapor-phase oriented attachment (Figure 1.9 e-h).[71,72] Such comprehensive understandings of SPCVD growth provided a feasible way for achieving morphology, crystal structure, and property control, as well as deposition manipulation and scaling in fabricating energy-related devices. The SPCVD

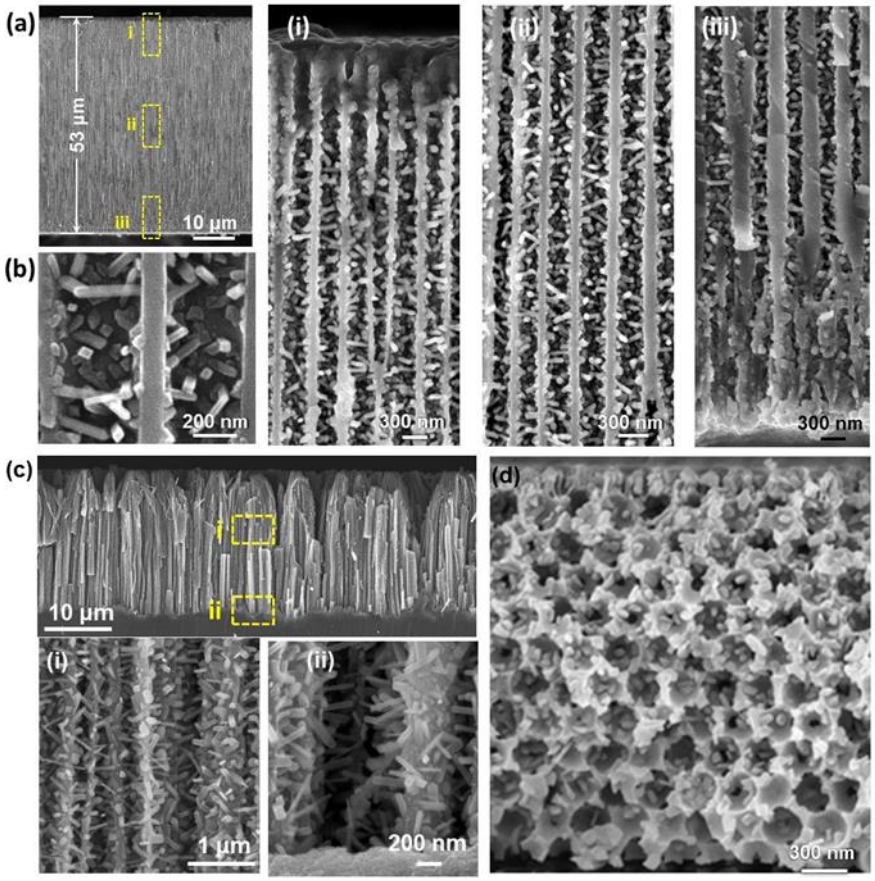

Figure 1.8. (a) The uniform and dense coating of SPCVD TiO_2 NRs inside the AAO channels at the top (i), middle (ii), and bottom (iii) sections. (b) Higher magnification SEM of TiO_2 NRs rooted on the walls of AAO channels. (c) SPCVD TiO_2 NRs on 25µm long Si NWs. (d) SPCVD of TiO_2 NRs inside inverse opal.

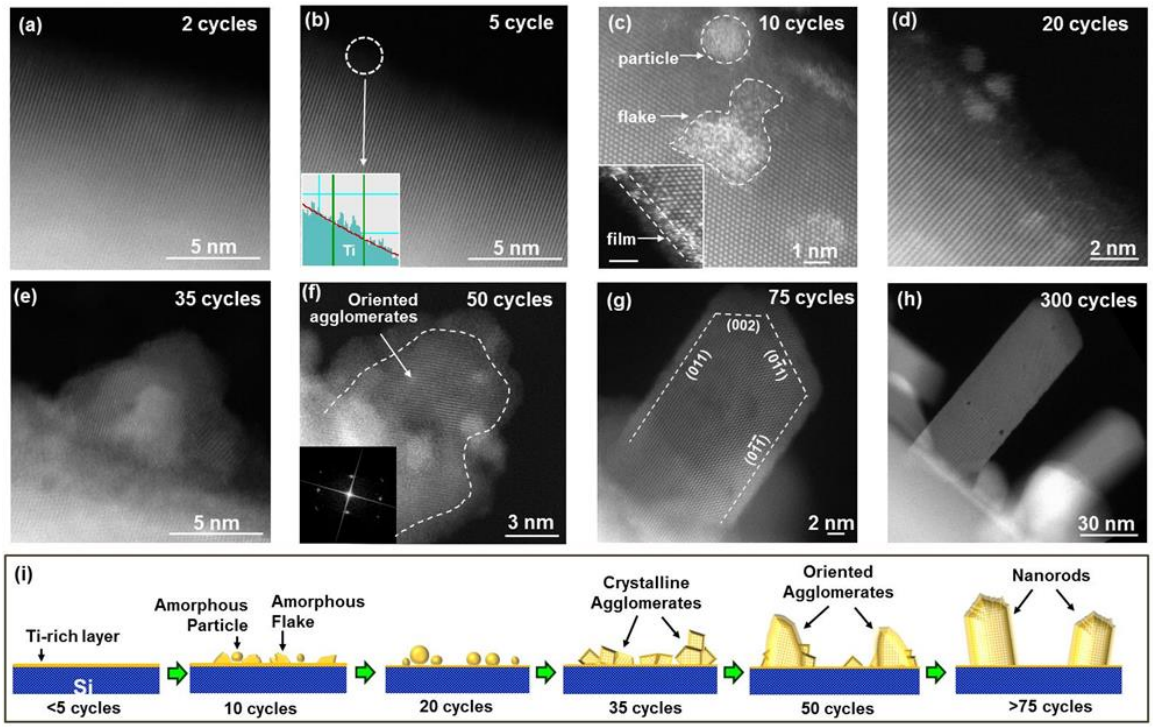

Figure 1.9. Evolution of TiO_2 NRs at different ALD cycles at 600 ℃. (a-h) STEM image of TiO_2 on Si surface after 2, 5, 10, 20, 35, 50, 75 and 300 cycle growth, respectively. Inset of (b): EELS analysis on 5 cycle sample detected the existence of Ti. Inset of (c) shows the amorphous ultrathin TiO_x layer coated on NW substrate (scale bar is 1 nm). Inset of (f) is the FFT pattern converted from lattice image. (i) Schematic illustration the entire evolution process of TiO_2 NRs. Scale bars are 5 nm unless otherwise noted.

has realized the large-area, low-cost and simple fabrication of 3D nanomaterials for PEC applications.[34,72]

By using the TiO_2-Si heterogeneous 3D NW architecture, Shi *et al.* demonstrated the capability of this SPCVD technique for PEC water splitting application.[34] As shown in Figure 1.10a, when this heterogeneous structure was used as a PEC anode for water splitting, photocatalyzed H_2O oxidation reactions only occurred on the TiO_2 surfaces. The photogenerated electrons would quickly transport through the Si NW backbone and reach the counter electrode with minimal losses owing to the high conductivity of Si NWs and isolation from electrolyte. The very large surface area provided by the TiO_2 NR arrays together with the high-speed electron transport channels provided by the Si NWs are promising features that could lead to a significant improvement of the PEC efficiency (Figure 1.10b). This result suggests that implementing 3D NW networks into electrode design could advantageously impact the performance of PEC and photovoltaic devices.

Besides the Si NW arrays, SPCVD of TiO_2 NRs was also applied on ZnO NW backbones, which is shown in Figure 1.10c. Under high deposition temperature, ZnO NWs was found to interact with $TiCl_4$ precursor vapor and were quickly converted into polycrystalline TiO_2 tubes following the Kirkendall effect.[73] The evolution of TiO_2 nanotubes from ZnO NW scaffolds was seamlessly integrated with TiO_2 NR branch growth and thus realized a pure TiO_2-phased 3D NW architecture. Because of the significantly enlarged surface area and the trace amount of Zn left in the TiO_2 crystals,

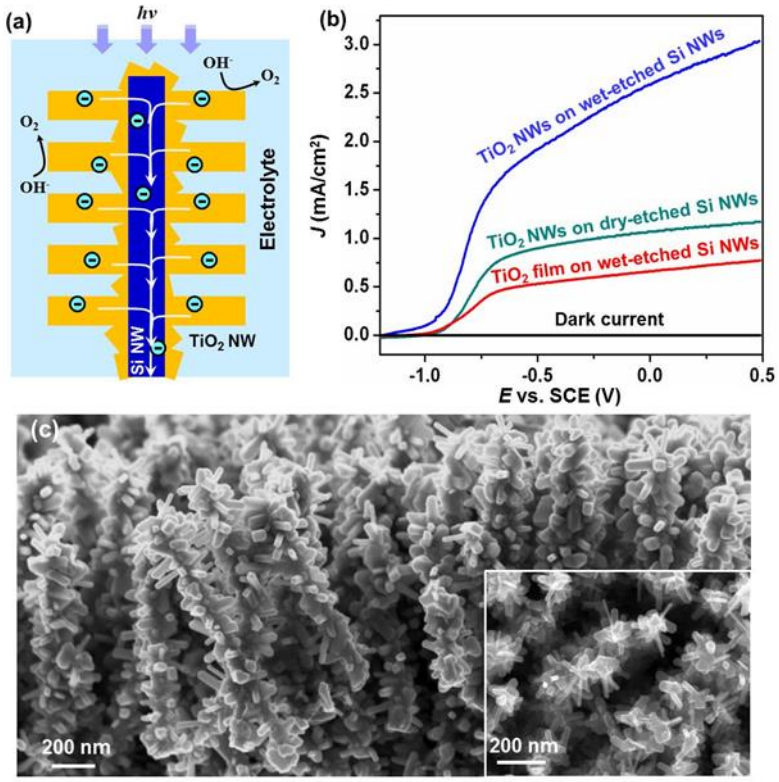

Figure 1.10. (a) Schematic illustration of using TiO_2-Si NW structure as PEC anode for water splitting. (b) *J-V* curves of different TiO_2-Si configurations showing enhanced PEC performance by introducing high-density TiO_2 NR branches. (c) Cross-sectional SEM image of a 3D TiO_2 nanoforest formed on ZnO NWs. Inset is the top view.

such 3D TiO_2 nanoforests demonstrated enhanced photoelectrochemical performance particularly under AM (air mass) 1.5G illumination.

1.4 Summary of Research in This Thesis

Owing to the fantastic ability of ALD and SPCVD techniques for multiple 3D nanoarchitectures, as well as their achievements on efficient energy harvesting and storage applications, in this dissertation, fundamental understandings and rational controls of the SPCVD process in branched nanorod (NR) synthesis is illustrated by a series of experimental work. Further application potentials of 3D branched nanowire architectures are also explored and studied. Specially, in Chapter 2, the SPCVD technique was manipulated for high-density doped metal oxide NR branches through mimicking the ALD doping process. The nitrogen doped 3D TiO_2 NR architecture was synthesized by introducing both TiN and TiO_2 growth cycles during the SPCVD process, which tailored the band structure of TiO_2, demonstrating an obvious visible light PEC activity. Moreover, the nature cellulose nanofibers (CNFs) were chosen as the template, and the SPCVD TiO_2 NR growth was applied for 3D TiO_2 NW/nanotube architecture (Chapter 3). This architecture exhibited superior performances on photo-induced water splitting with enhanced surface area and improved behavior on light absorption and charge transport. Based on the CNF template, as shown in Chapter 4, the mesoporous TiO_2 3D nanostructure was further synthesized by ALD for PEC application. By integrating the strong capillary property of CNF film, a capillary PEC process was developed by performing water oxidation reactions outside of the body of electrolyte with enhanced

reaction kinetics and higher efficiency. In Chapter 5, Pt nanoparticle catalyst was then introduced to the 3D TiO_2 photoelectode and successfully produced hydrogen via the capillary photocatalytic system. At last in Chapter 6, SPCVD was applied to the growth of high-density VO_x NR branches on Si NW backbones. Such a 3D hierarchical VO_x/Si NW structure exhibited enhanced performance as a supercapacitor.

Chapter 2. Nitrogen Doped 3D TiO_2 Nanorods Architecture with Photoactivity in Visible Light Regime

2.1. Introduction

TiO_2 has been a widely used semiconductor for environmental remediation, hydrogen generation, and solar energy harvesting since its intriguing discovery of the photocatalytic properties on TiO_2 in early 1970s.[74,75,34,76,77,72,78] One critical limitation of its application in solar energy harvesting is its large bandgap (~3.0-3.2 eV) which excludes it from absorbing the majority of solar energy within the visible light range.[72,79,43] Tailoring the band structure of TiO_2 by doping has been broadly investigated as a common strategy to address this challenge.[79,80,81,82]

Anion doping (e.g., C, S, N, F, B, and P) have been intensively studied as an effective approach to narrow the bandgap by introducing new *p*-states near the valence band or hybridizing the O 2*p* states to lift the valence band edge.[75,83-91] Among all the anion candidates, nitrogen is a promising dopant due to its comparable atomic size with oxygen, small ionization energy, and good stability.[92,93] Nitrogen-doped TiO_2 has been created via a variety of methods and demonstrated efficient visible light absorption up to 600 nm,[85] which largely enhanced photoelectrochemical water splitting performance,[94] and suppressed the reduction of I_3^- on the TiO_2 electrode in dye-sensitized solar cells (DSSC).[95] Incorporating cations, such as V, Cr, Mn, Fe, and Ni, into the TiO_2 lattice has also been found practical for band gap narrowing.[96,97] The transition metal dopants can

introduce intraband discrete states near the edges of conduction band (CB) or valence band (VB), leading to visible light absorption with sub-band gap energies.[93,98,99] In addition, hydrogen has also been found as an effective dopant that enabled visible and infrared light absorption in TiO_2. The dopant induced a highly disordered layer on the nanocrystals surface, which yields mid-gap states for optical excitation/relaxation and provides trapping sites for photoexcited charges to reduce rapid recombination.[100] In order to circumvent the impurity-related charge separation and transport issue found in single element doped TiO_2,[96,101] a donor-acceptor co-doping method has been proposed. For example, density functional theory calculations suggested that (W,C), (Mo,C), (Ta,N), (Nb,N), (W,2N), and (Mo,2N) donor-acceptor pairs are good codoping candidates, which can shift both CB and VB edges of TiO_2 and significant narrow its band gap.[32,79,102] Nevertheless, only a few successful developments were reported on co-doped TiO_2 due to the complexity in element and crystal structure control during the synthesis.[79] So far, various solution-based, vapor-based and ex-situ growth techniques have been applied to the synthesis of doped TiO_2 nanostructures. However, how to control dopant concentration and distribution and how the doping elements influence the morphology and crystal structure of the host materials are inadequately understood. Such understandings are particularly critical for engineering the properties of TiO_2 nanostructures, and thereby further advance the performance of TiO_2-nanomaterials-based solar energy harvesters.[43,79,81,85-89]

Among all TiO_2 nanostructure growth techniques, SPCVD is a powerful 1D

nanostructure growth technique. It mimics the process of ALD and offers a unique capability for growing high-density nanorod (NR) branches inside highly-confined spaces. Several important growth phenomena in this anisotropic crystal growth process have been revealed for morphology and composition evaluation. However, how to intentionally dope the NRs through this process is still unexplored, though it is a critical aspect for controlling the electronic properties and improving the performance.

In this chapter, we start the fundamental understandings and rational controls of the SPCVD process in branched nanorod (NR) synthesis on optimizing TiO_2 band gap to overcome its intrinsic constrain for visible light absorption. High-density nitrogen doped TiO_2 NR branches with controlled doping concentrations on dense Si NW forest was successfully synthesized by SPCVD technique. Nitrogen doping was achieved by introducing designed number of TiN cycles to TiO_2 growth cycles. Microscopic studies were performed to reveal the influence of Nitrogen dopant to the crystal growth behavior and NR morphology, as well as the elements distribution inside the lattices. We also demonstrated that the Nitrogen doping lowered the bandgap of TiO_2 NRs and effectively activated PEC reactions in the visible light range.

2.2. Experimental Section

Synthesis of Nitrogen Doped TiO_2 Branched NRs Architecture: Highly orientated Si NWs arrays were fabricated on n-type Si wafer by the reported metal assisted electroless chemical etching method.[34] The etchant solution was a 40 mL mixture of 0.02 M $AgNO_3$ and 5 M HF. The Si NWs arrays were cleaned by DI water and dried by N_2 gas, and then

transferred into our home-built ALD reaction chamber. In the SPCVD process for synthesizing Nitrogen doped TiO_2 NRs branches, deposition cycle ratio of the NH_3:H_2O (*X:Y*) increased from 1:80 to 1:1 to achieve different N concentrations (A2-A7). The undoped TiO_2 NRs branches (A1) for comparison were prepared by the same SPCVD process with only $TiCl_4/H_2O$ cycles. The total number of $TiCl_4/H_2O$ cycles for each sample (A1-A7) was kept at 400.

Compositions and structures characterizations: X-ray photoelectron spectroscopy (Thermo Fisher Scientific Inc. Waltham, MA) was applied to characterize the chemical compositions of all Nitrogen doped TiO_2 NR samples. The survey binding energy range is from 0 to 1350 eV. The N 1s, O 1s, and Ti 2p spectra were measured for characterizing the dopant concentrations and chemical structure variations. The density of states (DOS) of the valence band maximum profile was also characterized by the X-ray photoelectron spectroscopy (XPS) spectra. Both TEM and EELS combined with STEM were performed on highly doped sample A6 and lightly doped sample A2. EDS analysis was conducted during SEM analysis.

Photoanode Setup and Photoactivity Characterizations: All Nitrogen doped and undoped TiO_2 NR samples were immersed into the dilute HF and HCl to remove the oxidized Si and contaminations on the surface. Then 200-cycle of ALD anatase TiO_2 overcoating was conducted at 300 ℃ to protect the entire sample surfaces. These samples were then covered by epoxy leaving an average exposed active area of ~0.22 mm^2 as the photoanodes. PEC characterizations were performed in 1 mol L^{-1} KOH (pH=14) aqueous

solution using a three-electrode electrochemical cell configuration. A saturated calomel electrode (SCE) was used as the reference electrode and a Pt wire was used as the counter electrode. All electrodes were connected to a potentiostat system (Metrohm Inc., Riverview, FL) for *J–V* measurement. Light illumination was provided by a 150 W Xe arc lamp (Newport Corporation, Irvine, CA) and the intensity at the PEC anode position was adjusted to be 100 mW cm^{-2}. An AM 1.5G filter and a UV cut off filter were also utilized with the lamp for PEC characterizations. A monochrometer was used on Xe lamp source to obtain the monochromatic illuminations for IPCE characterizations with the wavelength ranging from 300 to 700 nm. UV-Vis absorption spectra were measured by a UV/Vis/NIR spectrometer (Jasco, Easton, MD) within the wavelength range of 300-700 nm.

2.3. Results and discussion

Figures 2.1a and b show a typical morphology of as-synthesized Nitrogen doped TiO_2 NRs on Si NW hierarchical structures measured by scanning electron microscopy (SEM). The top-view image presents dense Nitrogen doped TiO_2 NRs branching from Si NW bundles and protruding outward radially (Figure. 2.1a). Higher magnification image reveals the approximate dimensions of the as-fabricated NRs were ~130 nm in length and ~25 nm in diameter (inset of Figure 2.1a). Same as the regular SPCVD result, the TiO_2 NRs were uniformly distributed along the entire side surfaces of the Si NWs that were 12 μm in length and only ~100-200 nm apart from each other (Figure 2.1b). The zoom-in view clearly shows TiO_2 NRs had the rectangular prism shape, which were all rooted on

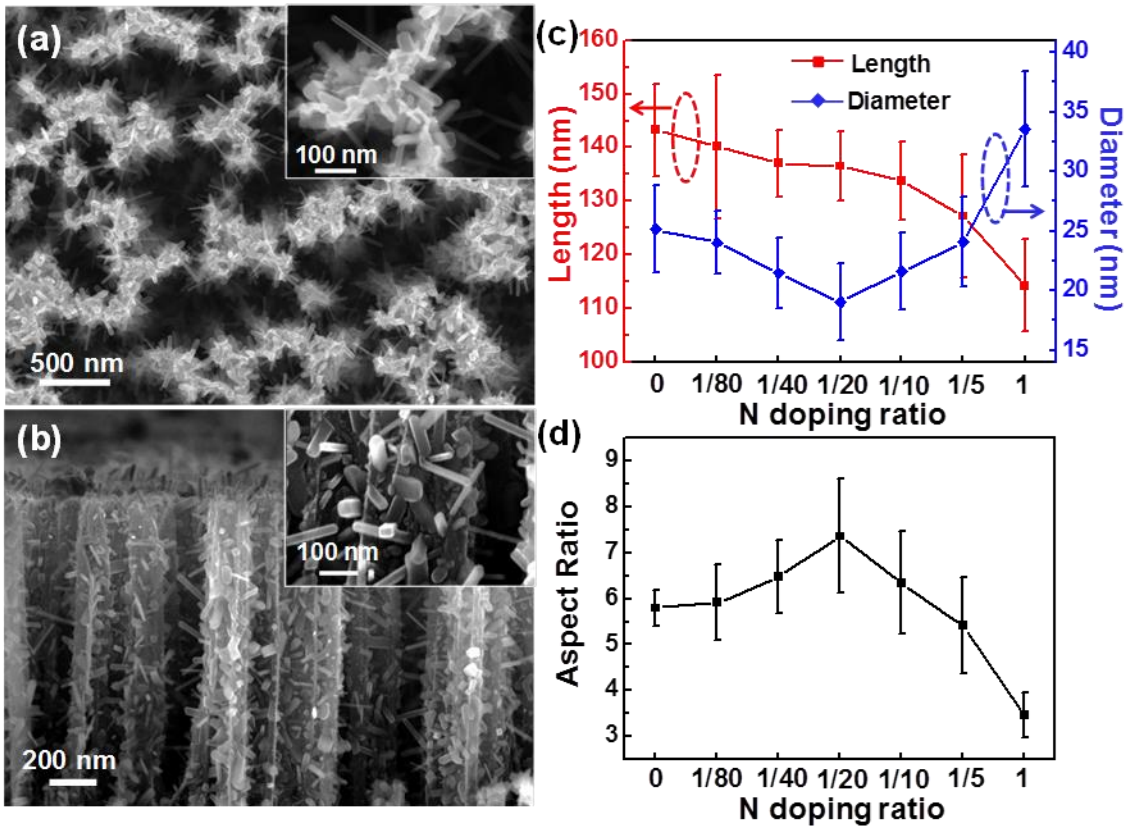

Figure 2.1. Top view (a) and Cross-section view (b) of high-density Nitrogen doped TiO_2 NRs on Si NW arrays. Insets are higher magnification SEM images showing the morphology of Nitrogen doped TiO_2 NRs branches. (c) Plots of NR length (square symbol) and diameter (diamond symbol) as a function of Nitrogen doping ratio. (d) Plots of aspect ratio of NRs as a function of Nitrogen doping ratio.

the Si surfaces (inset of Figure 2.1b).

The average N concentrations were initially quantified by energy-dispersive X-ray spectroscopy (EDS). N signal was observed from all Nitrogen doped samples (Figure 2.2a and inset) but absent from the undoped one (Figure 2.2b and inset). Table 2.1 summarizes the amounts of N dopant in corresponding to the doping ratio, which were control by the ratio of NH_3 cycle to H_2O cycle (*X:Y*). It showed a very good correlation between N traces and expected level of nitrogen doping. In particular, A6 (*X:Y*=1:5) had the highest N doping concentration (~2.28%) while A2 (*X:Y*=1:80) only had 0.82% N. Sample A7 (*X:Y*=1:1) exhibited a slightly lower N concentration compared to A6, although it had the most NH_3 cycles. This is possibly because that too high NH_3 precursor ratio might lead to more TiN growth cycles, which typically reduces the incorporation rate of N elements into the lattice.[103]

The Nitrogen doping effect to the TiO_2 NR morphology was investigated from samples grown under different doping ratios (Figures 2.3). Samples A1-A7 represent undoped (A1) and doped TiO_2 NRs (A2-A7) with six *X:Y* values of 1:80, 1:40, 1:20, 1:10, 1:5, and 1:1, respectively. The lengths and widths of NRs in all the samples were measured via a statistical sampling method[104] and shown in Figure 2.1c. In general, the length of NRs slightly decreased from 143 ± 9 nm (the undoped NRs) to 137 ± 7 nm when the NH_3 cycle ratio was increased to 1:20 (sample A4). Meanwhile, the average diameter of the NRs monotonically decreased from 25 ± 4 nm (A1) to 19 ± 3 nm (A4). When the NH_3 cycle ratio was further increased from 1:20 to 1:1, a large decrease of NR

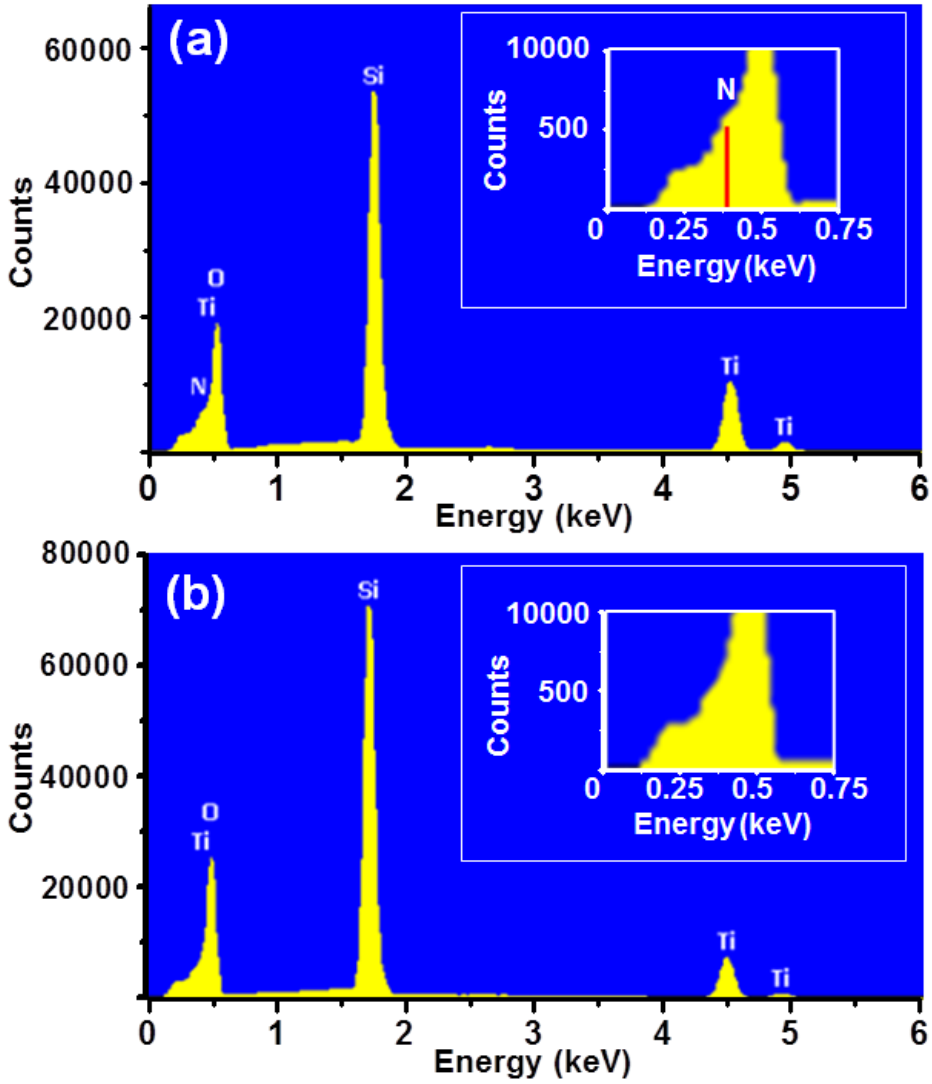

Figure 2.2. EDS spectra of Nitrogen doped (a) and undoped (b) TiO_2 NRs on Si NW array. N was detected in doped samples but absent in undoped one.

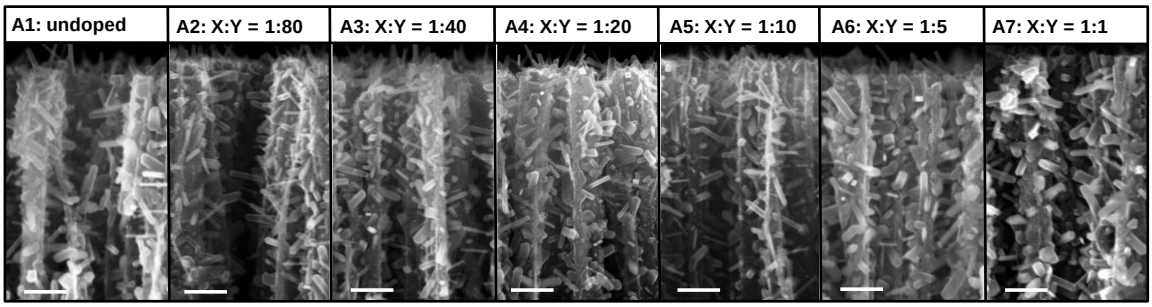

Figure 2.3. SEM images of TiO_2 NRs synthesized under different NH_3 cycle ratios. The ratio between NH_3 cycle and H_2O cycle in SPCVD growth is marked as *X:Y*. Scale bar, 200 nm.

Table 2.1. Summary of the average concentrations of N dopant corresponding to different doping ratios. The values were obtained by energy-dispersive X-ray spectroscopy (EDS).

	A1	A2	A3	A4	A5	A6	A7
Samples	Undoped	1 : 80	1 : 40	1 : 20	1 : 10	1 : 5	1:1
N at.%	0	0.82	1.52	1.81	2.01	2.28	1.79

length from 137 ± 7 nm (A4) to 114 ± 9 nm (A7) was observed. The NR diameter also rapidly increased from 19 ± 3 nm (A4) to 34 ± 5 nm (A7), evidencing a significant change of NR morphology from long and slim to short and plump upon the introducing of N dopants.

The statistical size measurement provides a preliminary understanding of the TiO_2 NR growth behavior by SPCVD under the influence of NH_3 precursor. The highest growth rate was achieved at ~3.6 Å/cycle when no NH_3 precursor was induced (A1). Reduced length growth rate was observed with the rising of Nitrogen doping ratio. The smallest length with the average length growth rate of 1.4 Å /cycle was identified when the most $TiCl_4/NH_3$ cycles were programed for Nitrogen doping (A7). This observation is similar to the ALD of Nitrogen doped TiO_2 films because TiN has lower growth rate than TiO_2.[43,103] In the high temperature SPCVD process, we have found that the unique anisotropic crystal growth behavior of TiO_2 is enabled by the formation and migration of metastable amorphous-crystalline mix-phased nanoparticles (NPs) *via* the principle of vapor-phase oriented attachment.[71] We therefore reckon that the deposition of TiN had significantly hindered the aggregation and migration of the metastable NPs and thus suppressed the NR length growth. The NR width growth rate, however, significantly increased from ~ 0.45 Å/cycle to 0.84 Å/cycle when the NH_3 precursor ratio was raised from1:20 to 1:1. This also indirectly evidences the immobilization of the metastable NPs, which stay at the side surfaces and induce faster width growth. Nevertheless, it appears that lower NH_3 ratio (< 1:20) can reduce the width growth rate as well. Therefore, the

aspect ratios of all samples followed a parabola-like curve as shown in Figure 2.1d. The maximum aspect ratio was 7.4 from Sample A4, which had a NH_3 precursor ratio of 1:20. In general, low doping concentration has minimal effect on the TiO_2 NR's growth rate and morphology, while high doping concentration could jeopardize the anisotropic crystal growth and forming more particle-like nanoscrystals.

The elemental characteristic of Nitrogen doped TiO_2 NRs was further studied by XPS as shown in Figure 2.4. The N 1s peaks could be identified from all Nitrogen doped TiO_2 NR samples (A2-A7) but were absent in the undoped one (A1) (Figure 2.4a). To analyze the chemical structures of Nitrogen doped and undoped TiO_2 NRs, three regions of the XPS spectrum were examined: N 1s scan near 400 eV, Ti 2p scan near 460 eV, and O 1s scan near 530 eV (Figure 2.4b). For TiO_2 NRs with different Nitrogen doping ratio, there are observable variations among each scan. Broad N 1s peaks expanding from 398.0 eV to 403.5 eV were observed in all Nitrogen doped samples. The peaks were located at binding energies higher than the typical value of TiN (397.2 eV).[105] This is considered as the consequence of higher N 1s binding energy in an O-Ti-N environment, where the formal charge of N in O-Ti-N is more positive than that in TiN.[106,105] The variation in peak intensities and positions also reveals the different concentrations and chemical environment. The doublet lines in the spectrum profiles in the Ti 2p and O 1s scanning regions of doped and undoped TiO_2 NRs exhibit similar differences. In particular, sample A6's ($X:Y$ = 1:5) exhibit the most significant shift of its Ti $2p_{3/2}$ peak to lower binding energy (459 eV) and amplitude attenuation of its O 1s peak at 533 eV (red

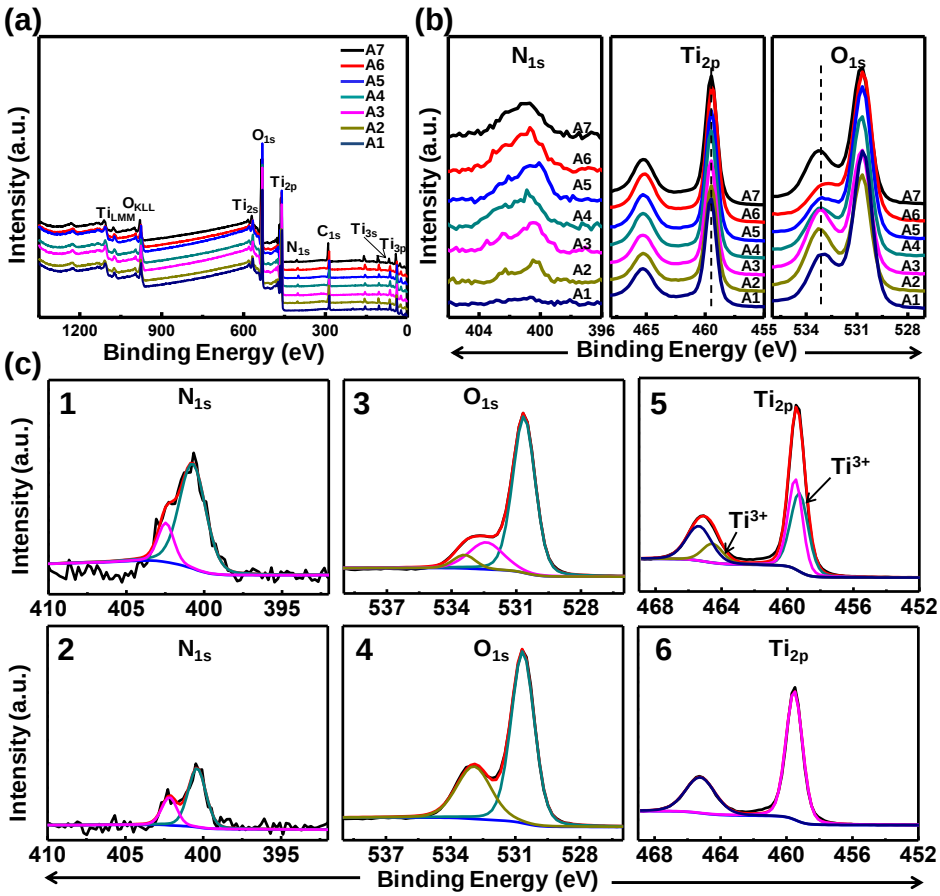

Figure 2.4. XPS characterization of Nitrogen doped TiO_2 NRs with different Nitrogen doping ratios (A1-A7) (a) Full XPS spectra. (b) N 1s scan near 400 eV, Ti 2p scan near 460 eV, and O 1s scan near 530 eV of A1-A7 samples. (c) The deconvoluted spectra for N 1s peak of heavily-doped sample A6 (1) and lightly-doped sample A2 (2); O 1s peak of heavily-doped Sample A6 (3) and undoped Sample A1 (4); and Ti 2p peak of heavily-doped Sample A6 (5) and undoped Sample A1 (6).

curve in Figure 2.4b). The shift in the binding energy of Ti 2p peaks toward lower values indicates a successful incorporation of N in TiO_2 lattice. The change in O 1s spectrum suggested the formation of O-Ti-N bonds and the modification of OH groups on the NR surfaces.[106,72,105]

In order to elucidate the chemical binding states of N, O and Ti elements, the deconvoluted spectra for N 1s, O 1s and Ti 2p peaks were investigated and presented in Figure 2.4c. The N 1s profile can be split into two characteristic peaks and assigned to O-Ti-N or Ti-N-O bonds at 400.2 eV (green peak) and NH_4^+ adsorbed on NR surfaces at 402.5 eV (purple peak) as reported in literatures (Figures. 2.4c-1 and 2.4c-2).[107,108] As shown in Figure 2.4c-1, the area ratio of the O-Ti-N peak (at ~ 400.2 eV) to the total N1s peak in sample A6 (*X:Y*=1:5) is ~0.86 while the area ratio of NH_4^+ (at ~ 402.5 eV) is ~0.14. When the doping ratio decreased to *X:Y*=1:80 (Sample A2 shown in Figure 2.4c-2), the two ratios became 0.61 and 0.39, respectively, suggesting that a more substitutional doping might happen at 1:5 doping ratio. By comparing the Nitrogen doped Sample A6 and undoped Sample A1, more notable variations were observed in O 1s (Figures 2.4c-3 and 2.4c-4) and Ti 2p (Figures 2.4c-5 and 2.4c-6) signals regarding to N incorporation. The O 1s peak of A6 was deconvoluted into three contributions at 530.6 eV (green), 532.4 eV (purple) and 533.4 eV (yellow) which are identified as Ti-O, O-Ti-N and surface OH groups, respectively. The peaks of sample A1 were only deconvoluted into two components of Ti-O (green) and OH groups (yellow), while the O-Ti-N signal at 532.4 eV was absent. This further confirms that the O-Ti-N bonds were formed in the

Nitrogen doped TiO_2 NRs. The surface OH group-related peak at 533.4 eV is common in XPS studies of TiO_2. The area ratio of this component was reduced in sample A6, possibly due to more substitutions of O atoms by N, and the consumption of surface OH groups for NH_3 protonation (Figure 2.4c-1).[108]

Earlier research mentioned that the valence state of the Ti cations in TiO_2 should be reduced when N substitutes O by doping. The binding energy of Ti 2ppeaks shifted to lower values due to Ti^{4+} being reduced to Ti^{3+}.[106,109] Development of the O-Ti-N bonds through partially substituting O with N in TiO_2 lattice can be evidenced by the shifts of Ti 2p binding energy.[106] This effect was illustrated by XPS profiles of Ti 2p scans.[107,110] Figure 2.4c-5 is the deconvoluted spectra of the Ti 2p peaks of sample A6. The extra Ti^{3+} signals appeared at 459.3 eV in Ti $2p_{3/2}$ (green) and 464.5 eV in Ti $2p_{1/2}$ (yellow), which were located at the lower binding energy side of each Ti-O peak. The undoped one only showed two peaks of typical Ti-O bonds (Figure 2.4c-6).

TEM was implemented to study the morphology and crystal structure of the Nitrogen doped TiO_2 NRs. Figure 2.5a shows HRTEM images of NRs from sample A6 that exhibits the highest detected N concentration. The images were taken from the tip and body regions. The truncated tip of this NR is typical and the facets could be indexed as the (001), (011), $(0\,\bar{1}\,\bar{1})$, and $(0\,\bar{1}\,1)$ planes. The tip angle of NR is 111.4°, representing the angle between the $(0\,\bar{1}\,1)$ and (001) planes with lattice spaces measured to be 0.35 nm and 0.48 nm, respectively (Figure 2.5b). The NR tip and body was completely covered by a ~2.5-3.5 nm thick percolated layer, a mixture of randomly-oriented nanocrystals with

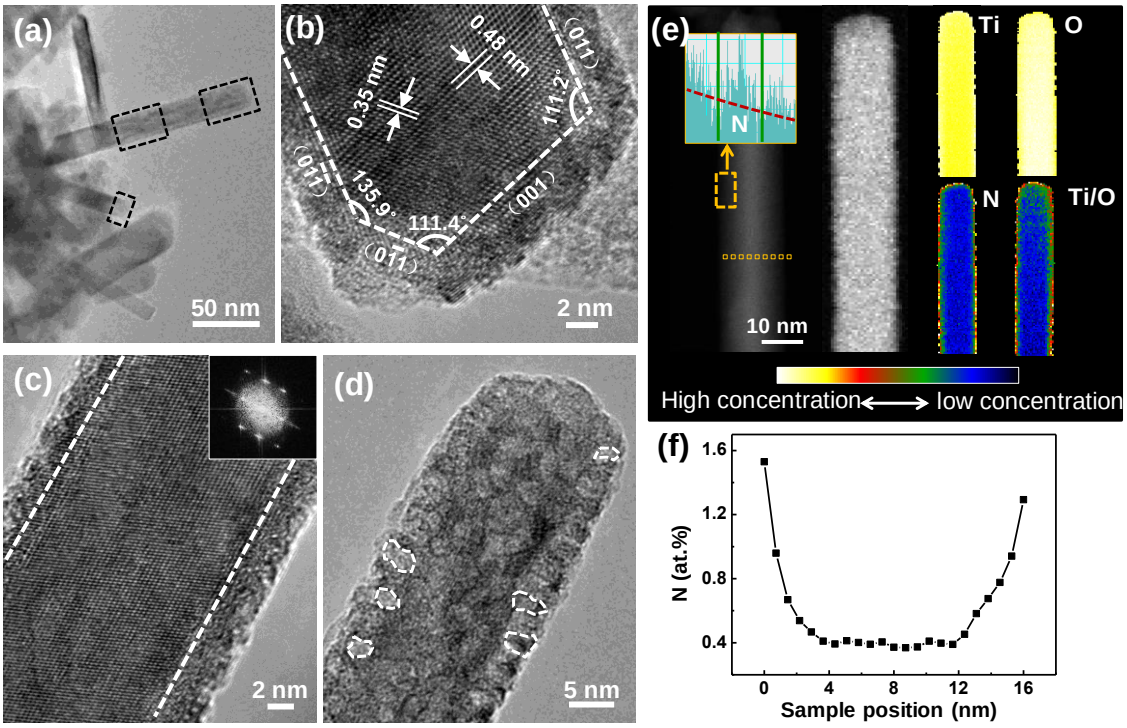

Figure 2.5. Structure and species distribution in TiO_2 NRs. (a)TEM image of Nitrogen doped TiO_2 NRs bundles on a Si NW. (b, c) High resolution TEM images taken from the tip (b) and body (c) regions. The NR is covered by a~2.5-3.5 nm thick percolated layer as marked by the dashed lines. Inset in (c) is the FFT pattern of the lattice image. It confirms the anatase phase.(d)Voids observed in the percolated layer, as marked by white dashed lines. (e) EELS spectrum image measurements on a Nitrogen doped TiO_2 NR showing the distributions of Ti, O and N elements, as well as the concentration difference between Ti and O (Ti/O) along the entire NR body. (f) N concentration profile along the NR crosssection as marked by the square dots in the left panel of Figure 2.5e.

amorphous intercalations (Figure 2.5c). This is different from the single crystalline sharp surfaces that were observed from the undoped TiO_2 NRs.[111] Beneath the percolated layer, the NR exhibit a nearly perfect crystal lattice with perfect {011} facets, which is consist with the observation for undoped TiO_2 NRs.[111] Analysis of the Fast Fourier Transform (FFT) pattern of cut image showing the central part of N-doped NR reveals the anatase structure of TiO_2 (inset of Figure 2.5c).

To analyze the element distribution and understand the composition of the percolated layer, electron energy loss spectroscopy spectrum image (EELS SI) was taken from a single Nitrogen doped TiO_2 NR (center and left panel of Figure 2.5e). Appreciable N signal in EELS spectrum was detected from the NR (left panel of Figure 2.5e). Elemental mapping clearly reveals the distributions of Ti, O and N elements, as well as the concentration difference between Ti and O (Ti/O) along the entire NR body (right panel of Figure 2.5e). More Ti was found near the NR surface, where less O element was identified. The map of Ti-O reveals the O depleted surface region and the stoichiometric NR body. The N map demonstrates a concentrated N region along the NR surface profile. Such a non-uniform N distribution is further confirmed by measurement of the N concentration profile along the NR cross-section as shown in Figure 2.5f, where depth of surface layer with increased concentration of nitrogen was ~4 nm.

It is known that the impurity formation energy in doped nanocrystals increases as the crystal size decreases.[112] Impurities atoms can diffuse to the crystal surface, referred as self-purification.[112,113] Meanwhile, point defects such as vacancies and interstitials can

diffuse outward and aggregate to form voids and grain boundaries.[35,114] We believe the formation of the percolated layer with highly concentrated N atoms manifests above processes. In the high-temperature SPCVD process, oxygen vacancies associated with O-Ti-N structures could diffuse to the surface while the TiO_2 NR body was crystallized, forming voids (Figure 2.5d) in the percolated layer.[115] As a result, the Nitrogen-rich percolated layers were formed near the NR surfaces. Because the NR formation mechanism has been found to be the migration of crystallized particles on manifold body followed by orientated attachment on high surface energy facets (the tip part of NRs), significant amount of the percolated layer covering the NRs might be an obstacle for the migration and attachment of crystal particles to the tip area of NRs.

Theoretical and experimental work suggested that N impurity could introduce localized states above valence band maximum (VBM) or VBM lifting, enabling photoactiviy in the visible light range.[72,75,81,116] Therefore, introducing Nitrogen doping to the SPCVD TiO_2 NR branch growth is expected to realize a promising 3D NR architecture for high-performance PEC photoanode across a wide spectrum range. To investigate the doping-related PEC performance, the six Nitrogen doped TiO_2 NR samples (A2-A7) and the undoped sample (A1) were used as PEC photoanodes and their photocurrent density (J_{ph}) characteristics versus bias potential were measured under the same conditions. Corresponding PEC efficiencies were estimated using following equation:[76]

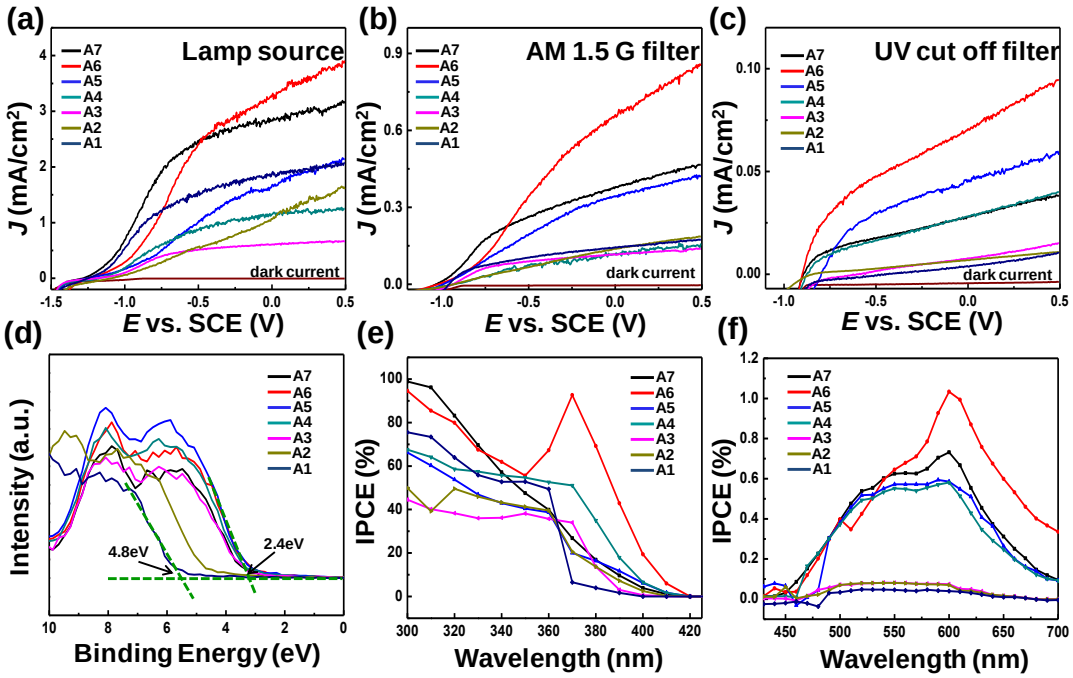

Figure 2.6. (a-c) *J-V* curves of Nitrogen doped and undoped TiO_2 NRs-Si NW hierarchical architectures under illuminations of 100 mW cm^{-2} Xe lamp source, lamp with AM 1.5G filter, and with UV cutoff filter, respectively. (d) XPS demonstrates that density of states (DOS) shift in the valence band happened to all Nitrogen doped samples. The maximum shift is ~ 2.4 eV in sample A6. (e)(f) IPCE of Nitrogen doped and undoped TiO_2 NRs-Si NW hierarchical architectures within the wavelength range of 300-425 nm and 425-700 nm, respectively.

$$\eta\% = \left[J_{ph}(E^0_{rev} - |E_{bias} - E_{aoc}|)\frac{100}{I_0}\right] \qquad (2.1)$$

where E_{bias} is the bias potential; E^0_{rev} = 1.23V is the standard state reversible potential for water-splitting reactions; and E_{aoc} = V_{oc} is the open circuit voltage (vs. SCE). Figure 2.6 (a-c) show representative J_{ph} –V curves collected under the illumination of a 100 W cm^{-2} Xe lamp without and with AM 1.5G or UV cutoff filters. The dark current densities of each PEC test remained at fairly low values (<10^{-4} mA cm^{-2}) within the bias potential range between -1.1 V and 0.5 V (vs. SCE), indicating high quality crystal surfaces of the as-synthesized TiO_2 NR architectures. Among all the samples, A6 exhibited the highest J_{ph} under all wavelength conditions. Generally, higher Nitrogen doping yielded high photocurrent and higher efficiency. All the photocurrent and efficiency data are summarized in Table 2.2. Under direct Xe lamp illumination, the maximum efficiency was calculated to be 1.35% at ~ -0.75 V from sample A7 (Figure 2.7a). This value is close to that of sample A6 (1.23%) and 48% higher than that of the undoped TiO_2 NR photoanodes (0.91% at ~ -0.77V). However, other Nitrogen doped TiO_2 NR samples (A2-A5) all yielded lower photocurrent and efficiency compared to the undoped one. This is possibly due to the defective crystal structure around the NR surfaces (Figure 2.5), which would jeopardize the charge transport even though their visible light photoactivity might be higher than that of the undoped sample.

When an AM 1.5G filter was applied, sample A6 yielded the maximum efficiency of 0.26% at ~ -0.36 V; whereas, the efficiency of A7 rapidly dropped to 0.19%, which was only 73% of that of A6. Other than A5, whose J_{ph} was about the same level as A7, all the

Table 2.2. Summary of Photocurrent Density and PEC Efficiency of Nitrogen doped and undoped TiO_2 NR-Si NW architectures measured under different illumination conditions.

	Samples	A1 Undoped	A2 1:80	A3 1:40	A4 1:20	A5 1:10	A6 1:5	A7 1:1
J (mA cm^{-2})	Lamp Source	2.081	1.650	0.668	1.271	2.159	3.920	3.187
	UV cut off filter	0.011	0.011	0.015	0.040	0.060	0.095	0.039
	AM 1.5 G filter	0.175	0.187	0.140	0.159	0.426	0.858	0.466
η (%)	Lamp Source	0.905	0.362	0.324	0.531	0.492	1.232	1.357
	UV cut off filter	0.004	0.003	0.005	0.014	0.028	0.040	0.015
	AM 1.5 G filter	0.082	0.059	0.074	0.060	0.149	0.257	0.188

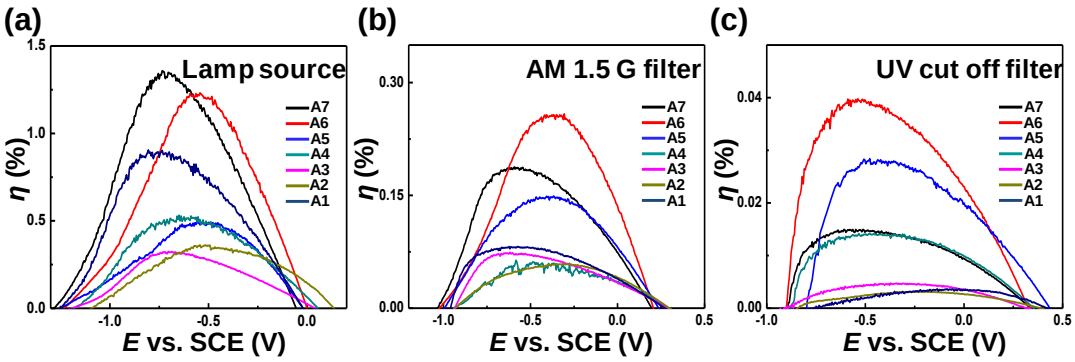

Figure 2.7. (a-c) Corresponding PEC efficiencies of Nitrogen doped and undoped TiO_2 NRs-Si NW hierarchical architectures under illuminations of 100 mW cm^{-2} Xe lamp source, lamp with AM 1.5G filter, and with UV cutoff filter, respectively.

other Nitrogen doped NRs exhibited the same level of performance as the undoped one (~0.08%). Therefore, under AM 1.5G illumination, the maximum efficiency offered by Nitrogen doping was 225% higher than that of the undoped TiO_2 NRs.

When the samples were only exposed to visible light by applying a UV cut-off filter (cut-off wavelength of 400 nm), the photocurrents were further reduced. As shown in Figure 2.6c, 2.7c and Table 2.2, sample A6 still exhibited the highest performance with a maximum efficiency of 0.04% at ~ -0.54 V. Under this situation, the J_{ph} and efficiency of sample A7 further dropped to the same level of sample A4 ($X:Y$ = 1:20) and was outperformed by sample A5. Similar to the observations under UV-involved illuminations, no significant difference was found between the low-doping-concentration samples (A2 and A3) and the undoped one, where the photocurrents were remained at 0.01 mA cm^{-2} level. Due to the rapid photocurrent drop when the entire UV spectrum was cut off, one order of magnitude enhancement was identified when appropriate N was doped into TiO_2 NRs.

The as-synthesized heavily Nitrogen doped TiO_2 NRs (A6) appeared darker in color compared to the undoped TiO_2 NRs (A1, inset Figure 2.8), demonstrating its more effective absorption of visible light. Corresponding UV-Vis absorption spectra revealed a significantly enhanced absorption in the visible light regime (<~600 nm) as a result of Nitrogen doping (Figure 2.8). XPS was then used to further understand this phenomenon from the aspect of density of states (DOS) shift in the valence band (Figure 2.6d). From the XPS spectra, the undoped TiO_2 NRs (A1) exhibited a VBM at ~4.8 eV. While sample

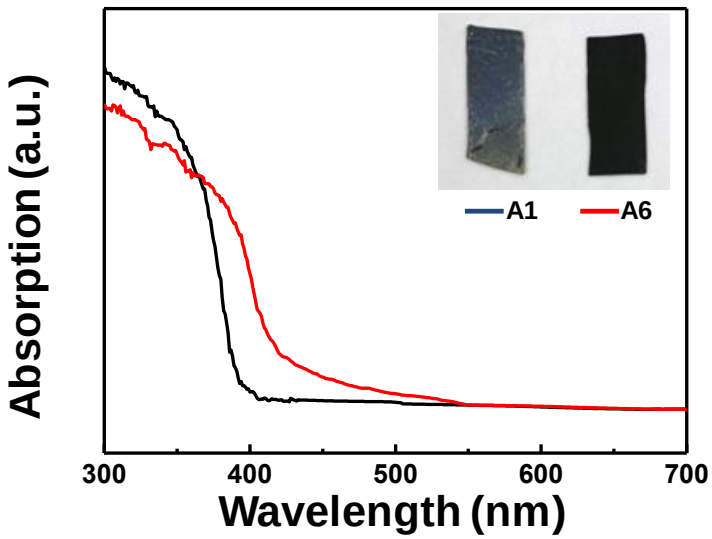

Figure 2.8. UV-Vis absorption spectra of heavily-doped (A6) and undoped (A1) TiO_2 NRs. Significant red shift of the absorption spectrum from A6 was observed. Inset is a digital photo shows the much darker color of heavily-doped TiO_2 NRs (A6) compared to the undoped TiO_2 NRs (A1), suggestingits more effective absorption of visible light.

A2, which had the lowest N doping concentration, only exhibited a shift of 0.5 eV, all the other Nitrogen doped samples showed a shift of 2.2-2.4eV. The change of VBM evidences the emergence of absorption capability in the visible light range, which could possibly enable photoactivity in broad-band illumination and thus enhanced PEC performance. These observations evidence the successful activation of visible-light photoactivity induced by N doping.

Incident-photon-to-current-conversion efficiency (IPCE) was used to quantitatively understand the N doping effect on the photoactivity as a function of incident wavelength.[117,118] IPCE characterizations (Figures 2.6e and 2.6f) were conducted on all Nitrogen doped and undoped samples at the potentials where J_{ph} approaches saturation (e.g. -0.55V vs. SCE for A6). IPCE values were calculated *via* the following equation:[119]

$$IPCE(\%) = (1240J_{ph})/(\lambda P_{mono}) \qquad (2.2)$$

where J_{ph} is the photocurrent density at the incident wavelength λ. P_{mono} is the power density of the incident monochromatic light. All the samples exhibited significant photoactivity over the entire UV region and decreased sharply when the wavelength is greater than 360 nm. The lowest IPCE (~35-40%) was found from sample A2 and A3, which was consistent with the lowest J_{ph} and efficiency observed from these two samples in all wavelength ranges. We believe this is due to the very low level of Nitrogen doping that was not sufficient to completely alter their optoelectronic behavior but rather introduced defects jeopardizing the charge transport properties. It is also surprise to see a very high IPCE from relatively heavily doped TiO_2 NR samples (A6 and A7). Their IPCE

reached over 95% in the UV range, which was 27% higher than that of undoped TiO_2 NRs. Considering the absorption of heavily-doped TiO_2 in this wavelength range is comparable to that of undoped one, we attribute this enhancement to their more efficient utilization of UV light where the separation and transportation of photoexcited charge carriers are more effective.[79,117] Sample A6 exhibited the highest high IPCE (~94%) at ~360 nm and the longest cutoff wavelength at 425 nm, which is consistent with its highest photoactivity among all samples. A blue shift on the cutoff wavelength was observed when the dopant concentration decreased and the undoped TiO_2 NRs exhibited the shortest cutoff wavelength at ~400 nm, which is consistent with their UV-Vis spectra.

Figure 2.6f shows IPCE in the visible light region. Here, we can allocate their visible light performance into three groups. Group I: relatively heavily doped TiO_2 NRs (A6 and A7). They exhibited the highest IPCE in the 450 to 700 nm range (0.8%-1.0%) with an obvious peak at ~610 nm. Group II: moderately doped TiO_2 NRs (A4 and A5). They showed a broad IPCE peak in the 450 to 700 nm regime with a maximum value of ~0.6% across a broad band (500-600 nm). Group III: lightly- and un-doped TiO_2 NRs (A1-A3). Their IPCE were nearly zero within this wavelength range suggesting that the low concentration of N is not able to introduce photoactivity in the visible light range. Considering Ti^{3+} in Nitrogen doped TiO_2 is referred as a color center which induces interbands for visible light absorption,[107,120,121] we attribute the conspicuous IPCE around ~610 nm of Group I Nitrogen doped TiO_2 to the Ti^{3+} related interbands light absorption.

In addition, the IPCE investigation also helps in understanding the strong wavelength

dependence of Sample A7's PEC performance. Since both A6 and A7 exhibited comparably high IPCE in the UV range (<350 nm), they showed similar PEC performance under Xe lamp illumination which had a significant UV portion. IPCE of A7 rapidly dropped when wavelength was greater than 350 nm. Therefore, its PEC performance lowered to the level of Sample A5 when AM 1.5G filter was applied. Once the UV illumination was completely blocked by a UV cut off filter, the J_{ph} and efficiency of A7 further dropped to the same level of A4, despite its higher IPCE in the visible light region.

2.4. Conclusion

In this chapter, we successfully introduced Nitrogen doping capability in the SPCVD process for synthesizing high-density Nitrogen doped TiO_2 NR branches on dense Si NW forests. The N elements were introduced by adding NH_3 vapor as additional precursor pulses between typical H_2O and $TiCl_4$ cycles for growing TiO_2 NRs at 600 ℃. The dopant concentration can be rationally controlled by adjusting the ratio between the doping cycles and regular TiO_2 growth cycles. HRTEM and EELS mapping revealed that the N dopants were mostly accumulated around the surface of NR forming a percolated layer. XPS study confirmed the formation of O-Ti-N bonds in Nitrogen doped TiO_2 NRs. Ti^{3+} signals were also observed, which are associated with the reduction of Ti^{4+} when N substitutes O by doping. Compared to undoped one, the valence band maximum of Nitrogen doped TiO_2 NRs exhibited a notable lifting up. The largest shift value reached ~2.4 eV in the most highly doped sample. The as-synthesized Nitrogen doped TiO_2 NR

branched heterostructures were used as PEC photoanodes and their performances were characterized within controlled illumination wavelength ranges. The Nitrogen doped TiO_2 NRs demonstrated fairly competitive photoactivity under 100 W cm^{-2} Xe lamp and simulated solar illuminations. Appreciable PEC activity was also observed in the visible light range from 450 to 700 nm. The maximum efficiencies offered by Nitrogen doping were 225% higher than those of the undoped TiO_2 NRs under AM 1.5G illumination. The enhancement of PEC efficiency was more than 900% when only visible light was illuminated. Successful synthesis of Nitrogen doped TiO_2 NRs by the SPCVD method introduces a strong new capability to this novel and powerful 3D NR growth technique. It enables composition and optoelectronic property control of the NR branches, allowing performance enhancement or creating new functionality. Understanding the doping behavior and controlling the doping concentration in SPCVD 3D NR growth hold a great promise for engineering the electrical properties of functional nanomaterials for PEC and other energy harvesting and conversion applications.

Chapter 3. Cellulose Nanofiber-Templated 3D TiO_2 Nanorod Architecture for PEC Photoanode

3.1. Introduction

PEC water splitting has received considerable attention on the development of solar fuel technologies to relieve our dependence on fossil fuels and to reduce greenhouse gas emissions.[76,122-124] High-performance photoelectrodes of PEC systems demand broad-band and high-percentage light absorption; instantaneous and low-loss charge separation, collection and transportation; and large and clean electrode-electrolyte interfaces.[33-35,76,125-128] High porosity 3D nanostructures, such as branched nanowire architectures and nanofiber networks, are considered as excellent candidates for PEC photoelectrode development. As a result, 3D nanostructures are the current focus of a tremendous surge of interest in PEC photoanode development.[34,129]

Among all nanostructured 3D morphologies, natural cellulose-based nanomaterials such as CNFs are another type of widely used large-scale renewable 3D mesoporous structures owing to their great abundance, low cost, bio-compatibility and degradability.[130-132] They are composed of elementary cellulose fibrils and show comparable mechanical properties (e.g. Young's modulus and tensile strength) as other fibrous materials (e.g., carbon fibers and glass fibers).[133] CNFs also exhibit significant absorbability to both hydrophilic and hydrophobic materials.[134] They are therefore a remarkable template for processing functional 3D nanostructures with extremely large

porosity, and possess a great promise for the development of high-performance energy harvesting and storage devices. For example, nanostructured networks of cellulose-graphite platelet composites were applied as Li-ion battery anodes demonstrating excellent flexibility and good cycling performance;[135,136] porous cellulose-templated TiO_2 nanostructures were used in photocatalytic and dye-sensitized solar cells (DSSCs) exhibiting significantly enlarged surface area and improved electron transport properties;[137,138] and cellulose/polyaniline nanocomposites were developed for supercapacitors with enhanced mass-specific capacitance.[139] Combining the CNF-templated nanostructures with branched functional NR configurations would lead to a novel hierarchical nanostructure with enhanced PEC performance and photoelectrode manufacturability.

In this chapter, further application of SPCVD TiO_2 NR growth will be discussed by using nature CNFs as template. 3D high-density hollow fibrous networks with branched TiO_2 NRs were synthesized on CNF-ZnO core-shell structures by SPCVD. The ZnO layer was completely converted into TiO_2 during the growth following the Kirkendall effect.[73] Compared to other CNF-templated mesoporous nanostructures (i.e. TiO_2-ZnO bilayer tubular nanofibers network and TiO_2 nanotubes network), 3D TiO_2 fiber-NR heterostructure exhibited significantly enhanced photocurrent and PEC efficiency owing to their large surface area and good electrical conductivity.

3.2. Experimental Section

Fabrication of CNFs Template: The CNFs used in our experiments were

tetramethylpiperidine-1-oxy (TEMPO) oxidized wood pulp fibers, which were prepared according to the method reported by Saito et al.[140,141] In particular, the CNFs hydrogel solution (0.4 wt%) was obtained by mechanically homogenizing the TEMPO-treated wood pulp fibers on an M-110EH-30 Microfluidizer (Microfluidics, Newton, MA, USA) with a series of 200- and 87-μm chambers *via* two pass-throughs. After printing the CNFs hydrogel on Fluorine doped Tin Oxide (FTO) glass substrate, the substrate with hydrogel film was frozen in a liquid N_2 and ethanol bath. The substrate was then placed into the vacuum chamber of Labconco 4.5 Freeze Dryer (Labconco, Kansas City, MO, USA) immediately, keeping 12 hours at room temperature with a base pressure of ~35 mTorr, where sublimation of the ice yielded a nanofibrous structure cellulose film, 10 μm thick on the FTO.

Fabrication of 3D TiO_2 fiber-NR heterostructure: The as-prepared CNF nanostructure on FTO substrates were loaded into ALD chamber for ZnO overcoating at 150 ℃. In one growth cycle, H_2O and diethylzinc (DEZn) vapor precursors were pulsed into the chamber for 1 s each and separated by N_2 purging for 60 s. The 150-cycle ALD growth yielded a 30 nm-thick ZnO film covering CNFs. This CNF-ZnO core-shell structure on FTO substrates was then used for SPCVD TiO_2 NR branch growth. Similar to the ALD process, 400 cycles alternating reactions were proceed at 600 ℃. Each cycle consisted of 1 s H_2O pulsing + 60 s N_2 purging + 1 s titanium tetrachloride ($TiCl_4$) pulsing + 60 s N_2 purging. Through this process, TiO_2 NRs were uniformly grown on the fibrous backbones.

In order to compare the PEC performance, both CNF-templated TiO_2-ZnO bilayer tubular nanofibers and fibrous TiO_2 nanotubes networks were prepared. For the TiO_2-ZnO samples, 400 cycles of ALD TiO_2 films were coated on CNF-ZnO core shell nanofibers. The deposition was performed at 300 ℃ with 1 s H_2O pulsing + 60 s N_2 purging + 1 s titanium tetrachloride ($TiCl_4$) pulsing + 60 s N_2 purging for each cycle. The fibrous TiO_2 nanotubes network was synthesized *via* 400-cycle ALD TiO_2 coating at 150 ℃ on CNFs template and sintered at 600 ℃ to crystallize the TiO_2 coating and remove CNF templates.[76] The fabrication process is schematically illustrated in Figure 3.1.

PEC Characterization: PEC characterizations were performed in 1 mol L^{-1} KOH (pH=14) aqueous solution using a three-electrode electrochemical cell configuration. The saturated calomel electrode (SCE) was used as the reference electrode and a Pt wire was used as the counter electrode. All electrodes were connected to a potentiostat system (Metrohm Inc., Riverview, FL) for *J*–*V* measurement. Light illumination was provided by a 150 W Xe arc lamp (Newport Corporation, Irvine, CA) and the intensity at the PEC anode position was adjusted to be 100 mW cm^{-2}. An AM 1.5G filter and a UV cut off filter were also utilized with the lamp for PEC characterizations.

3.3. Results and discussion

The as-fabricated CNF networks on FTO substrates are shown by SEM in figure 3.2a. The higher-magnification inset reveals a 3D fibrous structure of CNFs with an average fiber diameter of ~0.1 μm. This high-porous nanostructure was well-preserved after 150 ℃ ALD of ZnO thin film conformal coating (figure 3.2b). The surface of ZnO-coated

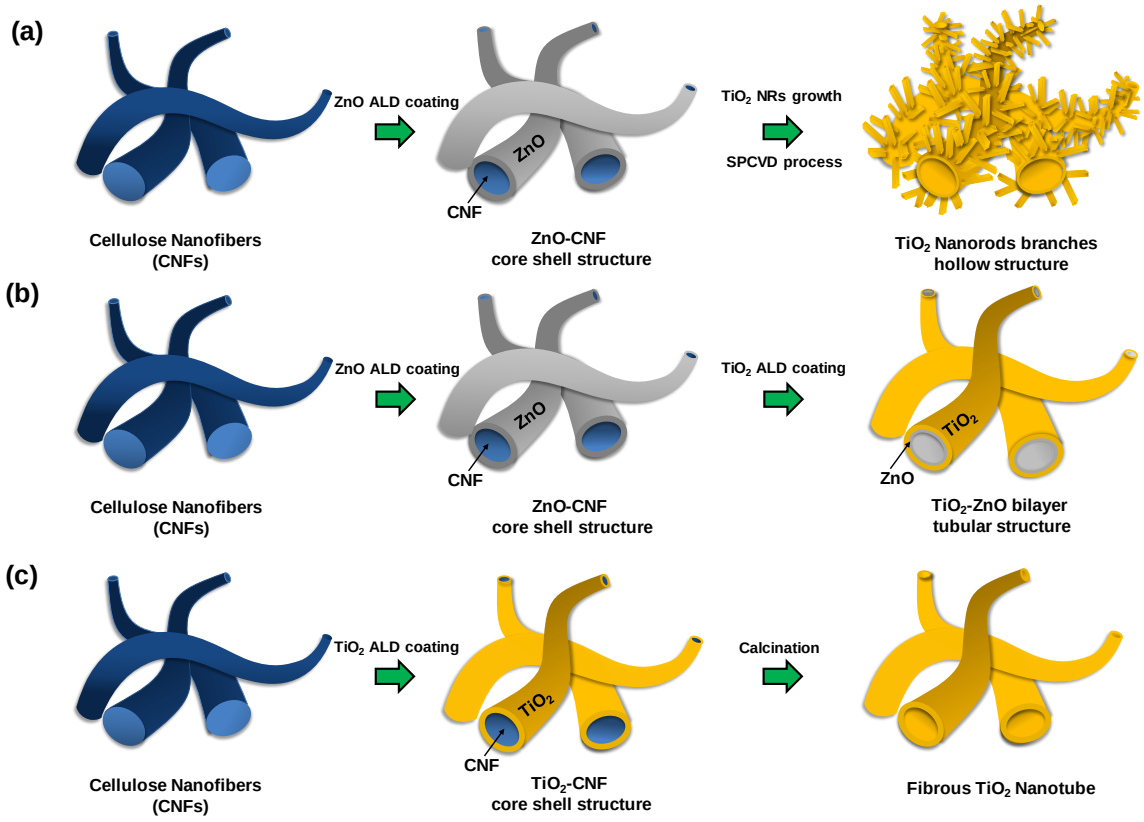

Figure 3.1. Schematic synthesis procedures of CNF-templated nanostructures. (a) 3D TiO_2 fiber-NR heterostructure by ALD and SPCVD process. (b) TiO_2-ZnO bilayer tubular nanofibers by ALD ZnO and TiO_2 coating. (c) Fibrous TiO_2 nanotubes networks by ALD TiO_2 coating and calcination in vacuum.

CNF was relatively rough, which is a result of the polycrystalline nature of the ZnO coating (Inset of figure 3.2b). Figures 3.2c and d show the morphologies of TiO_2-ZnO bilayer tubular nanofibers and TiO_2 nanotube fibrous networks, respectively, as two reference samples. Both structures present a well-preserved nanofibrous structure. 300 ℃ TiO_2 ALD coating yielded a polycrystalline TiO_2 shell over the CNF-ZnO core-shell fibers and burned away the CNF templates (inset of figure 3.2c).[76,142] The fiber diameter was slightly increased (~190 nm). The rough surface of final fibrous structure was replicated from the polycrystalline ZnO and became more notable. The TiO_2 nanotubes shown in Figure 3.2d and inset demonstrated a smooth surface with a mean diameter similar to those of fibrous CNF-ZnO core shell network. It is noteworthy in Figure 3.2 that the fibrous 3D network configuration was very stable during both low-temperature ALD and high-temperature heat treatment processes, and no morphology change could be observed.

Branched TiO_2 NRs SPCVD growth was conducted on the ZnO-coated CNF templates shown in Figure 3.2b. The 3D fibrous network morphology was also well-preserved after 14 hours of 600 ℃ SPCVD process (figure 3.3a). From higher magnification SEM images, the uniform and dense coverage of TiO_2 NRs can be clearly observed along the entire fiber length (figure 3.3b). The fibers trunks were ~220 nm in diameter, which was ~22% more than that of ZnO-CNF template. All TiO_2 NRs were rooted on the walls of nanofibers and pointed out divergently. The NRs exhibited an average length of ~170 nm and a diameter of ~30 nm (aspect ratio is ~5.7) (figure 3.3c).

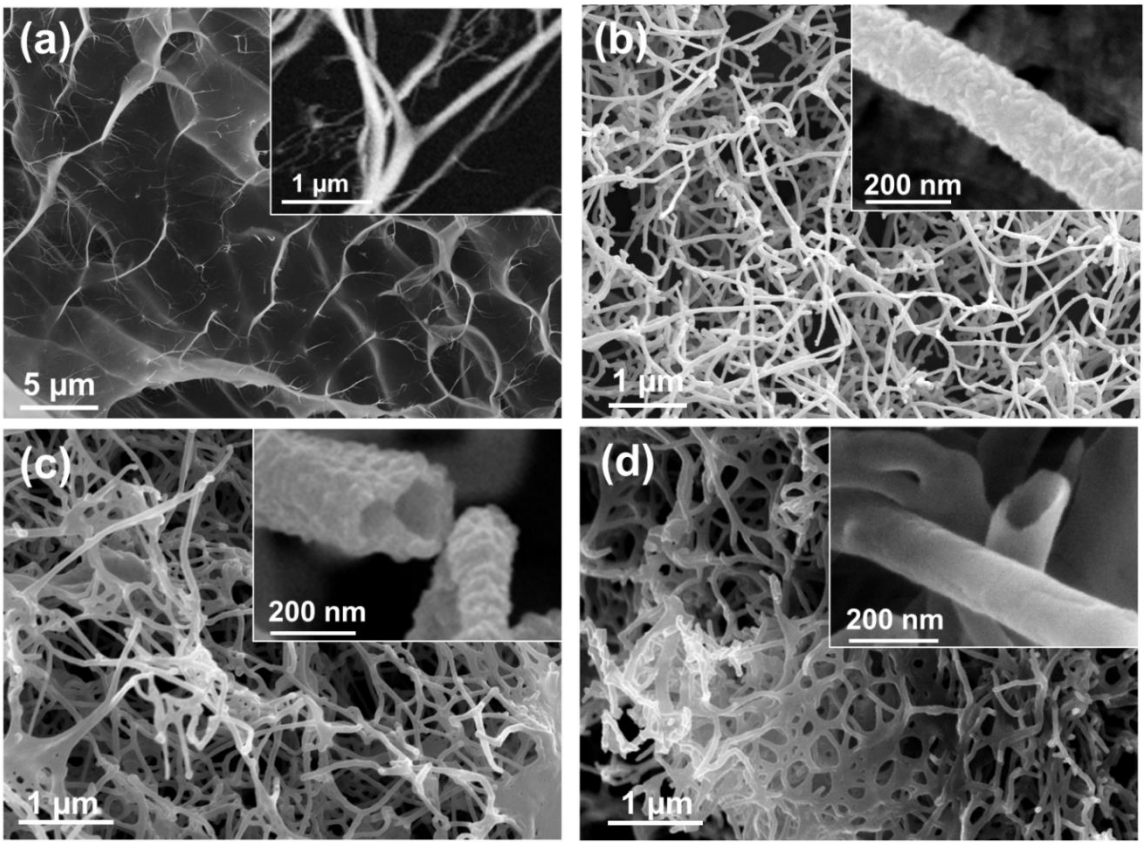

Figure 3.2. Morphologies and structures of CNF films and templated 3D architectures. (a) CNF film processed on a FTO substrate; inset is a high magnification image for cellulose nanofibers. (b) CNFs coated with 150-cycle ALD ZnO at 150 ℃; inset shows the crystalline ZnO film with rough surface. (c) Crystalline TiO_2 film overcoating on CNF-ZnO core shell template by 300-cycle ALD at 300 ℃; inset show the CNFs extinction and nanotubular structure. (d) Fibrous TiO_2 nanotube network after 400-cycle TiO_2 ALD at 150 ℃ and 24 hours annealing at 600 ℃ in vacuum; inset reveals the hollow structure and related smooth surface.

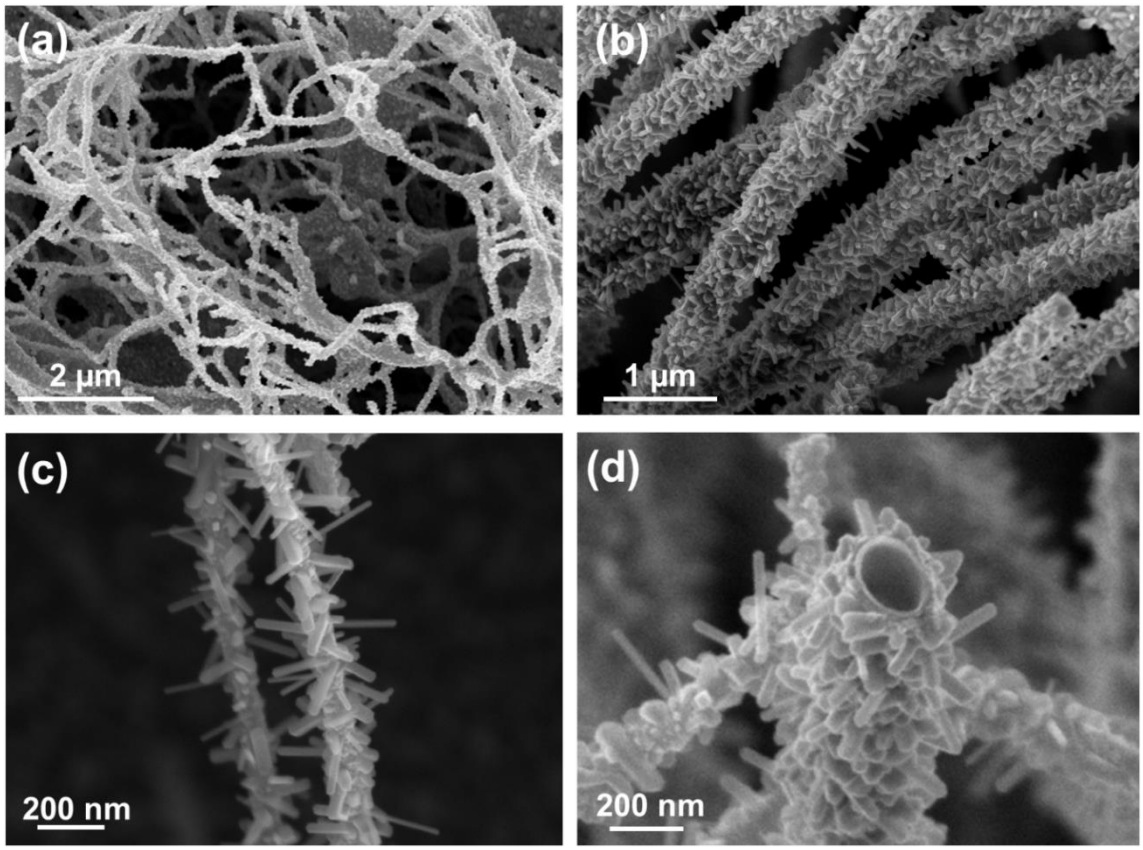

Figure 3.3. Morphology and structure of CNF-templated TiO_2 branches architecture. (a) Fibrous morphology was preserved after branched TiO_2 network growth. (b) High-density TiO_2 NRs that grew laterally out of the fiber surfaces via 400-cycle SPCVD process. (c) (d) Higher magnification SEM images indicate entirely covered fiber surfaces with TiO_2 NRs and the hollow backbone structure after growth.

Cross-sectional image of a single fiber (figure 3.3d) shows the hollow center of the branched structure and evidences the removal of fiber templates during high-temperature deposition. The diameter of the orifice was close to 180 nm which was larger than the size of cellulose fiber but comparable to that of the CNF-ZnO core-shell template. The continuous wall thickness was only ~10 nm.

The crystal structures of these three CNF-templated TiO_2 fibrous networks were further investigated by TEM (figure 3.4). All the tubular nanofibers exhibited a uniform wall thickness along the entire channel, which is consistent with the SEM results. TiO_2 NR-branched nanofibers were shown in Figure 3.4a, where a uniform ~10 nm wall can be clearly observed and the inner diameter was as large as that of the CNF-ZnO core shell template. The NRs exhibited a uniform contrast indicating their single crystal structure. These observations are consistent with our recent discovery of the Kirkendall effect during high-temperature TiO_2 ALD. When ZnO NW arrays were used as the initial template, 400-cycle SPCVD of TiO_2 at 600 ℃ yielded high-density branched TiO_2 NRs on TiO_2 nanotubes that were converted from the ZnO NWs *via* cation diffusion and exchange.[73] We believe such an effect also applied to our CNF-ZnO core-shell templates, where the ZnO shell was fully converted into the thin TiO_2 walls during the initial growth stage.

The TiO_2-ZnO bilayer tubular nanofibers were fabricated via 150 cycles of ZnO and 400 cycles of TiO_2 ALD at 150 ℃ and at 300 ℃, respectively. The wall thickness of this hierarchical tubular structure was found to be ~50-60 nm (figure 3.4b), which is

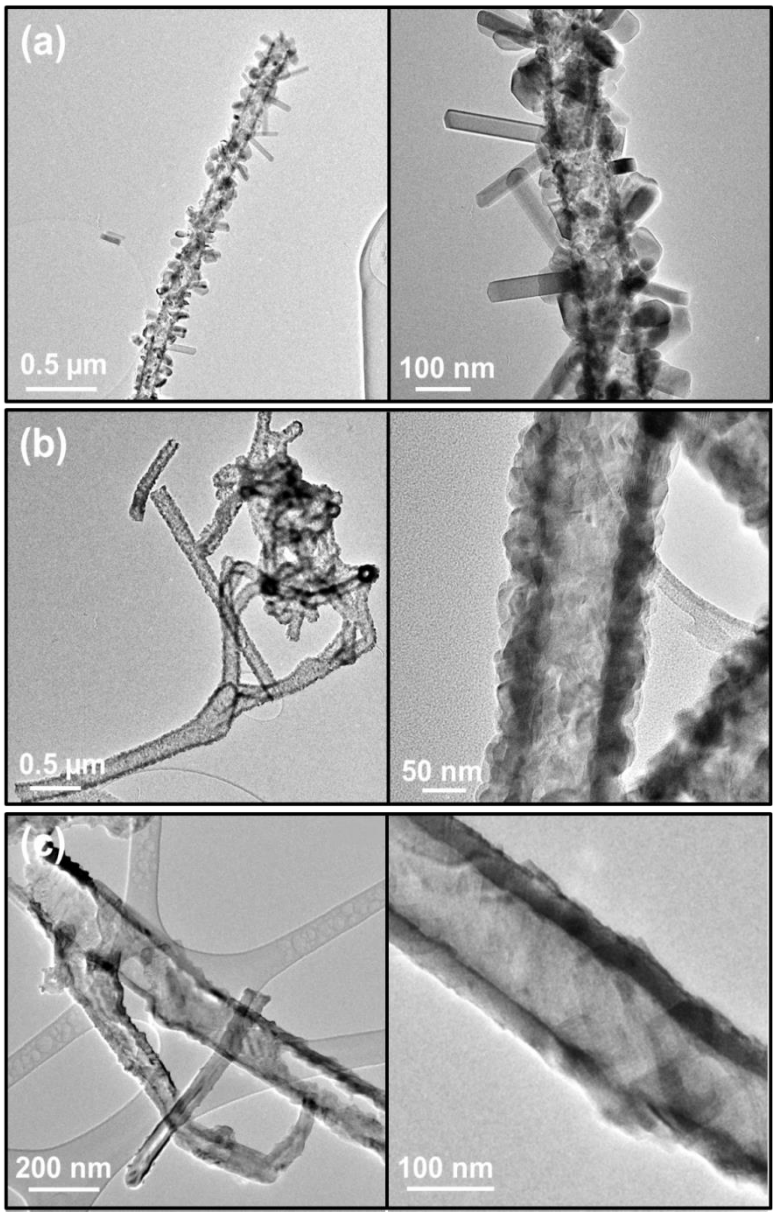

Figure 3.4. TEM characterizations for different CNF-templated3D architectures. (a) TiO_2 fiber-NR heterostructure, the nanotubular structure and TiO_2 NRs with average size of ~170 nm in length and ~30 nm in diameter. (b) TiO_2-ZnO bilayer tubular nanofibers and polycrystalline feature on the surface. (c) Fibrous TiO_2 nanotube structure with uniform wall thickness of TiO_2 and large crystalline domain area.

consistent with the typical ALD growth rate of ZnO and TiO_2. Unlike the 600 ℃ growth, the lower temperature (300 ℃) inhibited cation diffusion and exchange reactions that are required by the implementation of the Kirkendall effect. Thus, crystalline TiO_2 was simply over-coated on the ZnO surfaces and created TiO_2-ZnO bilayer tubular structure by only burning off CNF cores. Direct TiO_2 ALD on CNF templates yielded a much smoother tubular structure, as shown in Figure 3.4c. The wall of TiO_2 nanotubes was fairly uniform with a thickness of ~40 nm which is accordant with the typical TiO_2 ALD growth rate. The polycrystalline shell exhibited a much larger grain size (>100 nm) formed from subsequent high-temperature treatment (600 ℃), where the CNFs templates were also completely removed. Although CNFs have amorphous and crystalline regions, above microscopic observations they reveal no differences in morphology and crystallinity of either TiO_2 NRs or ZnO or TiO_2 overcoatings along the entire CNF surfaces. The preparation methods and representative morphologies of the three types of samples are summarized in Table 3.1.

Elemental and phase information of the three types of fibrous nanostructures were characterized to further confirmed the conclusions of structure evolution drawn from the microscopy analyses. From the 3D TiO_2 fiber-NR heterostructure, no Zn signal was detected from EDS spectrum (Figure 3.5a), nor the ZnO phase can be identified by the XRD pattern (Figure 3.5b). This verifies the fact that all ZnO shell was consumed and replaced by TiO_2 nanotube backbones during NRs integration via the Kirkendall effect. From the XRD profile, rutile TiO_2 was identified, which was believed to be a result of the

Table 3.1. Summary of observed morphologies of three types samples under different preparation methods.

CNF-templated Sample	Preparation Method	Morphology
TiO_2 fiber-NR heterostructure	ZnO ALD coating on CNFs then TiO_2 NRs growth by SPCVD	TiO_2 NRs rooted on the TiO_2 tubular nanofibers
TiO_2-ZnO bilayer tubular NFs	ZnO ALD coating on CNFs then crystalline TiO_2 ALD coating	TiO_2 and ZnO double-layer tubular nanofibers with rough surface
TiO_2 nanotubes networks	Amorphous TiO_2 ALD coating then annealing	TiO_2 tubular nanofibers

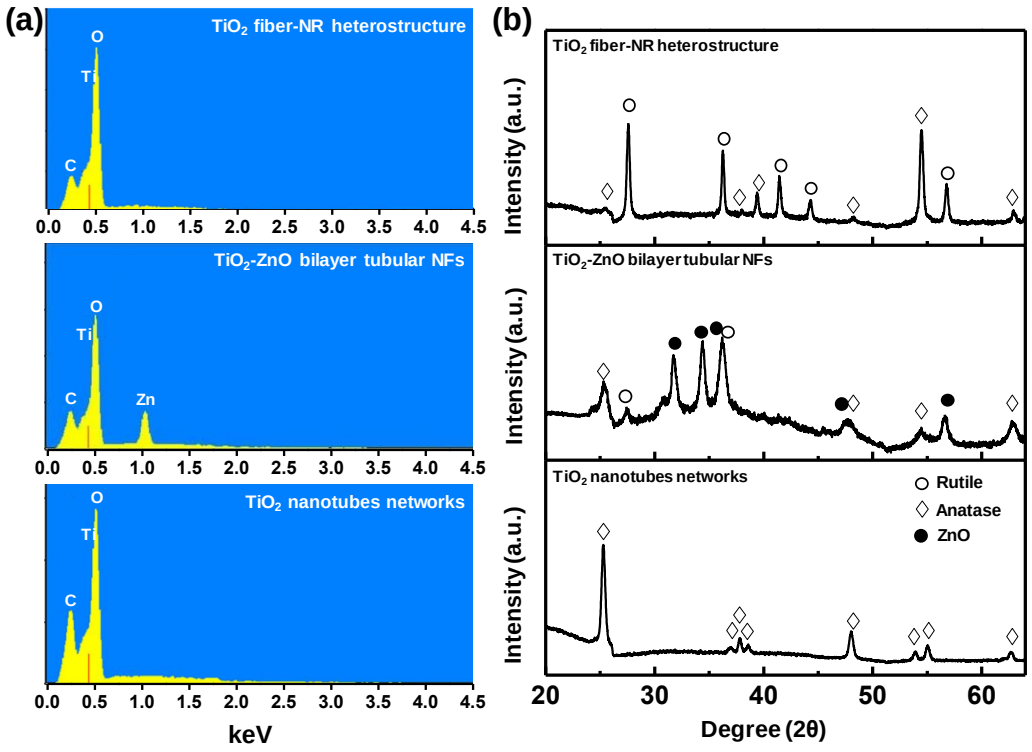

Figure 3.5. (a) EDS analysis and (b) XRD patterns reveal the conversion of ZnO template to TiO_2 and more appeared rutile phase during the 600 ℃ SPCVD process for TiO_2 NRs growth, whereas the ZnO layer was reserved and less rutile phase show up during 300 ℃ ALD process for TiO_2 films coating.

lower anatase phase stability when foreign element (e.g., Zn) was involved during the growth.[143] As expected, the TiO_2-ZnO bilayer tubular nanofibers showed a strong Zn single in the EDS spectrum and the ZnO phase can be clearly identified in the XRD pattern. Due to the existence of Zn elements, the rutile phase also appeared rather than pure anatase phase from 300 ℃ ALD TiO_2 in our earlier publication.[34] The EDS and XRD results of TiO_2 nanotube network were identical to typical ALD results as shown in our previous work,[76] where only anatase TiO_2 was observed. Notably, the EDS analysis showed distinct C signal from each sample. The amount of carbon preserved in the final products of TiO_2 fiber-NR heterostructure, TiO_2-ZnO bilayer tubular nanofibers, and TiO_2 nanotube network was identified to be ~6.2%, 7.9 %, and 14.4% respectively. Exposures of H_2O vapor during 600 ℃ TiO_2 NRs and 300 ℃ TiO_2 film growth might provide an oxidation environment and lessen the amount of reserved carbon from CNF calcination.

Due to the long optical paths and possible high quality transport channels for rapid charge separation and conduction, as well as the prominent electrolyte-semiconductor interface areas, the 3D TiO_2 fiber-NR heterostructure could be a promising mesoporous configuration for high-performance PEC photoanodes.[34,72,76,144-146] Such potential merits were explored by conducting PEC water splitting measurements. For performance comparison, the other two samples (TiO_2-ZnO bilayer tubular nanofibers and TiO_2 nanotube networks) were applied as PEC photoanodes as well. The photocurrent density (J_{ph}) versus bias potential characteristics of these three kinds of samples was measured under the same conditions. Corresponding PEC efficiencies were estimated using the

equation 2.1 that was present in previous chapter.

The representative J_{ph} $-V$ curves are shown in Figure 3.6a under the illumination of 100 W cm^{-2} Xe lamp source without and with AM 1.5G or UV cutoff filters. The dark current densities of each PEC test remained at fairly small values ($<10^{-4}$ mA cm^{-2}) within the bias potential range scanned between -0.9 V and 0.5 V (vs. SCE) indicating high quality crystal surfaces of the as-synthesized fibrous networks. In general, the 3D TiO_2 fiber-NR heterostructure exhibited high J_{ph} and efficiency under all wavelength conditions, where the highest values were obtained from the Xe lamp illumination and the lowest values when a UV cutoff filter was applied. Under Xe lamp, the maximum efficiency was calculated to be 1.13% at ~ -0.31 V. The maximum efficiency dropped to 0.76% at ~ -0.26 V for AM 1.5G filter and 0.17% at ~ -0.35 V for UV cutoff filter (Figure 3.6b). This phenomenon evidences that the performance of TiO_2 nanostructure-based photoanodes was mainly governed by UV absorption. Nevertheless, appreciable PEC performance was achieved when only visible light was illuminated. The photoactivity in the visible light region can be attributed to the presence of carbon elements as discovered in our recent study.[76]

Compared to the other two reference samples, the J_{ph} of 3D TiO_2 fiber-NR heterostructure exhibited obviously higher values under all illumination wavelength range. When illuminated directly under the Xe lamp, its maximum efficiency (1.13% at ~ -0.31 V) is 45% and 22% higher than that of the TiO_2-ZnO bilayer tubular nanofibers (0.78% at ~ -0.26V) and TiO_2 nanotube networks (0.93% at ~ -0.6 V), respectively

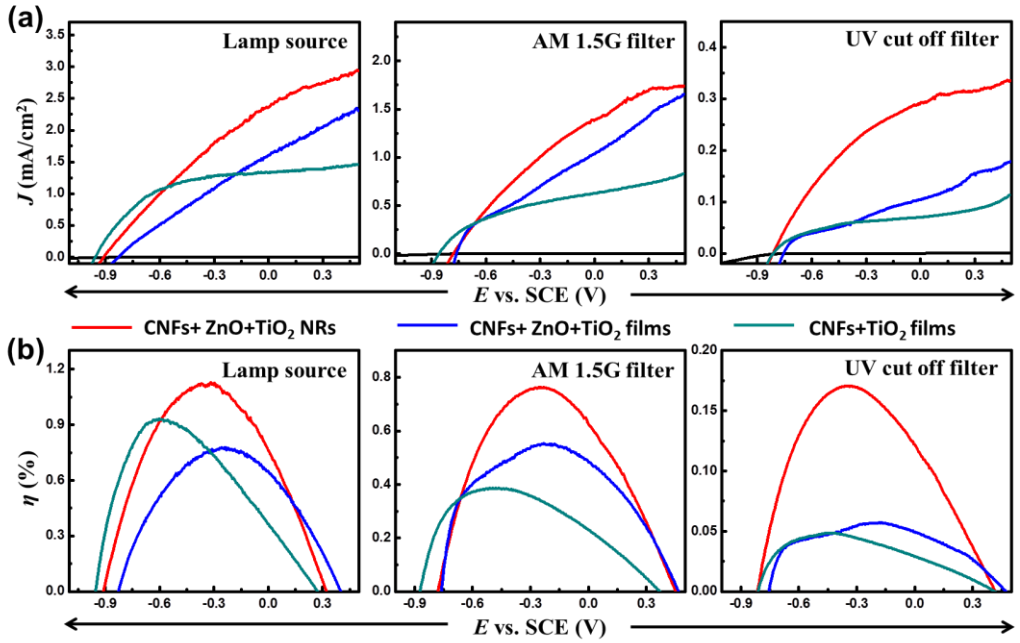

Figure 3.6. (a) Photoelectrochemical performance of three CNF-templated fibrous networks under illuminations of 100 mW cm^{-2} Xe lamp source, lamp with AM 1.5G filter, and with UV cutoff filter. (b) Corresponded PEC efficiencies for these CNF-templated3D architectures.

(Figure 3.6b). When AM1.5G and UV cut-off filter was applied, the TiO_2 fiber-NR heterostructure exhibited even higher advantages compared to the other two. Under AM1.5G illumination, its maximum efficiency was 38% and 97% higher than that of the TiO_2-ZnO bilayer tubular nanofibers and TiO_2 nanotube networks. Under only visible light, the enhancement was raised to 195% and 249% as compared to the TiO_2-ZnO bilayer tubular nanofibers, TiO_2 nanotube networks, respectively. The largest surface area is generally believed to be the main reason of the enhanced performance. However, the much more significant enhancement in the visible light region suggests that the charge transport might be the bottle neck when higher flux photogenerated charge was induced. This argument can also be supported by the shapes of $J_{ph} - V$ characteristics. As shown in Figure 3.6a, the saturation regions of both TiO_2 fiber-NRs heterostructure and TiO_2-ZnO bilayer tubular nanofibers samples were less obvious, indicating the existence of a larger number of defects and grain boundaries in these two samples acting as the recombination sites, which jeopardize the separation and transport of photogenerated charges.[147,148]

3.4. Conclusion

In this chapter, high-density 3D TiO_2 fiber-NR heterostructure was developed for efficient PEC photoanodes. 3D CNFs network with ALD ZnO shells was used as template for SPCVD growth of TiO_2 NR branches. The ZnO layer interacted with $TiCl_4$ vapor and was quickly converted into polycrystalline TiO_2 thin films seeding the growth of TiO_2 NRs. The template dimension and 3D morphology were well preserved. The structure evolution was in a good agreement with the vapor-phase Kirkendall effect in

ALD system that we discovered recently. The 3D fiber-NR heterostructure offers large porosities and tremendous surface areas for PEC water splitting. Its PEC efficiency was found to be 22%-249% higher than those of TiO_2-ZnO bilayer tubular nanofibers and TiO_2 nanotube networks that were synthesized as reference samples. The much more conspicuous photoactivity in longer wavelength region together with the J_{ph} $-V$ characteristics suggest that charge transport might be the issue for the 3D fiber-NR heterostructure to further enhance its PEC performance. This technique opens a new avenue toward cellulose-based nanomanufacturing technique which holds a great promise for large-area, low-cost, and green fabrication of functional nanomaterials, as well as their applications in solar energy harvesting and conversion areas.

Chapter 4. Capillary PEC Based on Cellulose Nanofiber-Templated 3D TiO_2 Nanoarchitectures

4.1 Introduction

Natural cellulose nanofibers (CNFs) have been successfully explored to synthesize the 3D TiO_2 fiber-NR heterostructure for PEC photoanodes in chapter 3. Such nanoarchitectures exhibited significantly enhanced photocurrent and PEC efficiency, which is attributed to their large surface area and good electrical conductivity. This successful application exploration of CNF-templated nanostructure suggests that the performance of PEC photoanodes could also be improved through directly depositing TiO_2 on CNFs for hollow TiO_2 nanofibers. In this chapter, 3D fibrous TiO_2 nanotube architecture was synthesized by ALD of titania films over CNF templates. Due to the excellent hydrophilic properties of CNF films, a capillary PEC setup was developed to perform water splitting reactions outside of the electrolyte body, where electrolyte was supplied through nano/micro-channels in the CNF film driven by capillary force. Enhanced reaction kinetics and higher efficiency were observed from the capillary PEC process. In addition, modification of the calcination atmosphere was used to engineer the chemical compounds of TiO_2 nanofibers and enable visible light photoactivity.

4.2 Experimental Section

Fabrication of CNF films: The Nanofibrillated cellulose (NFC) used in our fabrication was tetramethylpiperidine-1-oxy (TEMPO) oxidized wood pulp fiber, which

was prepared according to the method reported by Saito *et al.*[140,141] Specifically, in order to obtain a 0.4 wt%, nanofiber hydrogel, deionized water was added to the centrifuged NFC suspension before this mixture was mechanically homogenized on an M-110EH-30 Microfluidizer (Microfluidics, Newton, MA, USA) with a series of 200- and 87-μm chambers via two pass-throughs. After printing this NFC hydrogel on Fluorine doped Tin Oxide (FTO) glass substrates, the substrate with the hydrogel film was frozen by liquid nitrogen and ethanol bath. Next, the substrate was immediately and quickly transferred into the vacuum chamber of a Labconco 4.5 Freeze Dryer (Labconco, Kansas City, MO, USA) with stable pressure about 35 mTorr for 12 hours at room temperature, where sublimation of the ice yielded a nanofibrous structure cellulose film, 10 μm thick on the FTO.

Fabrication of TiO_2 nanotube photoanodes: The CNF films were loaded in ALD chamber for amorphous TiO_2 overcoating at 150 ℃. The ALD growth cycle consisted of 0.5 s H_2O pulsing + 60 s N_2 purging + 0.5 s titanium tetrachloride ($TiCl_4$) pulsing + 60 s N_2 purging. 350 cycles yielded 30 nm thick amorphous TiO_2 coating. The CNF-amorphous TiO_2 core-shell structures were annealed in oxygen (600 ℃, 24 hours, 390 mTorr) or vacuum (600 ℃, 24 hours, 55 mTorr) to convert the amorphous TiO_2 into anatase phase. Through this process, CNFs were also removed leaving TiO_2 nanotube structures. Then, another thin film of anatase TiO_2 was coated onto the entire sample by 400-cycle ALD at 300 ℃ to make a continuous cover of the TiO_2 fibrous nanotubes and exposed FTO area. The last step was further annealing the samples in oxygen at 500 ℃ for 10 hours to eliminate carbonized cellulose residues outside of the TiO_2 crystals to

avoid possible undesired electrochemical reactions during PEC measurement.

PEC setup and characterization: The TiO_2 nanotube networks on FTO substrate were covered by epoxy leaving an exposed active area of ~0.6 mm^2 as the photoanode. For capillary PEC setup, an additional CNF strip was adhered on the bottom side of the TiO_2 nanotube array. PEC measurements were performed in a 1 $molL^{-1}$ KOH (pH=14) aqueous solution using a three-electrode electrochemical cell configuration. Both the conventional in-electrolyte PEC setup (immerse all active area into the KOH electrolyte) and the new capillary PEC setup (only bottom part of the cellulose strip was immersed in to KOH electrolyte) were utilized in the performance characterization of TiO_2 fibrous photoanodes. In PEC measurements, a saturated calomel electrode (SCE) was used as the reference electrode and a Pt wire was used as the counter electrode. All electrodes were connected to a potentiostat system (Metrohm Inc., Riverview, FL) for *J-V* characterization. Light illumination was provided by a 150W Xe arc lamp (Newport Corporation, Irvine, CA) and the intensity at the PEC anode position was adjusted to be 100 $mWcm^{-2}$. An AM 1.5G filter and a UV cut off filter were also utilized with the lamp for PEC characterization.

4.3 Calculation Section

4.3.1 The potential change of the redox couple between new pH solution and pH=14 solution

The relation between the Fermi level of the redox couple and their concentrations is represent by the equation:[149]

$$E_{F,redox} = {}^{0}E_{redox} + kTln\left(\frac{[Red]}{[Ox]}\right) \quad (4.1)$$

where ${}^{0}E_{redox}$ is the standard redox potential of the redox couple.

For $4OH^- \rightarrow 2H_2O + O_2 + 4e^-$

[Red] = $[OH^-]$, [Ox] = $[O_2]$ = P_{O_2}

At pH =14,

$$E^1_{F,redox} = {}^{0}E_{redox} + kTln(\frac{1}{P_{O_2}}) \quad (4.2)$$

Also, $[H^+][OH^-] = 10^{-14}$ => $[OH^-] = 10^{-14}/[H^+]$

At new pH value,

$$E^2_{F,redox} = {}^{0}E_{redox} + kTln(\frac{10^{-14}}{P_{O_2}[H^+]}) \quad (4.3)$$

Thus, the potential change of the redox couple between new pH solution and pH=14 solution follow the euqtion:

$$\begin{aligned} \Delta\varphi_1 &= E^2_{F,redox} - E^1_{F,redox} \\ &= \frac{kT}{lge} lg\left(\frac{10^{-14}}{[H^+]}\right) \\ &= \frac{kT}{lge}(pH - 14) \\ &= 0.059(pH - 14) \end{aligned} \quad (4.4)$$

4.3.2 The relation between the Fermi level of the semiconductor and the number of accumulated holes

From interruption *J-V* test curve (black) and the related regular curve (red), the area between them is related to the number of accumulated holes on the semiconductor surface. Read the data (V_0, J_0) at t_0 and (V_1, J_1) at t_1 on black curve.

Based on the RC circuit model:

$$I(t) = I_0 e^{-\frac{t}{\tau_0}} = \frac{dQ(t)}{dt} \quad (4.5)$$

$$Q_0 = CV_0 \quad (4.6)$$

$$I_0 = V_0/R = Q_0/RC = Q_0/\tau_0 \quad (4.7)$$

where I_0 is the initial current and τ_0 is the time constant of the system.

Thus,

$$I(t) = (Q_0/RC)e^{-\frac{t}{\tau_0}} \quad (4.8)$$

Let $t=t_1-t_{0,}$ where t can be achieved by $(V_1-V_0)/S$, S is the scan speed =0.05V/s.

Put (J_0, 0) and (J_1, t) into the equation to get the value of Q_0 (C cm^{-2})

For traditional PEC case and capillary PEC case, the average Q_0/e value were obtained as 8.24×10^{12} (cm^{-2}) and 3.43×10^{12} (cm^{-2}). The thickness of the TiO_2 nanotube film was ~10 μm. The holes concentration should be approximately 8.24×10^{15} (cm^{-3}) and 3.43×10^{15} (cm^{-3}).

The appearance of transients diminishes at higher potential as a larger proportion of holes have sufficient potential to oxidize water.[150] Also, previous research mentioned that the magnitude of the transient decreases with increasing positive bias. This effect can be understood by considering that positive potentials increase the band bending.[151] Therefore, the exploration of difference on the number of accumulated holes for two cases can be considered to investigate the difference of band bending in two cases. Band bending is strongly related to the Fermi level of the semiconductor. So, from the equations:

$$E_i - E_{f_1} = kTln(\frac{N_1}{N_i}) \quad (4.9)$$

$$E_i - E_{f_2} = kTln(\frac{N_2}{N_i}) \quad (4.10)$$

For our ALD synthesized n-type TiO_2, if we assume N_1 is the carrier concentration in this TiO_2, $N_2 = N_1 + \Delta N$, where ΔN (>0) is the change of holes concentration from above calculation.

$$\begin{aligned} \Delta\varphi_2 &= E_{f_1} - E_{f_2} \\ &= kTln\left(\frac{N_2}{N_1}\right) \\ &= kTln\left(1 + \frac{\Delta N}{N_1}\right) \end{aligned} \quad (4.11)$$

$\Delta N \sim 5\times10^{15}$($cm^{-3}$). Typically, for n-type TiO_2, $N_1 = \sim10^{17}$ (cm^{-3}).

4.3.3 The relation between section 4.3.1 and section 4.3. 2.

The water oxidation happened when there is a certain gradient between the potential of semiconductor and the potential of the electrolytes. Assume this value will not change for our TiO_2 - KOH system. Also, the transient behavior is related to surface states which depend on the crystalline quality of the surface. This can be modified by the synthesis technique. In two PEC cases, the TiO_2 nanotube sample did not change. The calculated potential difference for the semiconductor described in section 2 is actually the potential difference for KOH solution.

Combine equation (4.4) and equation (4.11), let $\Delta\varphi_1 = \Delta\varphi_2$

$$0.059(pH - 14) = kTln\left(1 + \frac{\Delta N}{N_1}\right) \quad (4.12)$$

If $N_1 \sim 10^{17}$, $\Delta N \sim 5\times10^{15}$, kT~0.025eV

pH $\approx$ 14.02

4.4 Results and Discussion

The CNF films were fabricated at wafer-scale via freeze-drying approach as shown in the inset of Figure 4.1a. SEM revealed a highly-porous network structure composed of dense CNFs (Figure 4.1a). The fibrous nanostructure was well preserved after 150 ℃ ALD of TiO_2 thin film conformal coating, yielding an overall fiber diameter of ~100 nm (Figure 4.1b). The amorphous TiO_2 coating was then crystallized by annealing the sample at 600 ℃ for 24 hours under controlled conditions (see experimental section for details). The annealing treatment crystalized the amorphous TiO_2 coating as well as burned away the CNF templates. It is noteworthy that the fibrous 3D network structure was very stable during the vigorous heat treatment and no obvious dimension or morphology change could be observed (Figure 4.1c), except that the core-shell fibers were converted into TiO_2 nanotubes (inset of Figure 4.1c).

The crystal structure of CNF-templated TiO_2 nanotubes were further investigated by TEM. Low-magnification TEM images clearly demonstrated the tubular TiO_2 nanostructure after annealing (Figure 4.1d). Thickness of the TiO_2 layer was identified to be 25~30 nm which was consistent with the 350 cycles of ALD (Figure 4.1e). The TiO_2 nanotubes are polycrystalline with a fairly large single-crystalline domain (~20-50 nm in one dimension). HRTEM revealed a single-crystalline domain region obtained from the TiO_2 nanotube. The crystal lattice spacing and the diffraction pattern from fast Fourier transform (FFT) suggest the anatase phase of the TiO_2 nanotubes. Powder X-ray diffraction (XRD) further confirmed the pure anatase TiO_2 phases after 24 hours

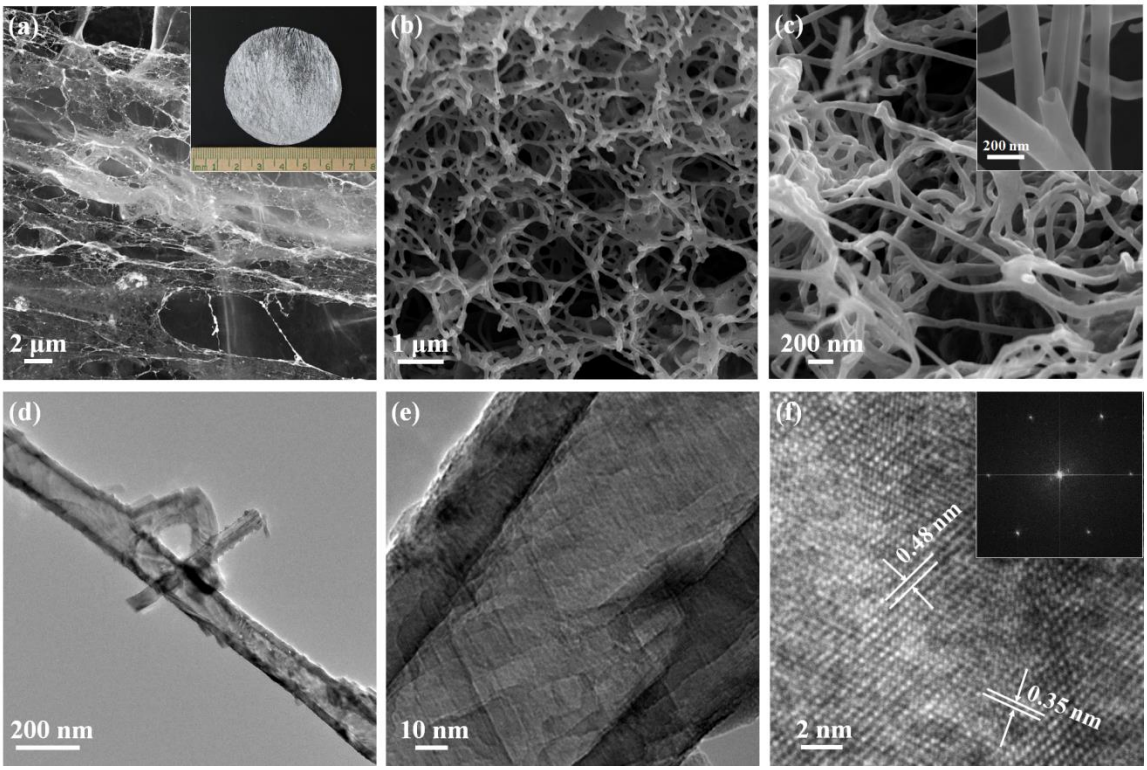

Figure 4.1. Morphology and structure of CNF films and templated TiO_2 nanotube structures. (a) CNF film processed on a FTO substrate; inset is a single piece of CNF film fabricated in large scale. (b) CNFs coated with TiO_2 via 350 cycles ALD at 150 ℃. (c) Fibrous TiO_2 nanotube network after annealing at 600 ℃ for 24 hours; inset shows an enlarged broken tip revealing the hollow tubular structure. (d) TEM image of a hollow TiO_2 nanotube obtained after annealing. (e) Higher resolution TEM image showing the uniform thickness of TiO_2 walls and large crystalline domain area. (f) HRTEM image showing the single-crystal region obtained from the TiO_2 shell. The lattice spacing and FFT (inset) suggest the anatase phase.

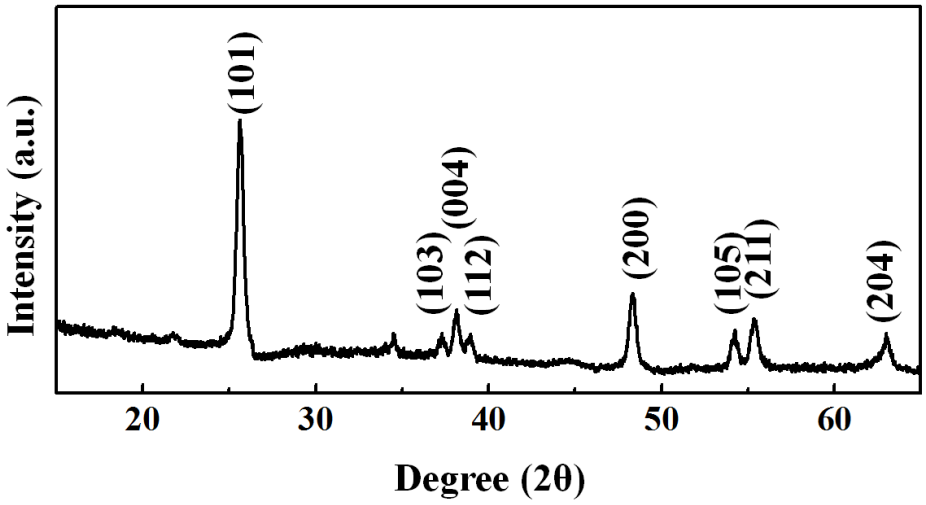

Figure 4.2. XRD spectrum of fibrous TiO_2nanotubes after annealing, confirming its anatase phase.

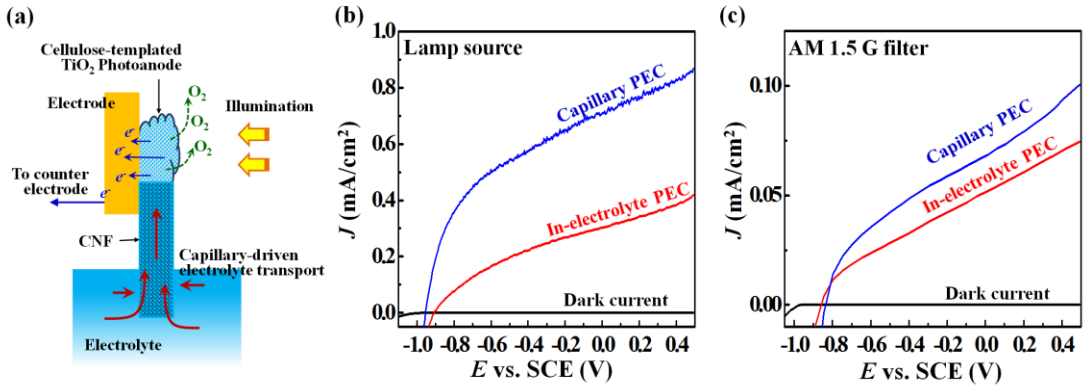

Figure 4.3. Capillary PEC water splitting setup and performance. (a) Schematic illustration of the capillary PEC setup. (b, c) *J-V* characteristics of a cellulose-templated TiO_2 photoanode measured using capillary setup and in-electrolyte setup under 100 mW cm^{-2} Xe lamp source without (b) and with (c) AM 1.5G filter.

annealing treatment (Figure 4.2).

The PEC performance of the CNF-templated TiO_2 nanotube network and the unique capability of CNF in PEC cell development were investigated using an out-of-electrolyte capillary PEC system, as schematically shown in Figure 4.3a. The active TiO_2 nanotube photoanode was placed on a conductive substrate and covered by epoxy, leaving an exposed area at the center. The photoanode bottom was in contact with a CNF film strip that was used to draw and transport electrolyte to the TiO_2 photoanode surface. The entire testing setup is shown in Figure 4.4. In this PEC design, the photoanode was placed outside of the electrolyte surface. Due to the excellent hydrophilic property of CNF, capillary force could drive the electrolyte to the active area quickly and continuously. Enhanced PEC reaction kinetics could be expected from the dynamic and infinitesimal electrolyte supply.

To investigate the performance of this capillary PEC design, the photocurrent density (J_{ph}) versus bias potential characteristics of both capillary PEC and conventional in-electrolyte PEC setups were measured under the same conditions. The representative *J-V* curves are shown in Figure 4.3 b and c under the illumination of 100 W cm^{-2} Xe lamp source without and with AM 1.5G filter, respectively. The dark current densities of both setups remained at small values ($<10^{-4}$ $mAcm^{-2}$) within bias potentials scanned between -1.2 V and 0.5 V (vs. SCE) demonstrating a high quality of the crystal surfaces of fibrous TiO_2nanotubes. Generally, J_{ph} was significantly higher under Xe lamp than that under AM 1.5G filter (e.g. 0.87 vs. 0.10 $mAcm^{-2}$), because a large amount of UV light was cut

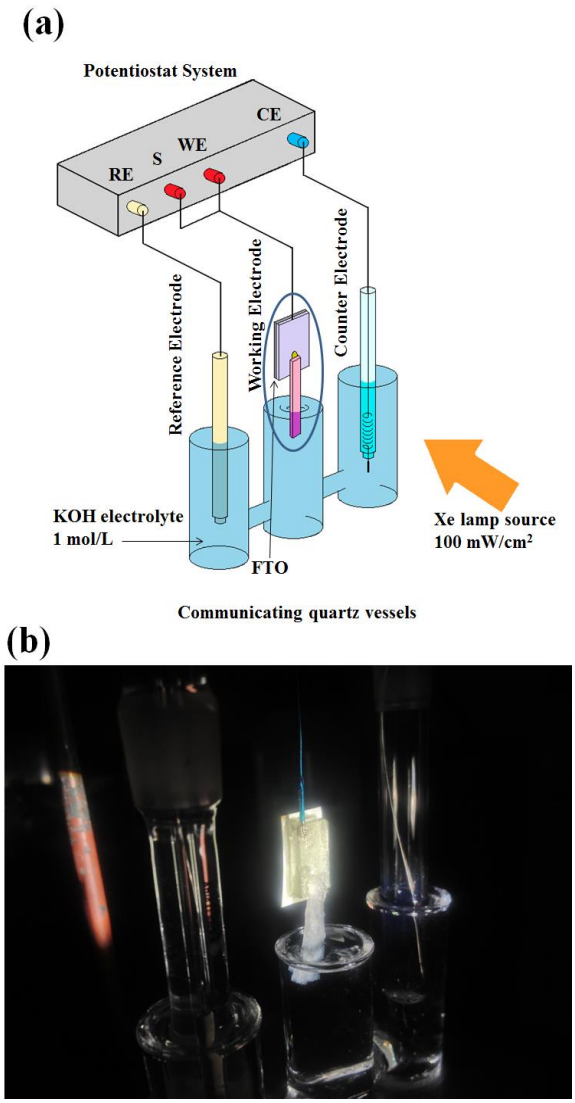

Figure 4.4. Schematic illustration (a) and a photo (b) of capillary PEC setup.

off by the filter. This phenomenon suggests that the performance of fibrous anatase TiO_2nanotubes photoanode was dominated by UV absorption. Under Xe lamp illumination, as shown in Figure 4.3b, J_{ph} measured from the capillary PEC setup ($J_{ph,ex}$, blue curve) was more than twice as much as that from the in-electrolyte setup ($J_{ph,in}$, red curve). Corresponding efficiencies were calculated by equation 2.1.

The capillary setup exhibited a maximum efficiency of 0.45% at ~-0.65 V; whereas the in-electrolyte setup had only a maximum efficiency of 0.16% at ~-0.45 V **(**Figure 4.5a**)**. When AM 1.5G illumination was applied, both $J_{ph,ex}$ and $J_{ph,in}$ were significantly decreased. Although $J_{ph,ex}$ was still higher than $J_{ph,in}$, their difference became much smaller (Figure 4.3c). Following Equation 2.1, the maximum efficiencies of capillary and in-electrolyte PEC processes were found to be 0.04% at ~-0.45 V and 0.03% at ~-0.35 V, respectively (Figure 4.5b). Meanwhile, the saturation regions of both curves were less obvious, indicating the lower UV intensity may not generate sufficient electrons/holes to saturate the surface or defect trapping states, which facilitated the recombination of photoexcited electrons and holes.[72,152,153]

The stability of the cellulose-temperature TiO_2 3D fibrous photoanode and the capillary PEC configuration was further evaluated by measuring J_{ph} at a constant bias of 0.3 V (vs. SCE) under 100 $mWcm^{-2}$ Xe lamp illumination. After an initial drop of 1.4% (J_{ph} changed from 0.73 to 0.72 mA cm^{-2}) during the first 60 minutes, J_{ph} remained at 0.72 $mAcm^{-2}$for 12 hours without appreciable further decrease (Figure 4.6). This measurement confirms good structural and functional stability of the TiO_2 photoanode. It also suggests

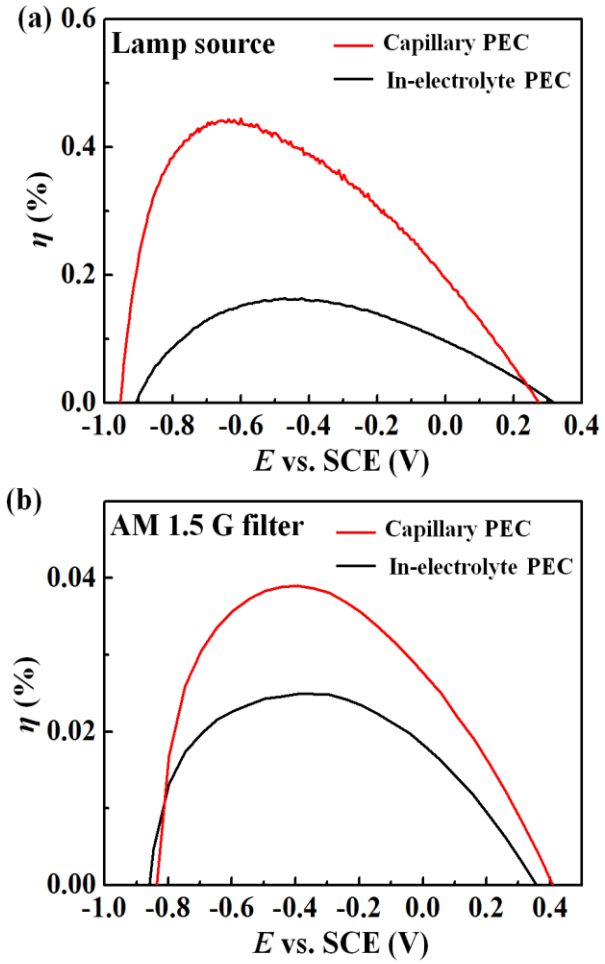

Figure 4.5. Calculated efficiencies versus bias voltages for capillary and in-electrolyte PEC setups using cellulose-templated TiO_2photoanodes annealed in O_2 atmosphere. (a) Under Xe lamp illumination. (b) Under AM 1.5 G illumination.

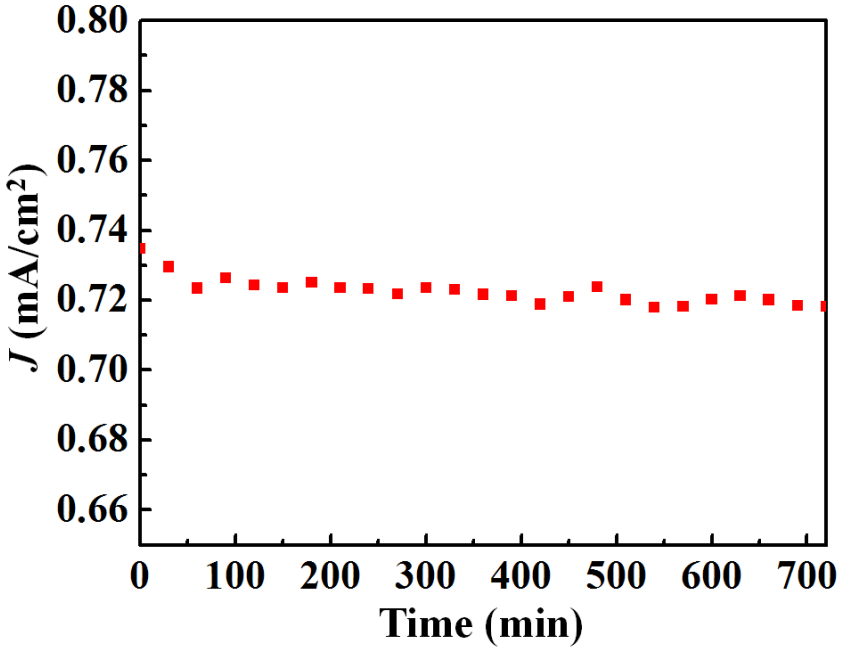

Figure 4.6. Stability test of capillary PEC setup under 0.3V (vs. SCE) bias for 12 hours.

that the capillary PEC design could function continuously and stably without any electrolyte transport or local reaction kinetic variation issues.

In order to understand performance enhancement from the capillary PEC design, a series of analyses were performed on the reaction environment and kinetics. Firstly, it is intuitive to imagine that less electrolyte body volume in front of the photoanode would result in higher light intensity that can be practically absorbed. Thus, the power densities of the illumination at fixed distances from the lamp were quantified. A linear decrease of the power density was found showing a rate of ~9.1mW cm^{-2} per 1 cm passing length through 1 $molL^{-1}$ KOH electrolyte **(**Figure 4.7**)**. Therefore, the capillary PEC design has the least amount of electrolyte covering the photoanode surface, which ensures the highest intensity of available light for absorption. This advantage becomes particularly significant when large amounts of photo-catalyst need to be applied within a confined volume of electrolyte.

Secondly, by performing *J-V* measurement under interrupted illumination, we found the reaction kinetics was slightly enhanced in the capillary PEC design. Figures 4.8a and b compare the *J-V* curves of the same TiO_2 fibrous photoanode collected from capillary and in-electrolyte setups under interrupted 100 $mWcm^{-2}$ Xe lamp illumination. Both dark currents were negligibly low while the J_{ph} profiles followed a similar trace as those shown in Figure 4.3b. For in-electrolyte setup, the emblematical anodic current spike was obvious at the point when the illumination was on (Figure 4.8a and inset); whereas from the capillary PEC setup, such spikes were less distinguishable (Figure 4.8b and inset).

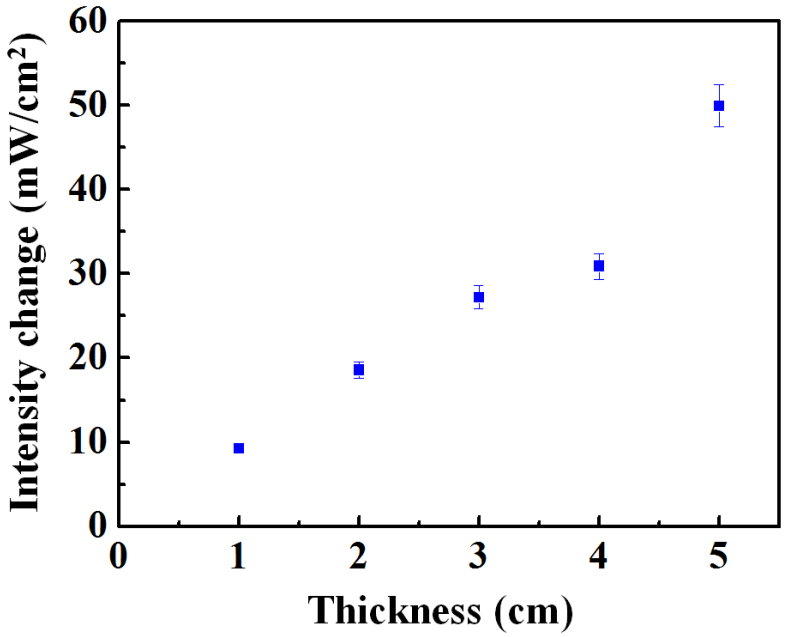

Figure 4.7. Illumination intensity decreases as a function of electrolyte (1M KOH) thickness that light passes through. The linear relation is consistent with the Beer–Lambert law.

These current spikes are known by evidence of accumulated photoexcited holes at the semiconductor-electrolytes interface.[150] They are a result of carrier oxidized trap states of the semiconductor,[154] or slow oxygen evolution reaction kinetics.[151,155] Such spikes can be suppressed when photoexcited holes experience less or no barrier to oxidizing the electrolyte under better interface charge transport kinetics.

Based on above discussion, the photo-oxidation reaction kinetics at TiO_2 surfaces can be compared for both PEC setups from the shape of spikes. From the area under the anodic current spike, the number of accumulated holes at the TiO_2-electrolyte interface can be estimated (Inset of Figures 4.8a and b), which is analogous to calculating the amount of accumulated charges in a capacitor of an RC circuit by Equation 4.5. For our situation, the area density (cm^{-2}) of accumulated holes can be approximated by integrating $J(t)dt$. From both *J-V* curves in Figures 4.8a and b, the accumulated hole densities were estimated to be $8.24\times10^{12}\ cm^{-2}$ for in-electrolyte PEC and $3.43\times10^{12}\ cm^{-2}$ for capillary PEC.

The lower interfacial hole concentration suggests a lower transient over potential ($\Delta\varphi$) for oxidation reactions (see details in calculation section). Because identical TiO_2 fibrous photoanodes were used in both cases, $\Delta\varphi$ (eV) is likely associated with the Fermi level shift of the redox couple in the electrolyte, which is directly related to the pH value in our KOH system following Equation 4.4.[149] The pH values corresponding to the over potential found in the capillary case was calculated to be ~14.02, suggesting the OH^- concentration is slightly higher than the actual electrolyte concentration (1M KOH,

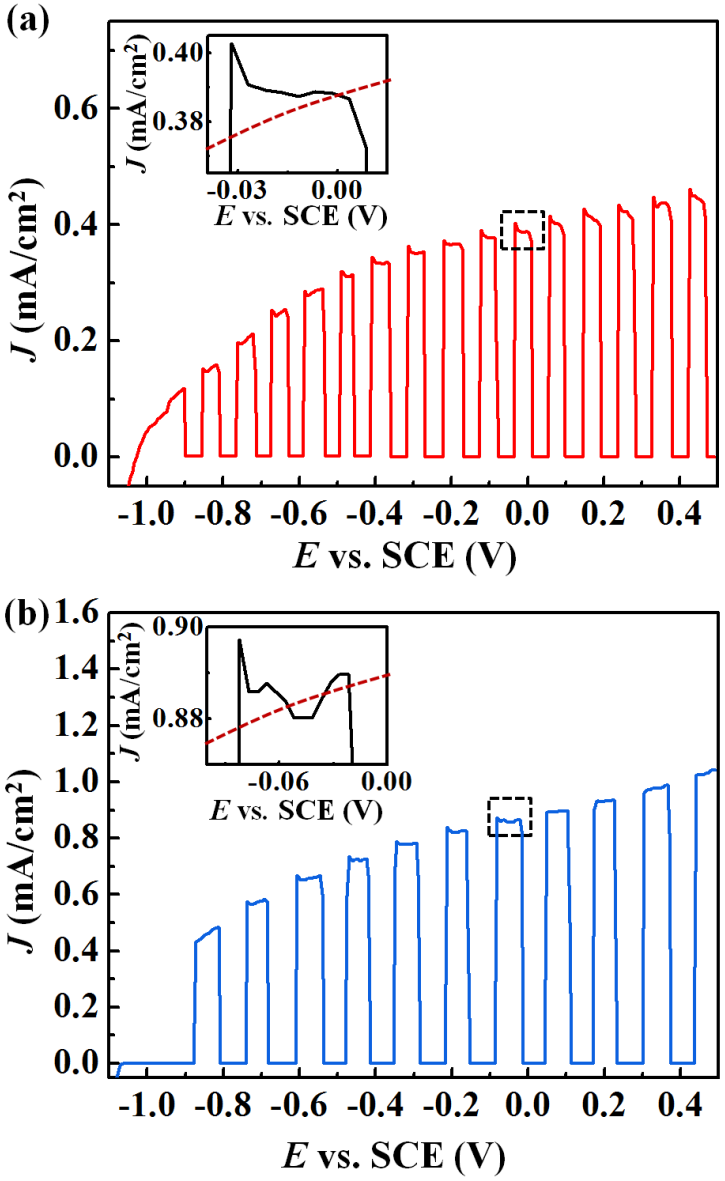

Figure 4.8. *J-V* characteristics of cellulose-templated TiO_2 photoanodes measured under interrupted illumination using in-electrolyte PEC setup (a) and capillary PEC setup (b). Insets are enlarged top regions of one J_{ph} cycle showing the feature of the initial current spikes.

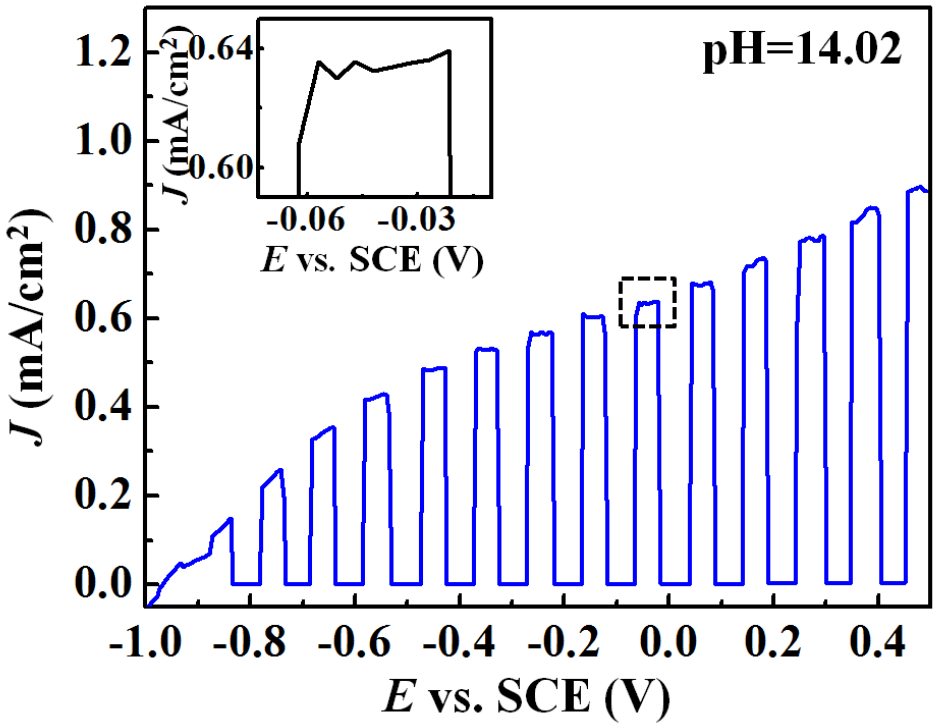

Figure 4.9. *J-V* characteristics of cellulose-templated TiO_2 photoanodes measured under interrupted illumination using in-electrolyte PEC setup, where the pH value of electrolyte was 14.02. Inset is enlarged top regions of one J_{ph} cycle showing the flatness of initial current.

pH=14). To further confirm the pH relationship, in-electrolyte PEC was conducted using the same TiO_2 photoanode under interrupted illumination in KOH electrolytes with pH=14.02, 14.2, respectively (Figures 4.9). Compared to the result shown in Figure 4.8a, most anodic current spikes disappeared at higher pH values. We believe higher pH value at the photoactive site was possibly due to solvent volatilization during electrolyte transport through cellulose film. This effect is beneficial to local reaction kinetics. However, it may become impedimental in practical applications when the transportation path is too long and where the electrolyte may completely dry out. This limitation can be circumvented by encapsulating the cellulose transport path.

Another significant merit of using cellulose nanofiber as templates is its ability to modulate the chemical composition of ultimate TiO_2 nanostructures. Previous measurements were all based on fibrous anatase TiO_2 nanotubes processed by annealing in O_2 atmosphere, where the cellulose nanofibers were completely removed and the final structure appeared pure white (low right picture in Figure 4.10a). However, when annealed in vacuum (600 ℃, 24 hours, 55 mTorr), the resulting TiO_2 nanostructure turned black, though the cellulose nanofiber cores were also fully removed (Figure 4.11). EDS analysis showed an appreciable amount of carbon (~10%) was preserved in the final TiO_2 product **(**Figure 4.12**)**. The existence of carbon in TiO_2 and the resultant black color suggests significant visible light absorption and possible visible light photoactivity of the TiO_2 photoanode, which may further enhance the PEC performance. To test this hypothesis, both capillary and in-electrolyte PEC setups were applied to characterize the

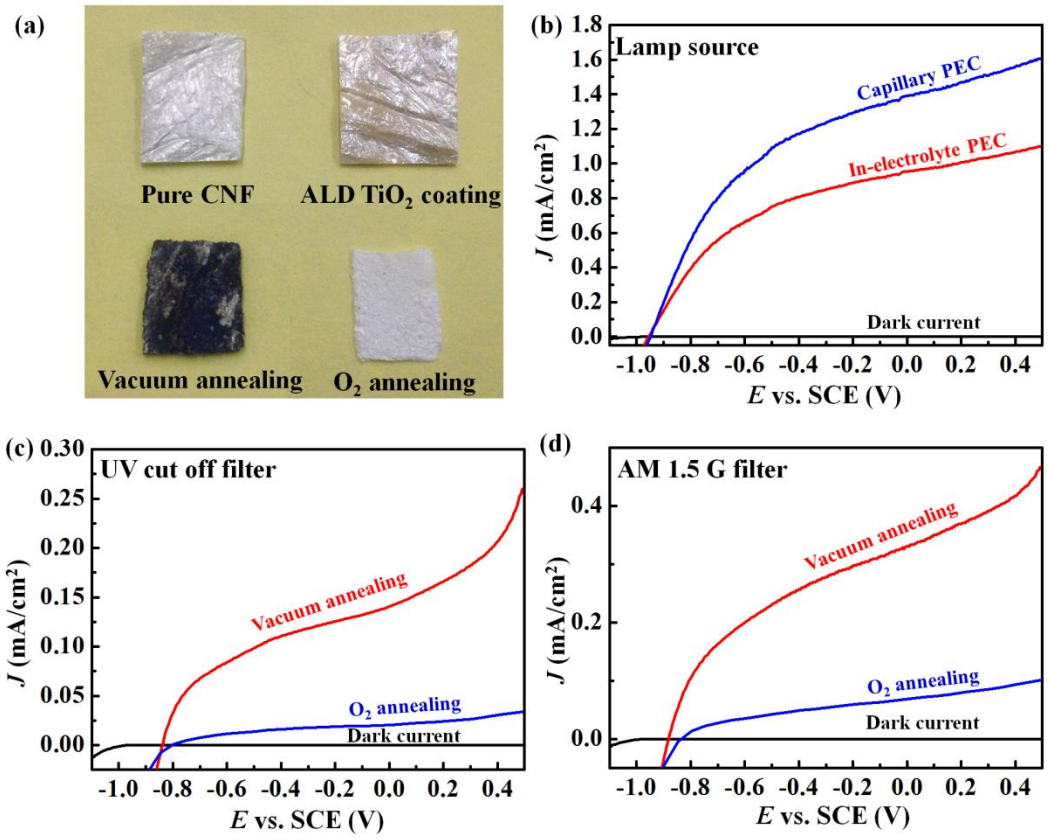

Figure 4.10. Effect of TiO_2 composition control. (a) Photos of CNF films before and after TiO_2 coating, and after annealing in vacuum and oxygen atmosphere. (b) J-V characteristics of "black" cellulose-templated TiO_2photoanode measured using capillary and in-electrolyte PEC setups. (c, d) Performance comparisons of cellulose-templated TiO_2photoanodes annealed in vacuum (red curves) and in oxygen (blue curves) measured with UV cutoff filter (c) and AM 1.5 G filter (d). All the curves were measured using capillary PEC setup.

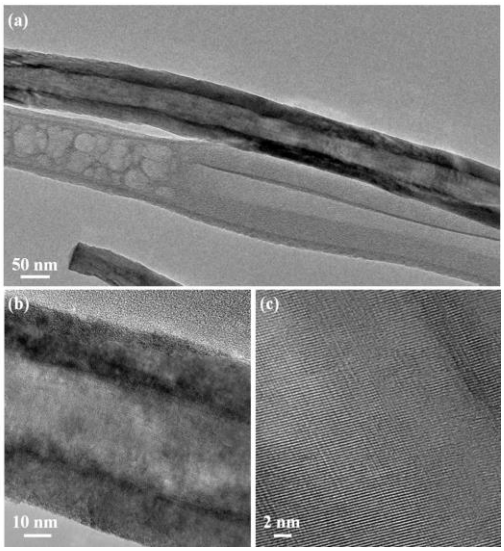

Figure 4.11. (a) TEM image of fibrous TiO_2 nanotubes obtained after 600 ℃ 24 hours annealing in vacuum. (b) TEM image showing TiO_2 wall with uniform thickness. (c) HRTEM image of TiO_2 wall showing good crystallinity.

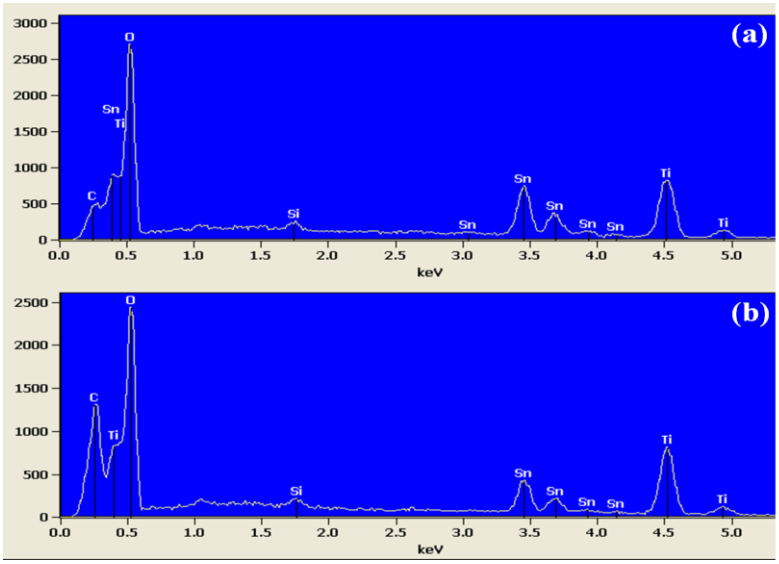

Figure 4.12. EDS spectra of fibrous TiO_2nanotube samples after 600 ℃ annealing for 24 hours under the environment of O_2atmosphere (a) vacuum (b). The observed average elemental content of carbon (atom %) was 5.713% for TiO_2 annealed in O_2 atmosphere; and 10.025% for TiO_2 annealed in vacuum. The "Si" peak and "Sn" peaks came from the FTO glass substrate.

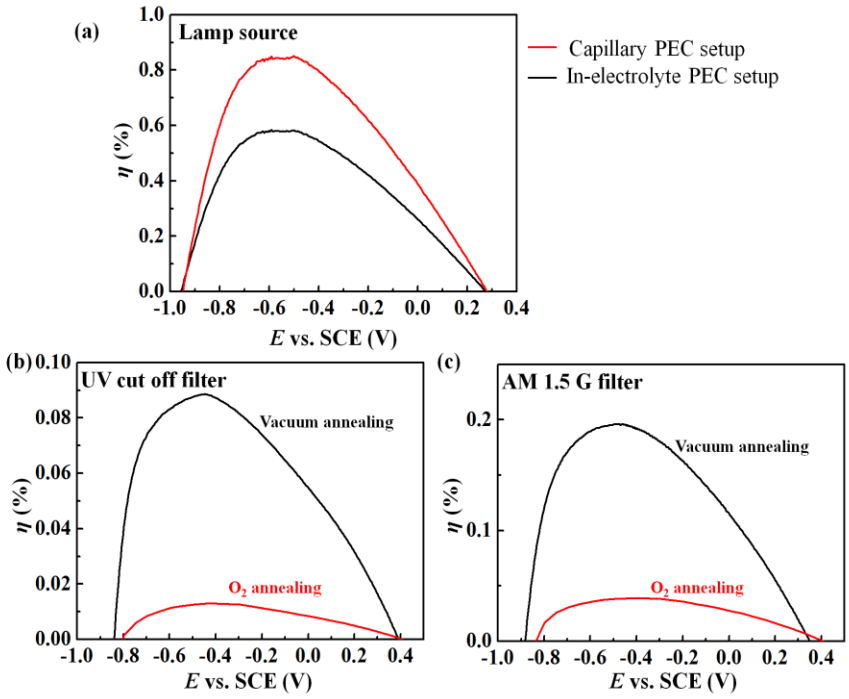

Figure 4.13. (a) Calculated efficiencies of "black" cellulose-templated TiO_2 photoanode measured using capillary and in-electrolyte PEC setups under Xe lamp illumination. (b, c) Calculated efficiencies of cellulose-templated TiO_2 photoanodes annealed in vacuum (black curves) and in oxygen (red curves) measured with UV cutoff filter (c) and AM 1.5 G filter (d). All the curves were measured using capillary PEC setup.

J-V curves under Xe lamp illumination. As shown in Figure 4.10b, both setups exhibited higher J_{ph} compared to the results from "white" TiO_2 photoanode (Figure 4.3b). Following Equation 2.1, the maximum efficiencies of the "black" TiO_2 photoanode were identified to be 0.85% and 0.58% for capillary and in-electrolyte setups, respectively.

The possible visible light photoactivity was further investigated by comparing the "black" and "white" fibrous TiO_2 photoanodes using the same capillary PEC setup and AM 1.5G and visible light (UV filter applied) illuminations, as shown in Figure 4.10 c and d, respectively. Under both illumination conditions, J_{ph} from the "black" TiO_2 photoanode was almost an order of magnitude higher than that from the "white" TiO_2. Corresponding efficiencies were calculated (Figure 4.13) and summarized in Table 4.1 for comparison. In general, J_{ph} and PEC efficiencies of capillary setups were higher than those obtained from in-electrolyte setup owing to less electrolyte-related light scattering and better local reaction kinetics. For both PEC setups, the vacuum annealed TiO_2 nanostructures exhibited significantly higher PEC performance compared to the ones annealed in oxygen due to the activation of visible light photoactivity. This comparison clearly shows that the capillary PEC design is able to further enhance the PEC performance in addition to those can be achieved by other strategies, such as optimizations of light absorption, surface/interface properties and charge transport. Given other key kinetic factors being well engineered, the maximum PEC efficiency could be raised to a higher level by the implementation of the capillary PEC design.

Table 4.1. Summary of Photocurrent Densities and PEC Efficiencies of Fibrous TiO_2 photoanodes measured under different conditions.

PEC set up	Annealing ambient	UV cut off filter	AM 1.5 G filter	J (mA cm^{-2})	η (%)
Capillary setup	Oxygen	No	No	0.87	0.45
	Oxygen	No	Yes	0.10	0.04
	Oxygen	Yes	No	0.03	0.01
	Vacuum	No	No	1.61	0.85
	Vacuum	No	Yes	0.47	0.20
	Vacuum	Yes	No	0.26	0.09
In-electrolyte setup	Oxygen	No	No	0.42	0.16
	Oxygen	No	Yes	0.08	0.03
	Oxygen	Yes	No	0.02	0.01
	Vacuum	No	No	1.10	0.58
	Vacuum	No	Yes	0.32	0.15
	Vacuum	Yes	No	0.15	0.07

4.4 Conclusion

In this chapter, 3D CNF networks were used as templates for fabricating PEC photoanodes *via* ALD of TiO_2. Annealing the cellulose-TiO_2 core-shell nanostructures created anatase TiO_2 nanotube 3D architecture, which offered tremendous surface area for PEC water splitting. Based on the excellent hydrophilic property of cellulose, a novel capillary PEC setup was developed. Capillary force quickly and continuously transported electrolyte to the photoanode surface during PEC water splitting. Better reaction kinetics and higher efficiency are achieved from the capillary PEC designs compared to conventional in-electrolyte PEC reactions. In addition, annealing the cellulose-TiO_2 core-shell structure in vacuum preserved the carbon elements in TiO_2, and thus activated photoactivity in the visible light region. The cellulose-based nanomanufacturing technique holds a great promise for large-area, low-cost, and green fabrication of functional nanomaterials. Using cellulose for capillary PEC design mimics the mass transport process in natural photosynthesis, where the interaction between light and reaction sites is no longer limited by the volume, surface and depth of electrolyte. Therefore, it offers a band new solution for improving the throughput of PEC reactions.

Chapter 5. Pt-TiO_2 Nanofiber Network for Efficient Capillary Photocatalytic H_2 Generation

5.1 Introduction

Hydrogen (H_2) fuel is a very promising green and sustainable energy source with high energy capacity and zero emission.[156] However, ~95% of the current H_2 supply in the world depends on reforming fossil fuels, which is unsustainable and generates greenhouse gas such as CO_2 in atmosphere.[157] Therefore, producing H_2 from renewable sources holds great promises to solve the energy crisis and tackle the global warming issue.[124] Integrating platinum (Pt) with TiO_2 surfaces has been found to be a very promising catalyst combination for photocatalyzed redox reactions for H_2 evolution owing to their high stability for long lifetime and large Schottky barrier efficient electron-hole separation.[158,159] With the addition of sacrificial reagents as electron donor/acceptor,[160,161] such photoexited electrons and holes can be consumed irreversibly to further improve the photocatalytic reaction efficiency.[162] Although more Pt is believed to be beneficial for tolerating more photoexited electrons to facilitate photocatalytic reaction,[163] the optimal amount of Pt loading on photocatalysts, either by photo deposition[164-166] or chemical reduction,[163,167] was usually below ~5% This is possibly because excess Pt could compete for the photocatalytic sites on TiO_2 surfaces for sacrificial reagents adsorption resulting in low H_2 throughput.[163,168] Besides, other valence states of Pt, such as platinum oxide (PtO) or platinum dioxide (PtO_2), also might

co-exist with elemental Pt due to pH variation in Pt impregnation processes, which jeopardize the catalytic capability of metallic Pt.[164,169]

In addition, nanostructure morphology is another import factor that can drastically impact the performance of photocatalysis. In previous chapter of this dissertation, based on the 3D CNF-templated TiO_2 nanostructures and taking the advantage of the excellent hydrophilic property of CNFs, a novel high-performance capillary PEC photoanode was developed that could perform PEC water oxidation in air with enhanced reaction kinetics.[170] However, in this PEC system, H_2 production was still in electrolyte on the surface of the counter electrode. To fully utilize the advantage of the capillary system, both reduction and oxidation (redox) reactions should be implemented in the capillary fashion. This requires the development of a full photocatalytic redox system with the 3D mesoporous hydrophilic configuration. Noting that the repeating units with reactive groups on cellulose are readily functionalized,[171] it is hypothesized that reductive ligands could be created on cellulose surfaces and used to produce Pt on-site. In this chapter, CNFs were functionalized with aldehyde groups, which were successfully used to reduce Pt ion and form Pt NPs. High density Pt NPs were created on CNF networks. ALD of TiO_2 completely converted the CNF templated into anatase TiO_2 fibers without affecting the Pt NP loading. This 3D fibrous Pt-TiO_2network structure was used as the photocatalyst in a capillary water splitting system and substantially higher H_2 generation rate was achieved compared to conventional in-electrolyte setup. This research demonstrated a new solution to efficient production of H_2 fuel from solar energy.

5.2. Experimental Section

Synthesis of Pt NP-decorated CNFs: The main material used in this project is CNF isolated through a combination of TEMPO treatment and homogenization processing. CNF hydrogel was oxidized in 0.05M $NaIO_4$ solution to generate aldehyde functional groups. The dialdehyde-functionalized CNF hydrogel were then immersed in 0.01M Chloroplatinic acid (H_2PtCl_6) solution at 80 ℃ for 13 hours. The on-site reduction of Pt ions yielded high density Pt NPs on CNF surfaces. After gently rinsing the obtained Pt NP decorated CNF hydrogel in deionized (DI) water for several times, the hydrogel was then frozen by liquid nitrogen in an ethanol bath. Next, the frozen hydrogel was immediately and quickly transferred into the vacuum chamber of a Labconco 4.5 Liter Free Zone Freeze Dry System (Labconco, MO, USA) at a stable pressure of ~35 mTorr for 12 hours at room temperature, where sublimation of the ice yielded a nanofibrous structure cellulose film with Pt NPs on the surface. In order to obtain different Pt NP loading, three processing times, 144, 180, and 200 hours, were selected to oxidize the CNF hydrogel, which were then used to produce Pt NPs within the same time frame and marked as C1, C2, and C3, respectively.

ALD of TiO_2 conversion: The Pt-CNFs template was loaded into the ALD reaction chamber for 20-cycle TiO_2 overcoating at 150 ℃ and subsequent 150-cycle TiO_2 growth at 300 ℃, which yield the thickness of polycrystalline TiO_2 as ~17 nm. The ALD growth cycle consisted of 0.5 s H_2O pulsing + 60 s N_2 purging +0.5 s titanium tetrachloride ($TiCl_4$) pulsing + 60 s N_2 purging. The 150 ℃ ALD deposition process

introduced a thin TiO_2 layer (~2 nm) to replicate the fibrous structure of Pt-CNFs, and the following high temperature ALD process at 300 ℃ made a continues coverage of anatase TiO_2 as well as completely removed the CNFs leaving the fibrous nanotubular TiO_2 with preserved Pt nanoparticles on their surface.

Sample characterization: The morphologies of as-prepared Pt-CNFs template and Pt-TiO_2 photocatalyst were characterized by LEO 1530 GEMINI scanning electron microscopy (Zeiss, Germany). XPS measurements were conducted for the elemental analysis on a Thermo Scientific K-alpha XPS system with Al Kα source. Tecnai TF-30 transmission electron microscopy (FEI, OR, USA) and X-ray diffraction (Bruker D8, Bruker, MA, USA) was implemented to study the crystal structure of the Pt NPs formed on CNF surface and corresponding Pt-TiO_2 heterostructures. To quantify the final Pt loading as a function of the CNFs oxidation time, ICP spectrometry (Optima 2000 ICP-AES, PerkinElmer, MA, USA) and EDS were performed on three Pt-TiO_2 samples (T1, T2 and T3). In the ICP measurement, certain amount of each Pt-TiO_2 sample was weighted and put into a beaker with subsequent 15 mL aqua regia solution (HCl:HNO_3=3:1) added in. The beaker was then heated to 70 ℃ and vigorously stirred for 3 hours to dissolve all Pt in the sample. The solution was thereafter filtered and the DI water was added in the filtrate to fix the volume at 112 mL. Besides, the ICP Pt standard solution (1000 mgL^{-1}, Sigma-Aldrich, MO, USA) was diluted for reference solutions in three different concentrations (0.1 mgL^{-1}, 1.0 mgL^{-1}, and 10.0 mgL^{-1}). Finally, these three reference solutions and the filtrated solution of each Pt-TiO_2 sample were injected into

the ICP system to characterize the Pt concentrations. The SBET of the Pt-TiO_2 photocatalyst was analyzed by nitrogen adsorption using a Quantachrome Autosorb-1 equipment (Quantachrome Instruments, FL, USA). Prior to nitrogen adsorption measurements, each sample was transferred into a glass tube and degassed at 120 ℃ for 12 hours.

Set up for hydrogen production via photocatalytic reaction: For capillary photocatalysis setup, the as-synthesized fibrous Pt-TiO_2 network structure was integrated with an untreated CNFs stripe by following procedures: First, the CNFs block was carved into a chair-like shape. Next, 0.0157 g Pt-TiO_2 photocatalyst was settled on this CNFs "chair" and fixed by the large mesh cheesecloth. The integrated CNF-based photocatalysis system was then hung in the quartz flask, and thereafter the whole apparatus was well sealed with one port opened in the water for further H_2 collection. The other port of the flask was connected to the upper flask through a glass valve, where appropriate amount of pure DI water and sacrificial reactant methanol were filled (H_2O:CH_3OH=4:1 in volume) (Figure 5.1a). Before the illumination, Ar gas with a flow rate of 70 sccm was introduced into the methanol solution for deaeration and system purging for one hour. Then the glass valve in the upper flask (red circle in top left picture of Figure 5.1b) was opened to allow the suitable amount of methanol aqueous solution flow into the bottom quartz flask, where the bottom portion of the CNF block was in touch with the electrolyte while the Pt-TiO_2 photoactive portion was exposed in the space. Light illumination was provided by a 150W Xenon arc lamp (Newport Corporation,

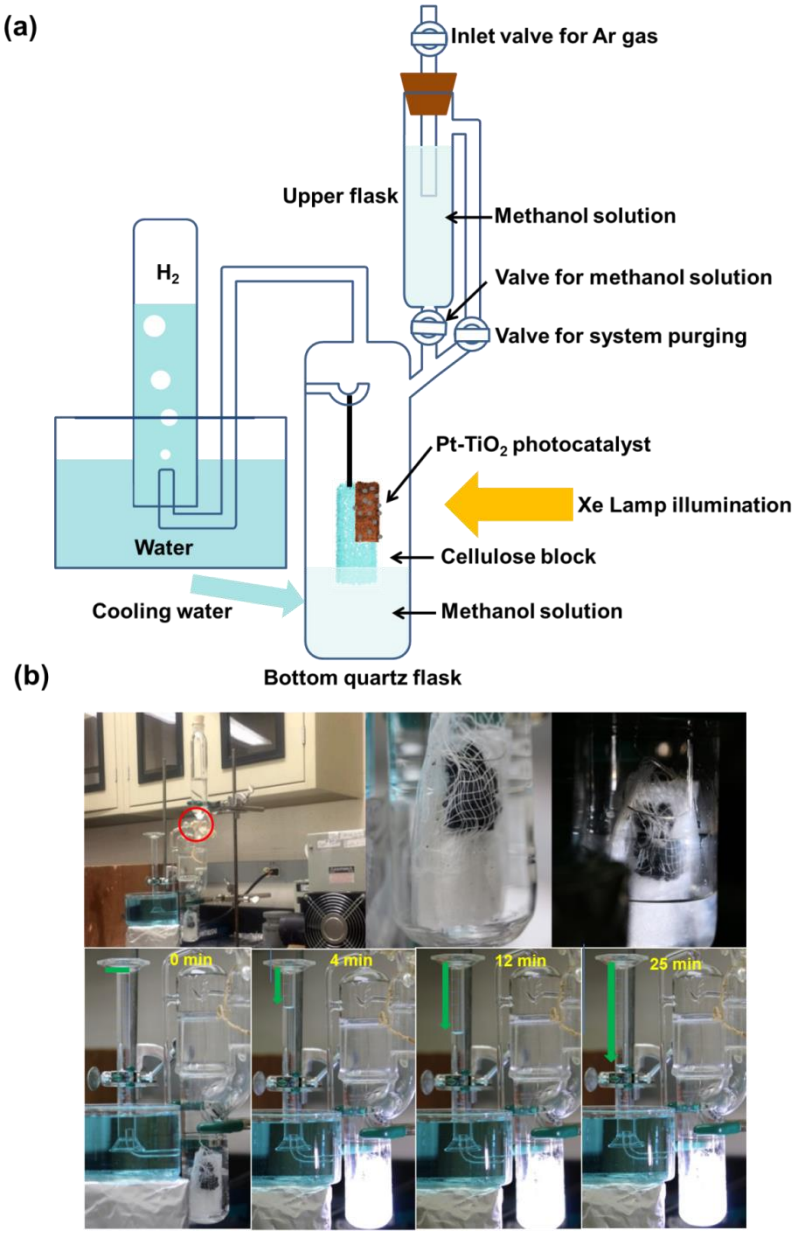

Figure 5.1. A schematics (a) and pictures (b) of typical apparatus configuration forH_2production and collection when the whole Pt-TiO_2 composite-CNF was exposed under Xe lamp illumination. H_2 is evolved and collected as indicated by the green arrows.

Irvine, CA), and the intensity at the Pt-TiO_2 photocatalyst position was adjusted to be 70 mW cm^{-2} to restrict the system temperature raising from the light irradiation. The backside of the flask was flashed by cool water during the photoreaction process. The evolved gas was collected in the graduated flask and the H_2 amount was characterized by a Spectra Products Residual Gas Analysis (RGA) mass spectrometry system (MKS Instruments, Wilmington, MA, USA). In order to determine the amount of H_2 (mL), the standard H2 (Industrial Grade, Airgas, PA, USA) in certain volumes were also utilized for calibration. The peak areas of the signal were calculated at the constant total pressure of 2.53×10^{-5} Torr (Figure 5.2). By comparing the signal peak areas to the calibration data, the volume of the H_2 in the collected gas sample can be obtained. Several molar mass channels were simultaneously used to detect the possible components of the collected gas sample (Figure 5.3 and Table 5.1).

5.3 Results and Discussion

The CNF hydrogel was employed as the starting material to produce high-density Pt nanoparticle-decorated TiO_2 nanofiber network (Figure 5.4). The CNFs hydrogel was first immersed into the NaIO4 solution for aldehyde functionalization. Under desired conditions (see details in experiment section), the two OH groups on the repeating unit of cellulose were oxidized to aldehyde groups. Second, the on-site reduction of Pt ions by aldehyde groups yielded high density Pt NPs on CNF surfaces when the dialdehyde-functionalized CNFs hydrogel was placed in chloroplatinic acid (H_2PtCl_6) solution. At last, the obtained Pt NP-decorated CNFs hydrogel was frozen dried to form a

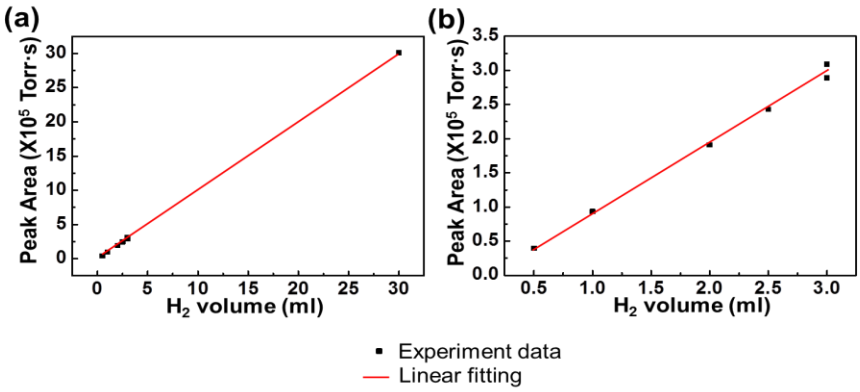

Figure 5.2. (a) The calibration curve of the Residue Gas Analyzer to determine the amount of H_2 by using standard H_2 in certain volumes (0.5, 1, 2, 2.5, 3, and 30 mL). (b) Zoom in view of the calibration curve using the standard H_2 ranging from 0.5 mL to 3 mL.

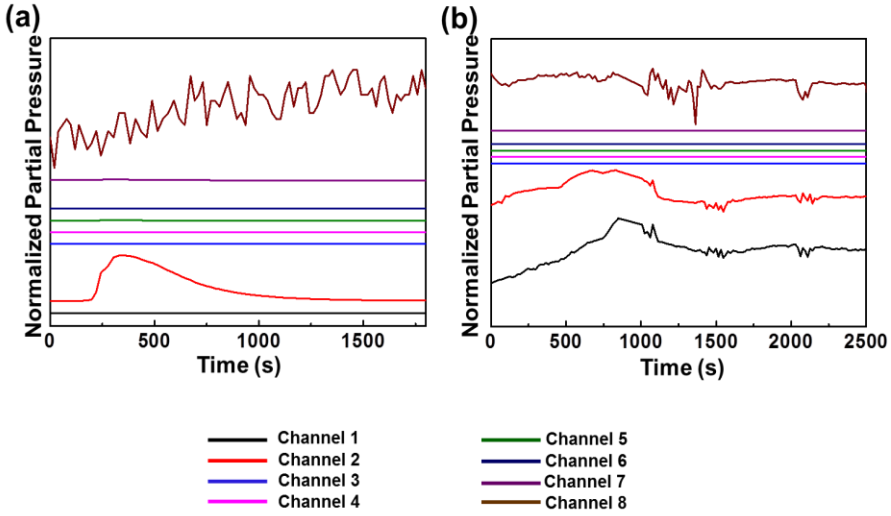

Figure 5.3. Normalized partial pressure of each setting channel versus measurement time by Residue Gas Analyzer. Every channel was set to detect the gas molecule with certain mass. (a) Result of the 30 mL H_2 sample, which is for calibration. (b) Result of the experiment gas sample, which was obtained from the 3 min capillary photocatalytic reaction at the beginning of sample T1. Since Ar may be contained in the gas sample as well as it was used as carrier gas during the RGA measuremnt, the obvious curve variation of channel 8 for Ar can be observed.

Table 5.1. Residue Gas Analyzer Maesurement Channel List

No. of Channel	1	2	3	4	5	6	7	8
Detected Mass	1	2	3	16	18	28	32	40
Related ion/Molecule	H^+	H_2	H_3^+	O^-	H_2O	Air	O_2	Ar

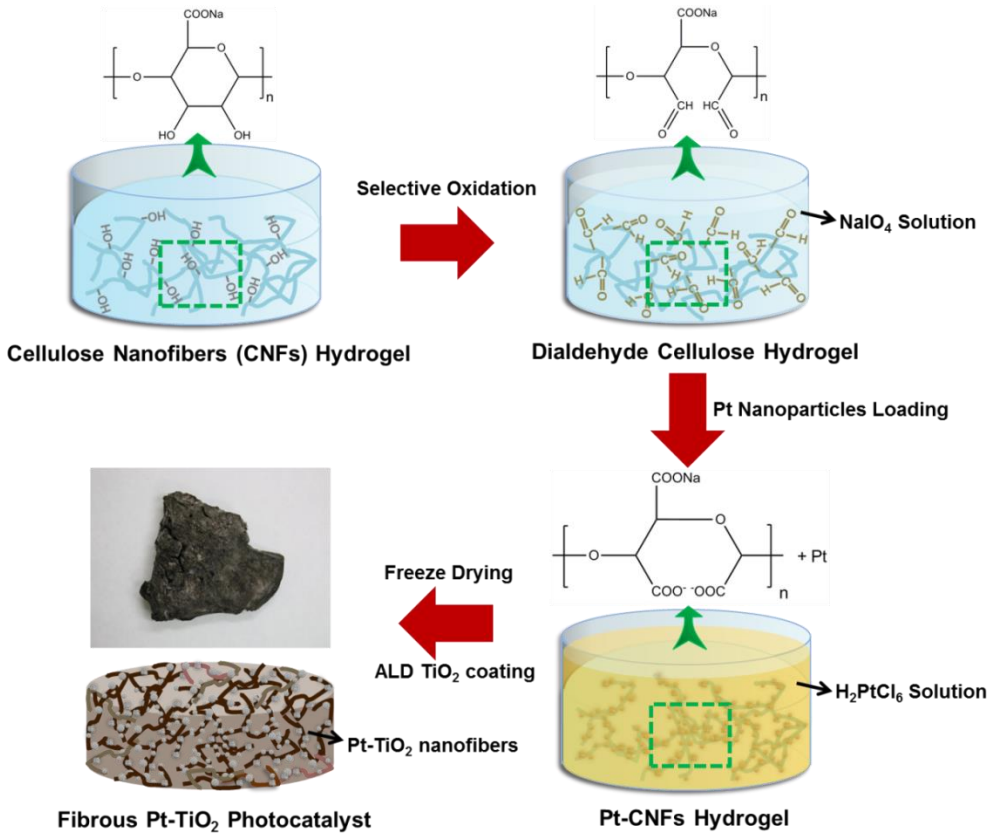

Figure 5.4. Schematic representation of the preparation processes. Cellulose nanofibers (CNFs) hydrogel is placed into $NaIO_4$ solution, which leads to the oxidation of hydroxyls to obtain dialdehyde cellulose hydrogel. The hydrogel is thereafter transferred into H_2PtCl_6 solution for the growth of Pt nanoparticles. The cellulose hydrogel with Pt nanoparticles on the surface is finally treated by freeze-dry method and sequential ALD TiO_2 thin film overcoating to achieve the nanofibrous Pt-TiO_2photocatalyst.

mesoporous structure. Subsequent ALD of TiO_2 converted CNFs to tubular TiO_2 nanofibers with Pt NPs exposed on the surfaces.

Theas-prepared high-density Pt NP-decorated CNF network (Pt-CNF) was first observed by SEM. As shown in Figure 5.5a, Pt NPs appeared in clusters of several (~2-6) individuals agglomerated together, which were evenly distributed over the entire CNF network. Meanwhile, the high-porosity network structure of CNF was nearly unchanged after the long-time on-site Pt ion reduction reaction and the average fiber diameter remained at ~ 15 nm (inset of Figure 5.5a). Individual Pt NPs exhibited a relatively large size distribution ranging from 20 nm to 80 nm (inset of Figure 5.5a). Since the Pt NPs were produced by the aldehyde groups, changing the selective oxidation time would introduce different amount of aldehyde groups to CNF surfaces and subsequently control the loading of Pt NPs. Three processing times, 144, 180, and 200 hours, were selected to oxidize the CNF templates, which were then used to produce Pt NP within the same time frame and marked as C1, C2, and C3, respectively. CNF templates with longer oxidation time yielded smaller Pt NPs, where the average NP sizes of C1, C2, and C3 were 80 ± 30, 40 ± 25, and 30 ± 10 nm, respectively (Figure 5.6a-c). The size reduction could be attributed to the increased number of surface functionalized aldehyde groups under longer oxidation time, which induced higher Pt nucleation rate in the beginning.[172,173]

The Pt NP-decorated CNF networks were then subjected to 300 ℃ ALD coating of polycrystalline TiO_2 thin film (Figure 5.5b and Figure 5.6d-f). While the highly porous CNF network structure was well preserved after ALD coating, Pt NP agglomerates were

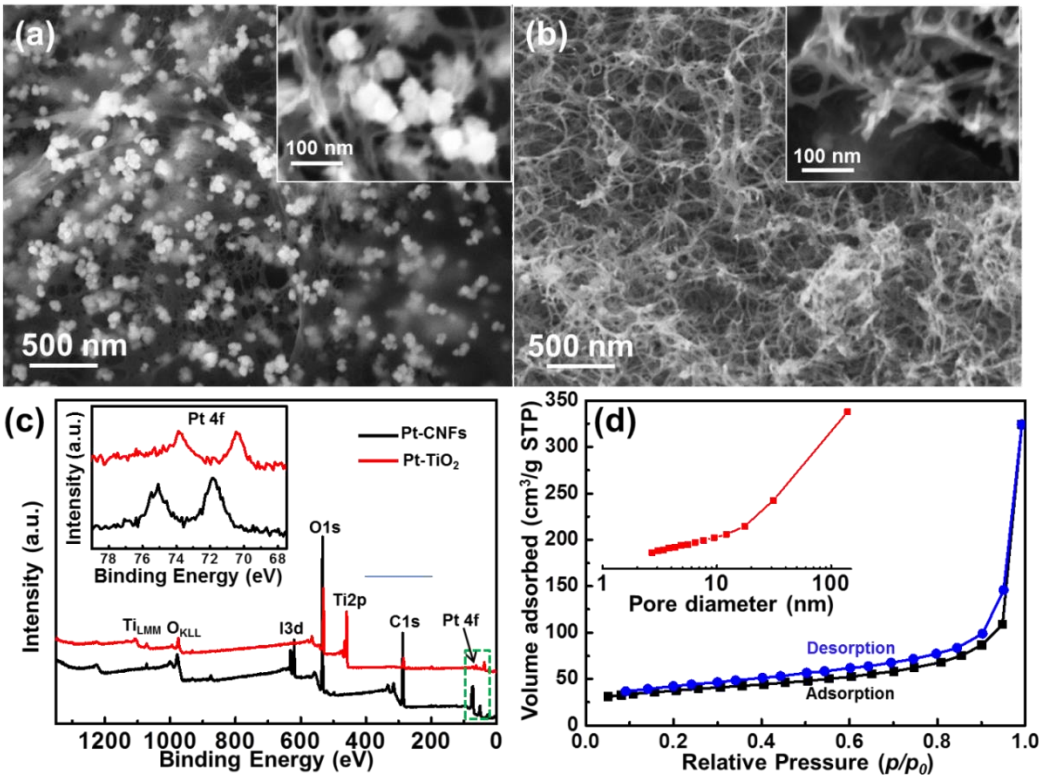

Figure 5.5. Morphology and structure of Pt-CNFs and Pt-TiO_2 samples. (a) Low magnification SEM images of nanofibrous Pt-CNFs; inset shows the as-prepared free standing Pt-CNFs in larger scale and the agglomeration of ~40 nm nanospheres on the nanostructured cellulose fibers. (b) Obtained fibrous Pt-TiO_2 network after ALD TiO_2 thin film overcoating at 300˚C; inset reveals the Pt nanospheres on fibrous TiO_2. (c) X-ray photoelectron spectroscopy (XPS) investigation for both Pt-CNFs and Pt-TiO_2 samples (black and red); inset is the spectra of Pt 4f region near ~71 eV. (d) Nitrogen adsorption desorption isotherms and the corresponding pore-size distribution curves (inset) for the 3D fibrous Pt-TiO_2 composite.

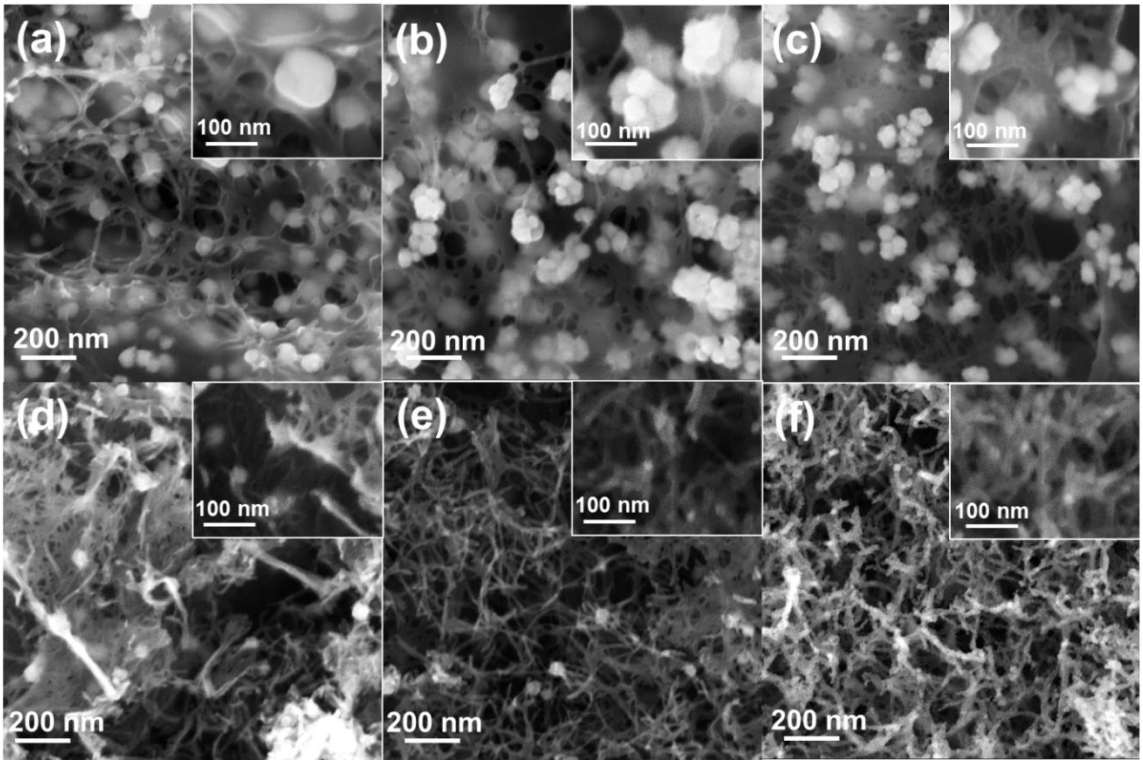

Figure 5.6. SEM images for the morphology comparison of three as-prepared Pt-CNFs templates and corresponding 3D fibrous Pt-TiO_2 composite samples.

fused together into bigger individual particles with an average size of 90±60 nm (inset of Figure 5.5b). Such a fusion phenomenon is common for metal NPs at elevated temperature due to the high surface energy and reduced melting point for small sized NPs. The high-temperature ALD process also removed the CNF template and left a pure TiO_2 tubular fiber network. [170]

Elemental analysis of Pt decoration and TiO_2 ALD deposition were then conducted by XPS.As shown in Figure 5.5c, the black and red curves illustrate the XPS profiles of Pt NP-decorated CNFs (Pt-CNFs) and structures after TiO_2 ALD coating (Pt-TiO_2). The peaks C 1s at 285.1 eV and I 3d at 619.9 eV in the Pt-CNFs spectrum are corresponding to the carbon component and residual iodine of sodium periodate ($NaIO_4$)-treated cellulose. Drastically diminished C 1s peak and disappearing of I 3d peak in the Pt-TiO_2 samplesuggested the complete removal of CNF templates. This result was consistent with previous reports that calcination above 300 ℃ could completely decompose cellulose.[142,170,174] In addition, strong Ti related peaks (Ti 2p and Ti_{LMM}) appeared from the Pt-TiO_2 sample, supporting the fibrous structure after ALD coating was completely converted into Ti-based materials. Pt 4f region near ~71 eV was further examined in details to analyze the chemical structure of the Pt NPs before and after ALD processing (inset of Figure 5.5c and Figure 5.7a). The Pt $4f_{7/2}$ and Pt $4f_{5/2}$ in Pt-CNFs are located at 71.8 eV and 75.2 eV, respectively. These two peaks shifted to 70.5eV and 73.8 eV, respectively after ALD of TiO_2 conversion. The higher 4f electron binding energy in Pt-CNF structure can be attributed to the extra Pt-O bonds between Pt NPs and the

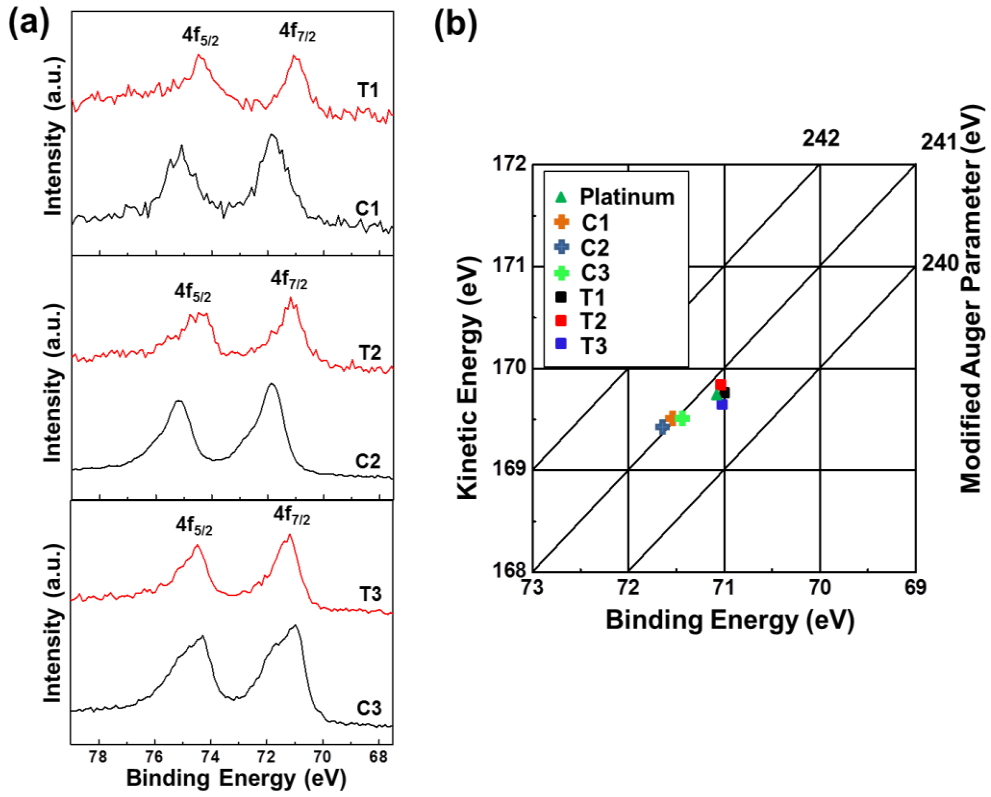

Figure 5.7. (a) Pt 4f XPS spectra for all three Pt-CNFs samples and their corresponding Pt-TiO_2samples. (b) Wagner plot showing the modified auger parameters of Pt in all Pt-CNFs and their corresponding Pt-TiO_2 samples. The Pt chemical states in Pt-TiO_2composites lie almost at the same position of metallic Pt (green triangle).

carboxyl groups on CNFs.[175,176] The doublet lines in the Pt 4f spectrum in Pt-TiO_2 (70.5eV and 73.8 eV) perfectly match the positions of metallic Pt.[177] The 3.3 eV difference between the binding energies of Pt $4f_{7/2}$and Pt $4f_{5/2}$ peaks also indicates the presence of metallic Pt4f states.[178] Moreover, compared to the Pt-CNF samples (C1, C2, and C3), the modified Auger parameters of Pt in corresponding Pt-TiO_2 samples all shifted to the same position of metallic Pt[179,180] (green triangle) in the Wagner plot (Figure 5.7b). Therefore, the relative high temperature during ALD TiO_2 would be beneficial to the formation of pure metallic Pt, which is desired for photocatalytic water splitting.[164]

One intriguing advantage of the fibrous Pt-TiO_2 network structure is that it can potentially provide very high surface area. Therefore, Brunauer-Emmett-Teller (BET) surface area (S_{BET}) analysis was conducted to investigate this potential merit. Figure 5.4d shows nitrogen adsorption-desorption isotherms and associated Barret-Joyner-Halender (BJH) desorption pore size distributions curve (inset of Figure 5.5d) measured from the fibrous Pt-TiO_2 sample. Linear increase of the adsorption isotherm profile was observed in the relative pressure (p/p_0) range from 0.05 to 0.25, where the data were used to determine the S_{BET} of the Pt-TiO_2 sampleusingthe multipoint BET method.[181] The obtained BET surface area was in the range of 128-166 m^2g^{-1} (Table 5.3), which are much larger than the typical surface area of Pt-TiO_2 NP (~50 m^2g^{-1}) or nanowire (~30 m^2g^{-1}) arrays.[163,182,183] The hysteresis loop profile appeared above the relative pressure (p/p_0) of 0.3 in the isotherm was classified as type IV according to the International Union of Pure

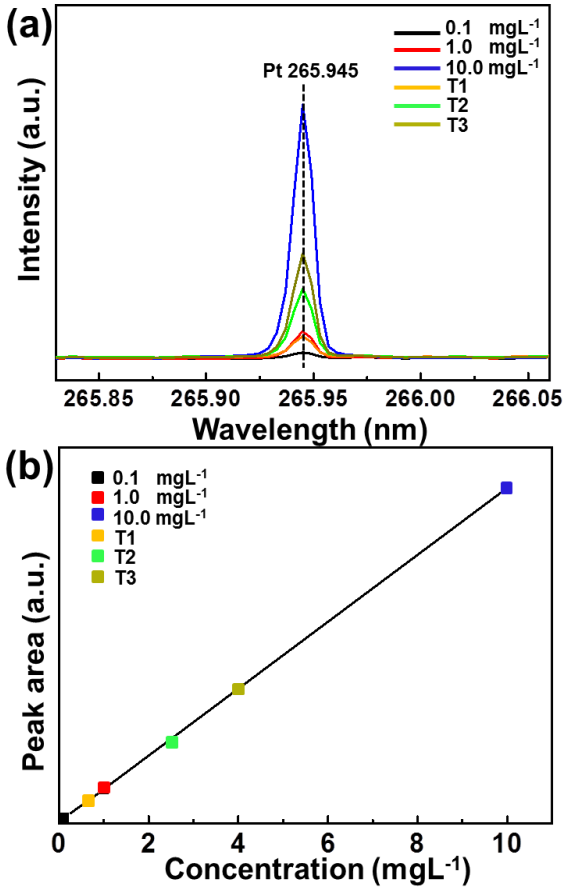

Figure 5.8. Inductively-coupled-plasma (ICP) spectrometry for three 3D nanofibrous Pt-TiO_2 samples prepared under different oxidation durations. (a) The Pt emission peaks of the three samples at 265.945 nm show clearly intensity variation compared to other three reference samples (0.1 mgL^{-1}, 1 mgL^{-1}, and 10 mgL^{-1}). (b) Corresponding emission peak areas versus Pt concentrations for three samples.

and Applied Chemistry (IUPAC) categorization,[184] indicating the presence of mesopores. The rapidly increased adsorption at relative pressure close to unity (p/p_0=1.0) was similar to the isotherm of type II, revealing the coexistence of macropores.[184] In addition, desorption curve data were used to determine the pore size distribution by the BJH method, assuming a cylindrical pore model.[164,184] The pore size distribution (inset of Figure 5.5d) shows that the fibrous Pt-TiO_2network possessed a wide pore size distribution ranging from 3 to 140 nm, *i.e.* the co-existence of both mesopores and macropores. Such a porous structure would be extraordinarily beneficial in photocatalysis, because it not only provided efficient mass pathways, but also offered extremely large reaction interface between catalyst and electrolyte.

Inductively-coupled-plasma (ICP) spectrometry and energy-dispersive X-ray spectroscopy were performed on the three Pt-TiO_2 samples (T1, T2 and T3) to quantify the final Pt loading as a function of the oxidation time. The Pt emission peaks of three samples at 265.945 nm showed intensity variations clearly (Figure 5.8a). By referencing to standard Pt solution, the Pt weight ratios of the T1, T2 and T3 samples were 2.3%, 7.72%, and 11.05%, respectively (Figure 5.8b and Table 5.2). Similar concentration values were also obtained by EDS (Figure 5.9). This result suggests that increasing the amount of aldehyde group on CNFs could effectively raise the Pt NP loading to a substantially high level.

TEM and XRD were implemented to study the crystal structure of the Pt NPs formed on CNF surface and corresponding Pt-TiO_2 heterostructures. Low magnification TEM

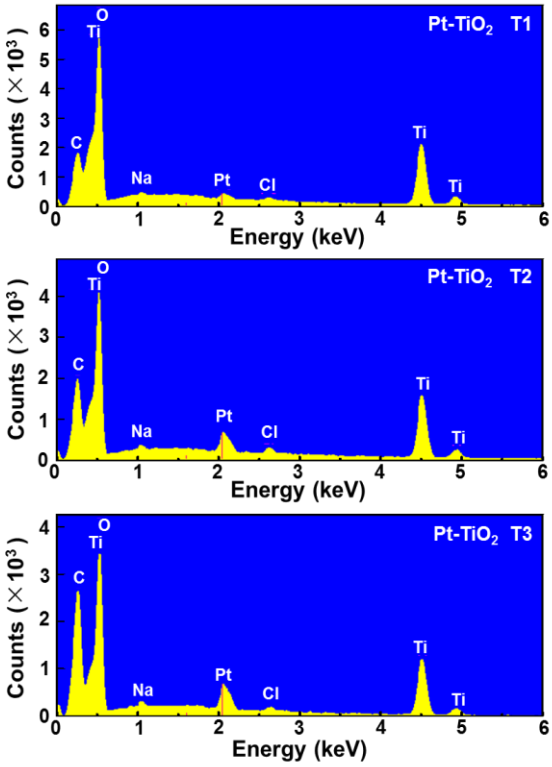

Figure 5.9. Energy-dispersive X-ray spectroscopy (EDS) for all three 3D Pt-TiO_2composites (T1, T2, and T3).

Table 5.2. Pt weight ratios in three 3D Pt-TiO_2 composites from both IPC and EDS characterizations.

Sample	ICP result (mgL^{-1})	Volume of solution (mL)	Pt amount (mg)	Sample amount (mg)	Pt wt %	EDS wt %
T1	0.720	112	0.081	3.5	2.30	2.61
T2	2.619	112	0.293	3.8	7.72	8.51
T3	4.046	112	0.453	4.1	11.05	11.38

image clearly shows the network structure of CNFs with a fairly uniform thickness of ~15 nm, an average pore size of ~140 nm, and decorated with Pt NPs (Figure 5.10a). Corresponding selective area electron diffraction (SAED) pattern (inset of Figure 5.10a) exhibits the representative bright diffusive halo of cellulose[185] and diffraction spots of crystalline Pt. The crystalline structure of Pt NPs was further confirmed by XRD spectra, where the cellulose diffraction peak at 23 ° and there presentative Pt (111) and (220) peaks were identified (Figure 5.11). An individual Pt NP rooted on the CNF surface is shown in Figure 5.10b. The NP was ~80 nm in diameter and exhibited a spherical outline from the un-supported region. The relatively large contact area between the NP and CNF would be a result of the on-site reduction of Pt ions by the surface aldehyde groups. The spherical shape of the NP is an indirect evidence of the nano-crystallinity of the Pt NP because no specific crystal facets could be observed from the NP. HRTEM image (Figure 5.10c) also revealed that the Pt NP was composed of numerous tiny crystallites. This observation suggested that the CNF surface aldehyde groups might produce trace amount of Pt over the entire surface, which migrated and agglomerated into spherical Pt NPs in liquid media to minimize their surface energy.[186,187] TEM image in Figure 5.9d clearly shows the well-preserved fibrous structure after 170-cycle ALD TiO_2 deposition at 300 ℃, where more concentrated Pt NPs can also be observed. SAED pattern further confirmed the anatase phase TiO_2 and crystalline Pt (inset of Figure 5.10d). The thickness of the polycrystalline TiO_2 film was found to be ~17 nm (Figure 5.10e), which was consistent with the typical morphology and growth rate of ALD TiO_2. Pt NPs were

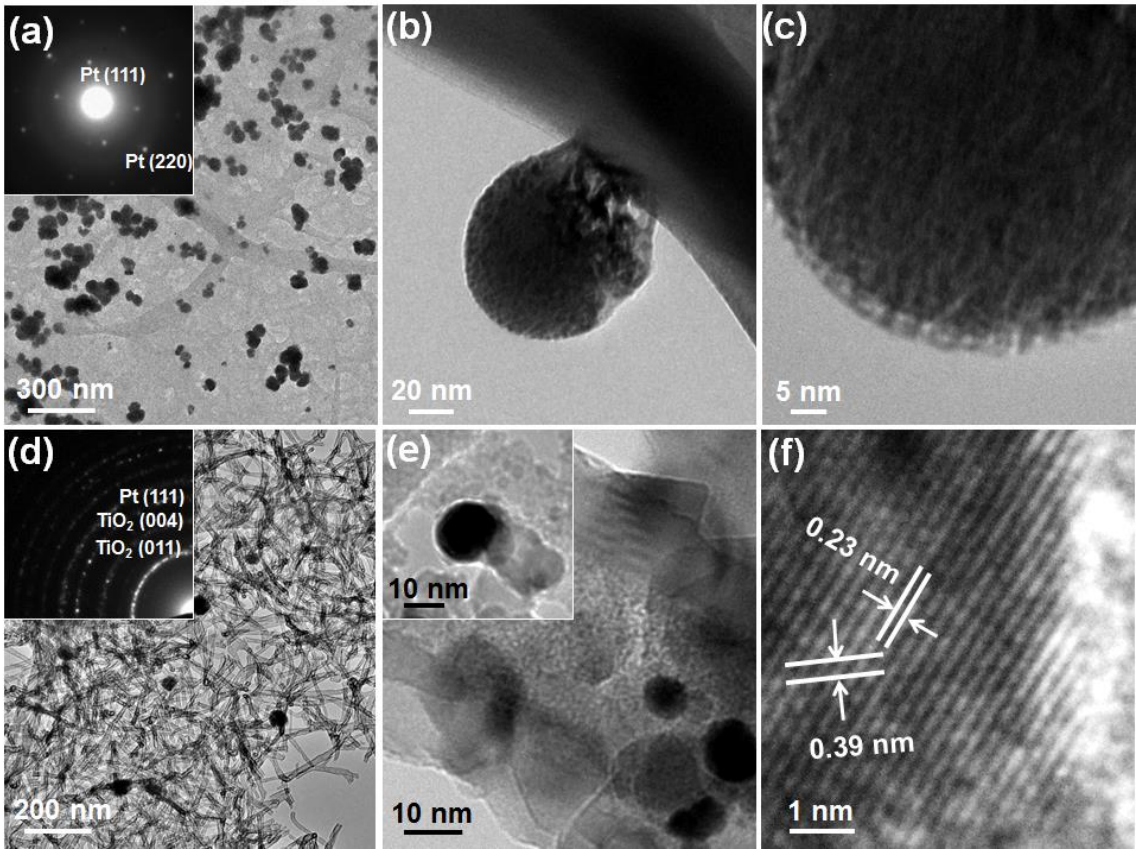

Figure 5.10. Structures and Pt nanoparticles distribution of samples before and after ALD TiO_2 coating. (a) TEM image of Pt-CNFs revealing fibrous structure with Pt spheres on it; inset is the respective SAD pattern. Only crystalline Pt appears on the Pt-CNFs before ALD TiO_2 coating. (b,c) Higher magnification images showing Pt nanospheres "root" on the surface of CNF (b) and the Pt nanospheres aggregated from small nanoparticle (c). (d-f) TEM images of Pt-TiO_2 after ALD TiO_2 coating. (d,e) The fibrous TiO_2 with Pt nanoparticles indicating the well preserved morphology after ALD process. (e) The ~17 nm thick polycrystalline TiO_2 is selectively deposited between Pt nanoparticles. (f) The measured lattice spaces of the nanoparticle are 0.39 and 0.23 nm, representing the corresponding values of Pt (100) and (111) planes.

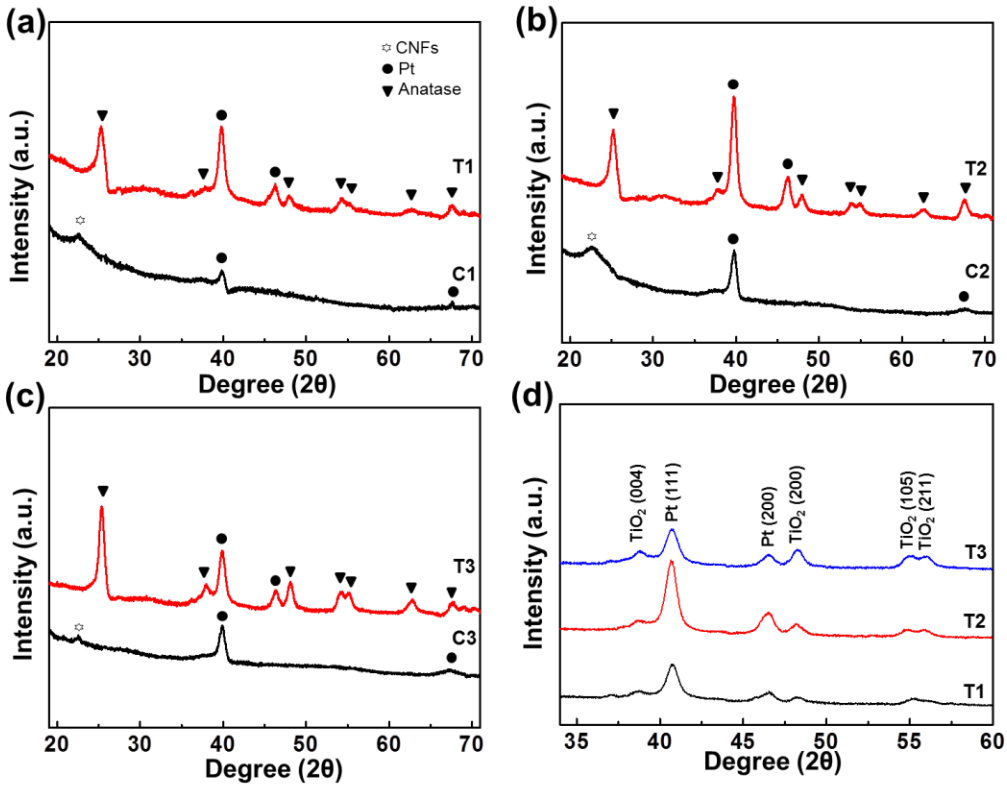

Figure 5.11. XRD carried on all three as-prepared Pt-CNFs templates (C1, C2, and C3) and 3D Pt-TiO_2composites (T1, T2, and T3). (a-c) The cellulose diffraction peak at 23 °can be only observed on Pt-CNFs templates. (d) The Pt diffraction peaks and anatase TiO_2 peaks are obtained on all Pt-TiO_2samples.

partially embedded in the TiO_2 film and the top portion was not covered by TiO_2 (inset of Figure 5.10e). Exposure of the Pt NP was because $TiCl_4$ precursors would preferentially attach to the hydrophilic CNFs surface that possesses abundant hydroxyl sites rather than the inert Pt surface.[188,189] Meanwhile, the high temperature ALD process heat-treated the Pt NP simultaneously. This process was very helpful for improving the crystallinity of Pt NPs, removing chemical residues, and forming close contacts with TiO_2 crystals. Long-range-ordered Pt lattices now can be clearly observed from HRTEM. The lattice spacing of the Pt NP was measured to be 0.39 and 0.23 nm, corresponding to Pt (100) and (111) planes respectively. The anatase TiO_2 and crystalline Pt phases were also verified by the XRD spectra on all three Pt-TiO_2 samples (Figure 5.11d).

To fully demonstrate the advantage of cellulose templating, the out-of-electrolyte capillary design[170] was used to test the photocatalytic water splitting behavior of the Pt NP decorated TiO_2 nanofiber network. The schematic setup is shown in Figure 5.12a.The fibrous Pt-TiO_2 structure was attached to a piece of untreated CNFs network. The bottom part of the CNF block was placed in a methanol solution to draw and transport the electrolyte to the Pt-TiO_2 photoactive surfaces. The testing apparatus for measuring volumes of photocatalyzed gas evolution is shown in Figure 5.1 (see experimental section for detailed measurement procedures). Upon illumination by a 70 W cm^{-2} Xe lamp source, H_2 rapidly evolved in air from the Pt-TiO_2 porous structure (no bubbles were formed in the electrolyte) and was collected in a quartz flask (Figure 5.1). In this capillary photocatalytic water splitting process, the electrolyte was continuously supplied

through the CNF network taking the advantage of its excellent hydrophilic property and filled the mesopores within the Pt-TiO_2 network. When photoexcited electron-hole pairs were generated, they quickly dissociated at the Pt-TiO_2 interface with the electrons moving to the Pt NPs to reduce water generating H_2; and holes moving to the TiO_2 nanofibers to oxidize the electrolyte. Similar to capillary PEC, enhanced photocatalytic reaction kinetics could be expected from the dynamic electrolyte supply and infinitesimal active electrolyte volume.[170]

The amount of H_2 generation was quantified for both capillary and conventional in-electrolyte setups using Residue Gas Analyzer (RGA) (see details in experiment section). Under the illumination of 70 W cm^{-2} Xe lamp source, the capillary setup of one gram Pt-TiO_2 photocatalyst (Sample T1) exhibited significantly higher H_2 yields compared to the in-electrolyte setup; while the H_2 production from both setups monotonically increased as a function of time (Figure 5.12b). Initially, 4.6 mL H_2 was produced after 10 minutes illumination from the capillary setup (black curve), which was three times higher than that from the in-electrolyte setup (red curve). With elongated reaction time, the H_2 generation rates decreased gradually and demonstrated a tendency of saturation after ~100 minutes of continuous reaction. The attenuation in H_2production was more significant in the capillary setup, and thus the ratio between the yields of the two setups was reduced from ~3.07 (at 10 minutes) to ~1.68 (at 80 minutes). Similar remarkable photocatalytic performance gain by the capillary setup, as well as the H_2

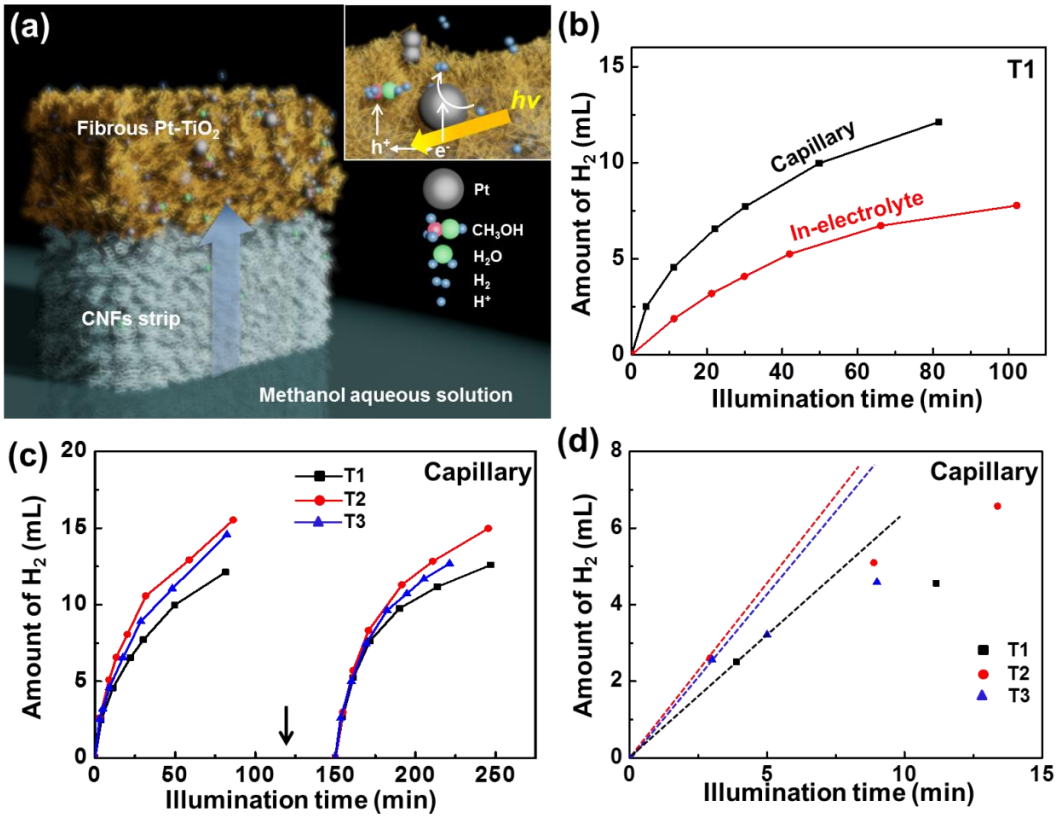

Figure 5.12. (a) Schematics of the novel capillary design by using CNFs block for photocatalytic H_2 evolution. (b) H_2 yield of 3D nanofibrous Pt-TiO_2 sample T1 from both capillary design (black) and in-electrolyte design (red). (c) H_2 yield of three Pt-TiO_2photocatalyst samples (T1, T2, and T3) versus illumination time in capillary design. The curve after the electrolyte renewal and whole system purging indicates a good stability of the capillary setup for photocatalytic reaction. (d) Magnified H_2 evolution curves of the first 15 min in the presence of T1, T2 and T3 photocatalyst. Derived initial H_2 production rates were calculated by the indicated dashed lines.

production attenuation phenomenon were both observed from Pt-TiO_2 Samples T2 and T3 that had higher Pt loading (Figure 5.13a and b).

To further investigate the reason of H_2 production attenuation, the reaction system was reset after 120 minutes photocatalytic reaction. The resetting process included blocking off illumination, replacing methanol solution, and 30-minute system purging with argon (Ar) gas. After the system resetting, the initial H_2 generation recovered to its original rate for all three Pt-TiO_2 samples (T1, T2, and T3). The same attenuation phenomenon was also observed from longer time photocatalytic reaction time (Figure 5.12c). These results revealed that the catalytic performance of the Pt-TiO_2 structure was not impacted by the long-term operation and the attenuation of H_2 production rate would be a result of kinetic factors. This kind of reaction rate drop was often observed in high-rate H_2 generation and other electrochemical processes,[165,168,190,191] particularly when the redox reactions occurred within very close vicinity.[192,193] Therefore, the non-linearity of H_2 yield versus time could be attributed to the reduced concentration of methanol solution and the accumulation of absorbed product molecules (e.g. CH_2O and probably trace of H_2) impeding the accessibility of reactants.

Considering the kinetic factors that majorly influenced the long-term H_2 production, the initial H_2 generation rate was analyzed to understand the intrinsic photocatalytic properties. Figure 5.12d shows the amount of H_2 collected at a few time intervals within the first 15 minutes of illumination, from which the initial H_2 generation rate was obtained from the slop of the dash line that connected the original zero and first collected

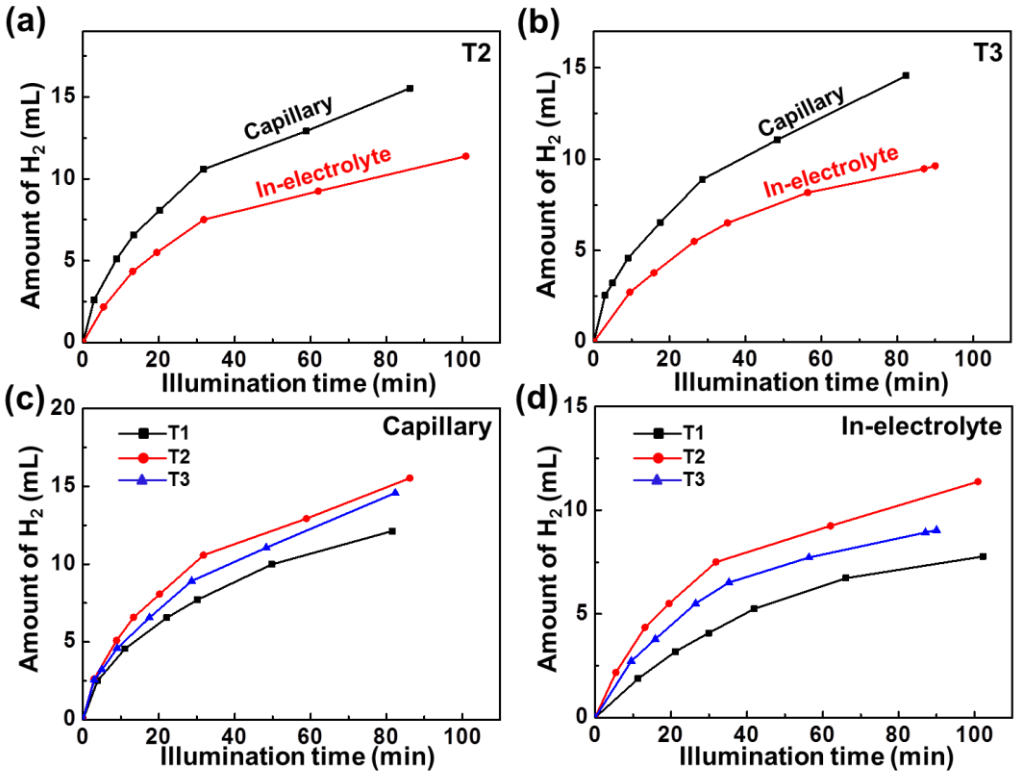

Figure 5.13. H_2 yield of Pt-TiO_2in capillary setup and in-electrolyte setup from photocatalyst (a) T2 and (b) T3. (c,d) The comparison of H_2 amount from three 3D Pt-TiO_2composites (T1, T2, and T3). In both capillary (c) and in-electrolyte setup (d), T3 photocatalyst exhibits the best ability on H_2 production.

data point.[157,165] Same process was also applied to analyze the H_2 data of the in-electrolyte setup (Figure 5.14). All the data are summarized in Table 5.3. In general, the initial H_2 generation rate of capillary setups were significantly higher than those obtained from the in-electrolyte setup owing to less electrolyte related light scattering and better local reaction kinetics that we discovered in previous study.[170] Specifically, the capillary setup exhibited an initial H_2 generation rate of 100.56 $mmolg^{-1}h^{-1}$ from the Pt-TiO_2 photocatalyst T1; whereas the in-electrolyte setup from the same photocatalyst had only 25.88 $mmolg^{-1}h^{-1}$. The improvement by capillary setup reached 287%. The highest initial H_2 generation rate (138.69 $mmolg^{-1}h^{-1}$) was found from photocatalyst T2 that had higher Pt NP loading. However, the corresponding enhancement from capillary setup was reduced to 123%. When the Pt loading further increased to 11.05% (sample T3), the initial H_2 generation rates of both setups decreased to 128.30 $mmolg^{-1}h^{-1}$, 44.82 $mmolg^{-1}h^{-1}$, respectively, where the enhancement ratio jumped back to 186%.

The parabola relation between H_2 yield and Pt wt% (Figure 5.15) is in accordance with other published studies on metal catalysts loading. [163,168,194] While the absolute H_2 yield further rose when the Pt NP loading increased, the difference between the capillary and in-electrolyte setup reduced. The less sensitive H_2 generation rate to Pt loading of the capillary setup indicates that the capillary setup is more kinetically favorable and the room of improvement is more limited compared to the conventional in-electrolyte configuration.[193]. The overall significantly higher performance of the capillary photocatalytic design (Table 5.3) clearly shows this setup can further enhance the H_2

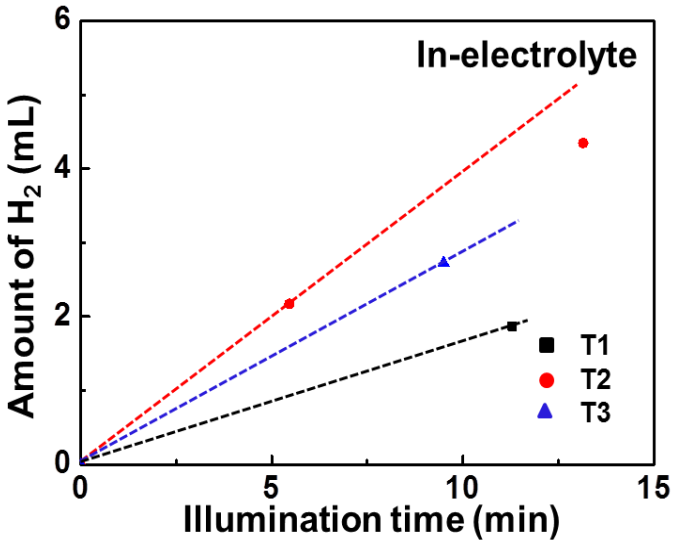

Figure 5.14. Magnified H_2 evolution curves in in-electrolyte setup of the first 15 min in the presence of T1. Derived initial H_2 production rates were calculated by the indicated dashed lines.

Table 5.3. Summary of the physical properties and photocatalytic activity of three 3D Pt-TiO_2 photocatalysts (T1, T2, and T3).

Pt-TiO_2 Sample	Average Pt Size (nm)	Pt wt %	S_{BET} (m^2g^{-1})	H_2 Production Set up	Initial H_2 Production Rate($mmolg^{-1}h^{-1}$)
T1	15	2.3	134.23	Capillary	100.56
				In electrolyte	25.88
T2	12	7.72	128.04	Capillary	138.69
				In electrolyte	62.11
T3	10	11.05	166.45	Capillary	128.30
				In electrolyte	44.82

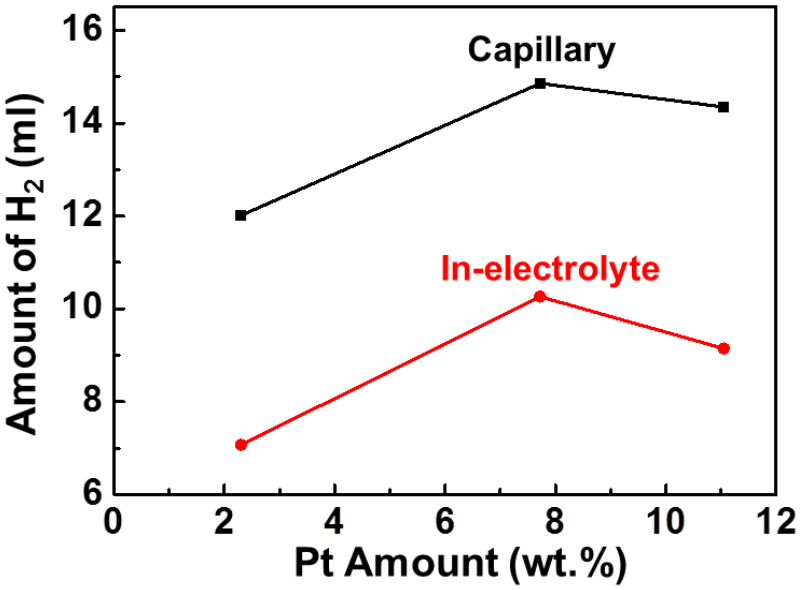

Figure 5.15. H_2 yield of both capillary and in-electrolyte measurement from three 3D Pt-TiO_2 fibrous structures (T1, T2, and T3) with different Pt contents.

evolution in addition to those achieved by other strategies, such as optimizations of Pt-TiO_2 surface area and Pt-loading amount. Given other key kinetic factors being well-engineered, the maximum H_2 evolution efficiency could be improved by implementing the capillary photocatalytic design.

5.4 Conclusion

In summary, the aldehyde-functionalization of CNFs is an effective strategy to introduce Pt NPs onto CNF surfaces by on-site Pt ion reduction. High concentration of Pt NP loading (up to 11.05 wt%) was achieved on $NaIO_4$-treated CNFs surfaces via on-site aldehyde reduction. Owing to the drastic differences in the hydrophilic behavior of the Pt and CNF surfaces, subsequent ALD of TiO_2 could be selectively deposited on CNFs and keep the Pt NP uncovered. The high temperature ALD process also simultaneously improved the crystallinity of Pt NPs and removed the CNF template leaving a pure anatase phased TiO_2 nanofiber network decorated with high-density Pt NPs. The fibrous Pt-TiO_2 network photocatalyst was integrated with CNF strips to develop the capillary setup of photocatalyzed water splitting. Owing to the excellent hydrophilic property of CNFs, capillary force quickly and continuously supplied methanol electrolyte solution to the Pt-TiO_2 catalytic sites that were placed outside of the solution. Better reaction kinetics and higher efficiency were achieved from the capillary design compared to conventional in-electrolyte reaction. The initial H_2 generation rates were found to be 100.56-138.69 $mmolg^{-1}h^{-1}$for the capillary setup based on different Pt NP loading, which was 123.3-287 % larger than conventional in-electrolyte setup (25.88-62.11 $mmolg^{-1}h^{-1}$). The

cellulose-based nanomanufacturing technique holds a great promise for large-area, low-cost, and green fabrication of functional nanomaterials. The capillary photocatalytic design mimics the mass transport process in natural photosynthesis, where the interaction between light and reaction sites is no longer limited by the volume, surface and depth of electrolyte. Therefore, this 3D nanofibrous Pt-TiO_2 photocatalyst offers a brand new solution for improving the throughput of photocatalytic hydrogen productions.

Chapter 6. Hierarchical 3D VO_x Nanorod@Si Nanowire Architecture for High Performance Supercapacitor

6.1 Introduction

As one of the most promising strategies for next generation energy storage, electrochemical supercapacitor has received considerable attention worldwide owing to its high-power density, fast charging/discharging, excellent cycling stability, and low maintenance.[52,195-197] Electrochemical double-layer capacitors (EDLCs) is one major type of supercapacitor design that stores electrical energy by accumulating ions on electrode surface resulting in the high energy density and high-rate capability.[53] Pseudocapacitor, on the other hand, makes use of fast redox reactions or phase changes at the surface or subsurface of active materials with the potential to achieve higher energy density than EDLCs.[198,199] Generally, high-capacitance electrode requires a high surface area and good electrical conductivity. These features are strongly related to the electrochemical double layer capacitance and/or electrochemical activity of electrode surfaces.[51-53] Therefore, one major strategy to improve the performance of supercapacitors is to construct complex nanostructured electrodes with hierarchical geometric structure, adequate charge transport properties, as well as suitable thickness and surface chemical properties.

3D hierarchical nanostructures have been increasingly studied in electrochemical applications due to their extremely large surface-to-volume ratio, better permeability and more surface active sites.[34,143,196,200-203] Owing to the extraordinary capability of

conformal and pinhole-free coating management, ALD was often used for directly depositing active materials on 3D nanostructured templates for supercapacitor electrode fabrication.[54] [55,56] The high quality ALD films are essential for controlling ion intercalation and diffusion into the bulk electrodes to achieve high capacity.[51,57] Meanwhile, the 3D nano-templates need to be conductive for rapid and low-loss charge transport. In order to integrate all the desired features in one coherent heterostructure, an emerging attractive concept is to directly synthesize nanostructure arrays from pseudocapacitive materials on conductive nano-templates as binder-free electrodes. The SPCVD technique developed in our lab has the unique capability of growing uniform TiO_2 nanorod (NR) branches among dense and deep Si NW arrays, offering a novel hierarchical 3D NW architecture with enhanced electrical and electrochemical properties.[34] Further understanding of the growth kinetics[71] suggested this technique could be broadly applied to other functional materials, such as VOx NR branches for supercapacitor applications. In this configuration, many advantages such as high surface area, multiple accessible electroactive sites, short ion transport pathways and superior electron collection efficiency would be simultaneously achieved to deliver high specific capacitance, sustained cycle life and rate performance. Driven by this hypothesis, in this work, pseudocapacitive VO_x NRs branches were synthesized on Si NW backbones creating a unique 3D hierarchical VO_x NRs@Si NWs structure. Superior electrochemical performance of the structure was demonstrated. In addition, the calcination atmosphere could tune the chemical compositions of VO_x NRs and manipulate their supercapacitor

performance. This development presents a new 3D nanomaterial platform for high-performance supercapacitor electrodes design.

6.2 Experiment Section

Preparation of 3D hierarchical VO_x NRs@Si NWs heterostructure. The Highly orientated 3μm long Si NWs arrays were fabricated via metal assisted chemical etching method.[34] Thereafter, VO_x NRs were grown by SPCVD on Si NWs arrays in a home-made ALD system using $VOCl_3$ and H_2O as precursors. In the SPCVD process, the as-received Si NWs arrays were placed at the center of the stainless steel ALD chamber. A constant flow of 40 sccm N_2 was applied into the chamber as the carrier gas, which provided a background pressure of 4.2 Torr. The chamber temperature was kept at 650°C. In a typical VO_x NRs growth process, $VOCl_3$ and H_2O vapor precursors were pulsed into the chamber for 1.5 s and 0.75 s respectively and separated by purging N_2 for 60s. Thus, one growth cycle included 0.75 s of H_2O pulsing + 60s of N_2 purging + 1.5 s of $VOCl_3$ pulsing + 60s of N_2 purging. After 400-cycle growth, the chamber was cooled down to room temperature naturally under N_2 flow.

To prepare for the electrochemical characterization, the as-received VO_x@Si heterostructure was loaded in the ALD chamber again for 100-cycle VO_x film overcoating. The growth conditions were 1 s of H_2O pulsing + 60s of N_2 purging + 0.5 s of $VOCl_3$ pulsing + 60s of N_2 purging at 350 °C. Some samples were then annealed in H_2 and O_2 at 500 °C for 8 hours to engineer the chemical compositions of the VO_x NRs. Using the same deposition condition, 500-cycle ALD VO_x film was also deposited on Si

NWs as a reference sample.

Structural Characterization. The morphologies of the 3D hierarchical VO_x NRs@Si NWs heterostructures were characterized by LEO 1530 GEMINI scanning electron microscopy (Zeiss, Germany). Tecnai TF-30 transmission electron microscopy (FEI, OR, USA) and X-ray diffraction (Bruker D8, Bruker, MA, USA) were implemented to study the crystal structure. XPS measurements were conducted for the elemental analysis on a Thermo Scientific K-alpha XPS system with Al Kα source.

Electrochemical Measurements. The electrochemical measurements were performed in an electrochemical cell of three-electrode systems. The VO_x NRs@Si NWs were covered by epoxy leaving an exposed active area of ~ 0.5 cm^2. The reference and counter electrodes were saturated calomel electrode (SCE) and Pt, respectively. 8 M LiCl solution (Sigma-Aldrich, 99.99%) was used as the electrolyte. All electrodes were connected to a potentiostat system (Metrohm Inc., Riverview, FL) for the electrochemical measurements. Cyclic voltammetry (CV) curves were measured in a suitable potential window based on the samples' characteristics with scanning rates ranging from 1 mVs^{-1} to 2 Vs^{-1}. The galvanostatic charge-discharge (C-D) performances of all samples were measured under the current density varied from 0.5 Ag^{-1} to 20 Ag^{-1} in their corresponding potential window. The electrochemical impedance spectroscopy (EIS) measurements were conducted by applying 10 mV alternative signal versus the open-circuit voltage in the frequency range of 100 kHz to 0. 1 Hz.

6.3 Results and Discussion

Figures 6.1a and b present a typical morphology of as-synthesized VO_x NRs@Si NWs hierarchical structure. Dense VO_x NRs branched from Si NW bundles and protruded outward radially (Figure 6.1a). Higher magnification image reveals that the dimensions of the NR branches were ~250 nm in length and ~30 nm in diameter (inset of Figure 6.1a). Similar to the SPCVD TO_2 NRs result, the VO_x NRs were uniformly distributed along the entire side surfaces of the Si NWs that were 3μm in length and only ~100−200 nm apart from each other (Figure 6.1b). The VO_x NRs exhibited a rectangular prism shape, and were all rooted on the Si surfaces (inset of Figure 6.1b). After annealing at 500˚C in H_2 and O_2 atmosphere, the morphology and hierarchical structure of VO_x NRs were well preserved (Figure c, d, respectively), suggesting the VO_x NRs had good thermal stability.

TEM was used to further study the morphology and crystal structure of the VO_x NRs. Figure 6.2a shows a TEM image of VO_x NRs rooted on Si NW surface. The surfaces of Si backbone are uniformly covered by ultrathin NRs (Figure 6.2a). Closer observation showed the rectangular shape of the NR with a flat tip surface (Figure 6.2b). Corresponding selected area diffraction (SAED) pattern (inset of figure 6.2b) confirmed single crystallinity of the vanadium pentoxide (V_2O_5) phase. From the HRTEM image as shown in Figure 6.2 c, the lattice fringes was identified with an interplanar spacing of 0.29 and 0.34 nm, which was indexed as the (301) and (110) planes of V_2O_5, respectively. Notably, some NR exhibited a sword-like tip whereas their diameter was nearly identical

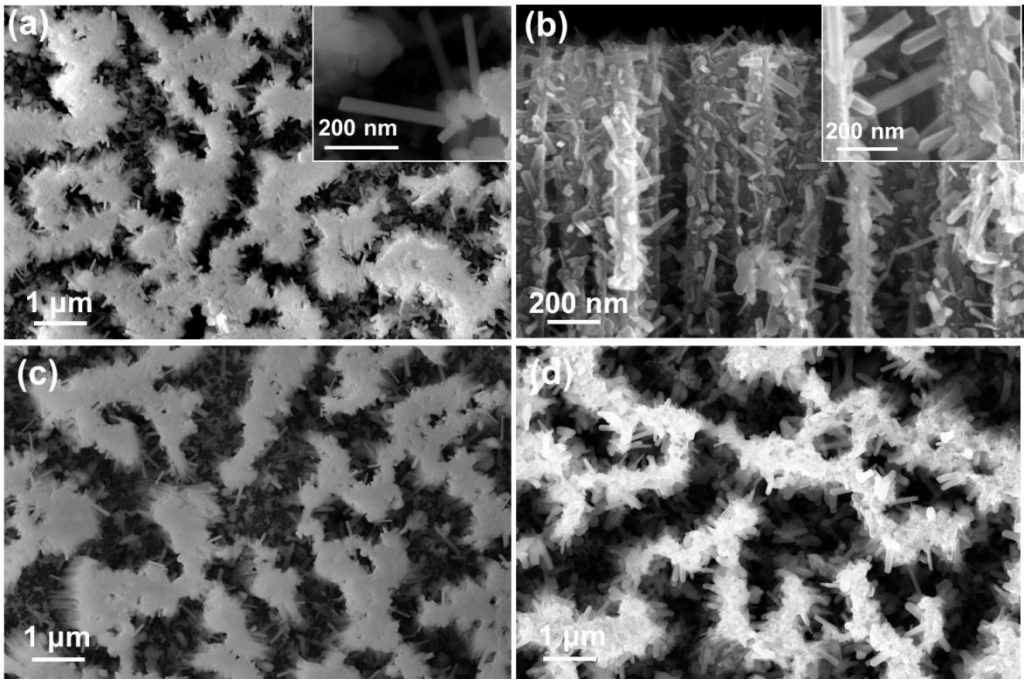

Figure 6.1. SEM of typical morphologies of different VO_x NRs@Si NWs hierarchical structures. (a) top view and (b) cross section view of as-synthesized one; insets indicating the dimensions of the NR branches were ~250 nm in length and ~30 nm in diameter. (c,d) VO_x NRs@Si NWs after thermal annealing in H_2 (c) and O_2 (d). The hierarchical structures were well preserved.

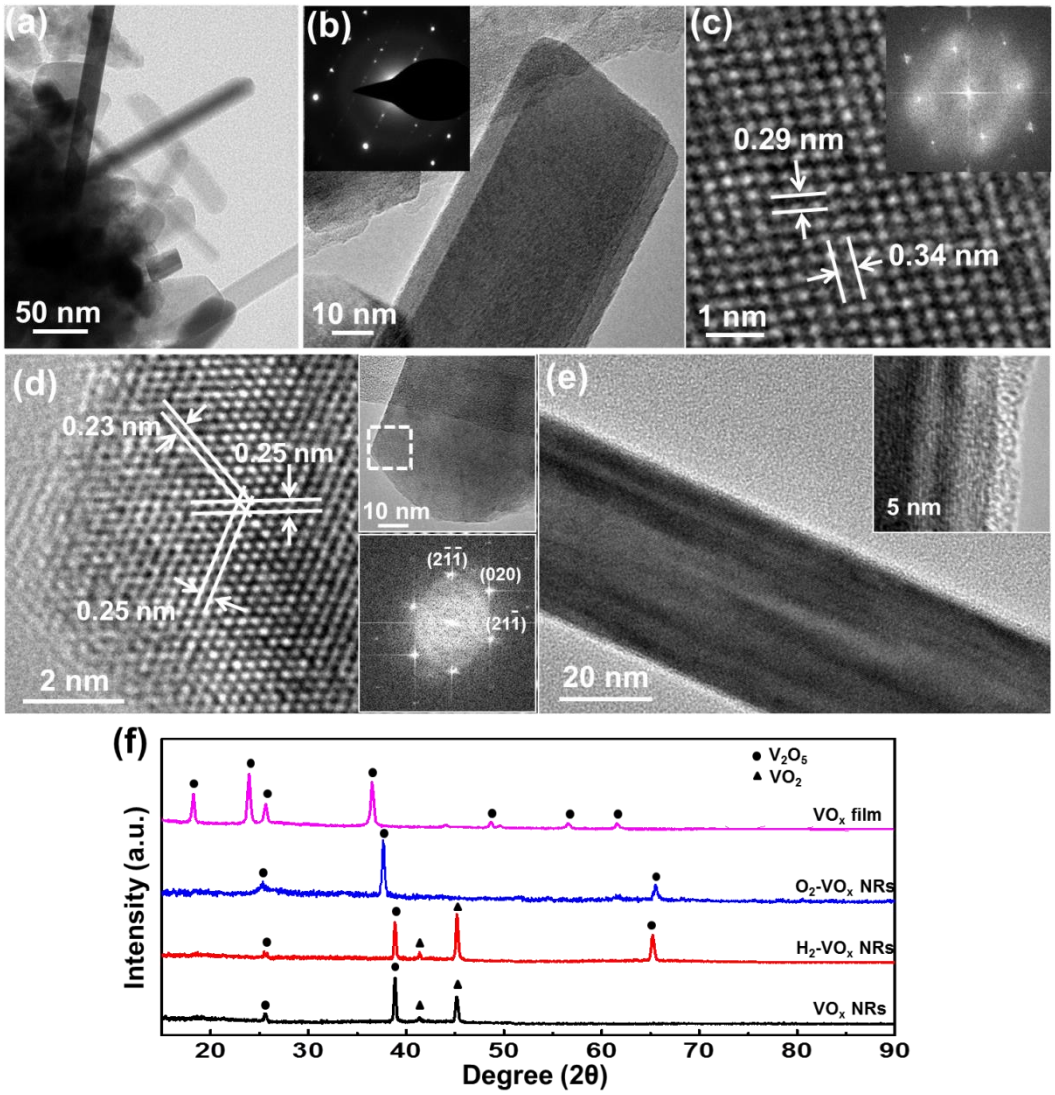

Figure 6.2. TEM images of typical morphologies and crystal structures of different VO_x NRs@Si NWs hierarchical structures. (a) Si backbone are uniformly covered by ultrathin NRs. (b) HRTEM image show the rectangular shape of the NR with a flat tip surface. Inset SAED pattern confirmed single crystallinity of the V_2O_5 phase, and (c) the lattice fringes were indexed as the (301) and (110) planes of V_2O_5, respectively. (d) VO_2 NRs was also found for some NR. (e) After H_2 annealing, a ~2 nm percolated layer was observed on the NR surface. (f) XRD characterization indicating the mixed phase and phase evolution of VO_x NRs upon different heat treatments.

to the flat-tip NRs. Nonetheless, these NRs were found to be the VO_2 phase. As shown by the HRTEM (Figure 6.2 d), the lattice spacing was determined to be 0.23, 0.25 and 0.25 nm from FFT, matching well to the (020), $(2\bar{1}\bar{1})$ and $(21\bar{1})$ planes of VO_2. Therefore, the as-synthesized VO_x NRs contained both V_2O_5 and VO_2 phases. Figure 6.2 e shows a VO_x NR after annealing in H_2 atmosphere. A ~2 nm percolated layer (mixture of amorphous and polycrystalline particles) was formed on the NR surface (Inset of Figure 6.2 e).

XRD was used to further analyze the mixed phase and phase evolution of VO_x NRs upon different heat treatments. As shown in Figure 6.2 f, both V_2O_5 and VO_2 exhibited significant signal in the as-received VO_x NR@Si samples. After H_2 treatment, the VO_2 phase became more dominant in the sample. Annealing the sample in O_2 atmosphere completely converted the VO_2 phase into V_2O_5. The mixed-valent of VO_x has been found beneficial for the electrochemical pseudocapacitor application.[52,204] It was also found that the pure V_2O_5 was obtained from ALD VO_x films grown at $350\,^\circ$C. The temperature-related phase variation was consistent with others' work where different valance states of vanadium was obtained in chemical vapor deposition of VO_x at different temperature using the same precursors ($VOCl_3$ and H_2O).[205,206]

The surface chemistry and elemental information of VO_x NRs and films are one essential factor for the supercapacitor performance, and they were studied by XPS. Figure 6.3a shows the full spectra of XPS survey scans from VO_x films, as-received, H-treated and O-treated VO_x NRs, in which elements of Si, V and O can be clearly identified. To

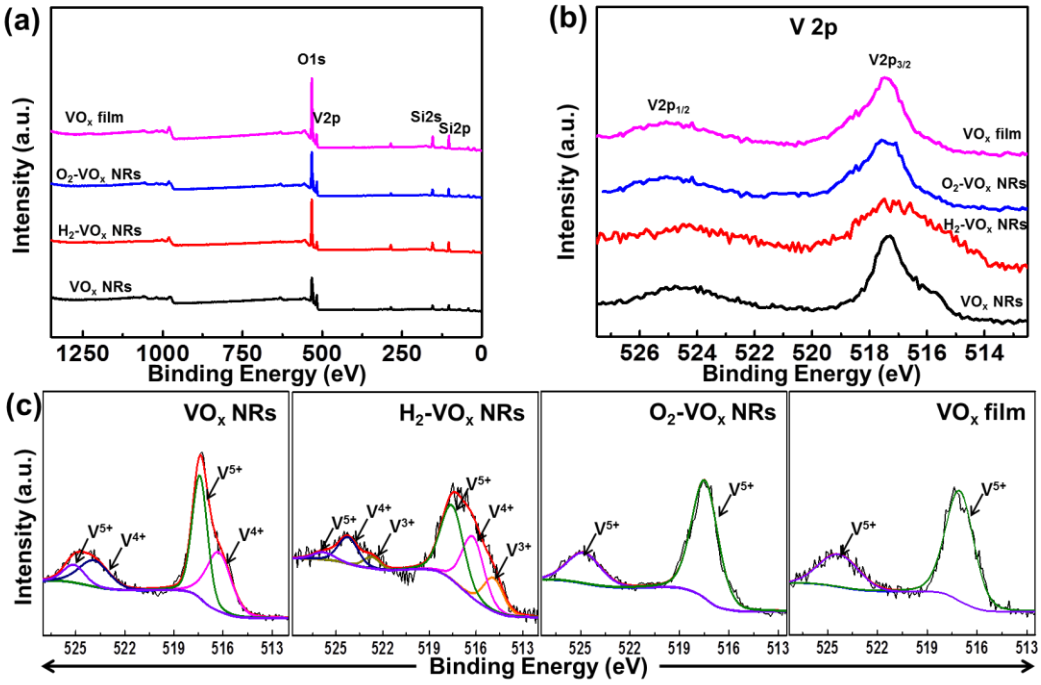

Figure 6.3. XPS characterization of VO_x NRs and films (a) Full XPS spectra. (b) V 2p scan near 520 eV. (c) The deconvoluted spectra for V 2p peak of all samples upon different prepare conditions. The mixed valence states were found in as-synthesized NRs. H_2 treatment introduced more mixed valence states, whereas O_2 treatment converted it into pure V_2O_5 pahse. The same pure V_2O_5 pahse was observed on ALD VOx film sample.

analyze the surface chemical states, the V 2p region near 520 eV of the XPS spectra were examined (Figure 6.3 b). All samples exhibited a typical two-peak structure (V $2p_{3/2}$ and V $2p_{1/2}$) due to the spin-orbit splitting. Broader V $2p_{3/2}$ and V $2p_{1/2}$ peaks were observed in as-synthesized VO_x NRs and H_2 treated VO_x NRs compared to those of O_2 treated VO_x NRs and VO_x films. In order to elucidate the different chemical binding states of V elements, the deconvoluted spectra for V 2p peaks were investigated (Figure 6.3c). The binding energies of V^{5+}, V^{4+}, and V^{3+} valence states to the V $2p_{3/2}$ peak could be assigned at 518.0, 516.4, and 514.8 eV, respectively. For the V $2p_{1/2}$ peak, such binding energies were assigned at 525.4, 524.1, and 522.4 eV, respectively.[204] The V^{5+} and V^{4+} states were observed in as-synthesized VO_x NRs, which was consistent to the TEM and XRD results. The valence states would be further reduced by extra H_2 treatment, and therefore, the V^{3+} states were discovered in H_2-VO_x NRs. However, V^{3+}-related structure was not observed from the XRD spectra, suggesting the amount of V^{3+} may not be significant enough to form as isolated phase and they might be contained in the percolated thin layer outside of the NRs. No lower chemical states of vanadium were observed from the oxygen-treated sample, further confirming that the VO_x NRs were fully transferred to the V_2O_5. The pure V_2O_5 phase was also obtained for the ALD vanadium oxide film sample.

The mixed valence states of metal oxide has been found being able to enable multiple charge storage mechanisms with small internal resistance, and highly reversible and faster charge transfer kinetics.[52] Owing to the mixed compositions of vanadium oxide, excellent surface/body ratios, and high conductive trunks, the 3D hierarchical VO_x

NRs@Si NWs heterostructure from SPCVD could be a promising electrode structure for supercapacitor design. Cyclic voltammetry (CV) measurement was performed on as-synthesized VO_x NRs in an 8 M LiCl solution with a scan rate from 1 mVs^{-1} to 2 Vs^{-1} (Figure 6.4a). The 1.2 V potential window (-0.5 V to 0.7 V) is the maximum value of VO_x based supercapacitors in LiCl electrolyte.[195,207] Although there was no distinct sharp redox peaks in the CV profile, the shape of the curve deviated from the ideal rectangle, implying its faradaic pseudocapacitive nature.[208] Weak but broad peaks were observed at -0.4V and 0.4 V indicating the charge exchange between the VO_x NRs and the LiCl electrolyte was almost independent to the applied voltage. This characteristic was very similar to that of hydrous ruthenium oxide, which was a characteristic of ideal pseudocapacitor-like materials.[204,209] Moreover, the symmetric shape of the CV curve suggested that the VO_x NRs@Si electrode was highly reversible up to 2 Vs^{-1}. This rate was higher than typically reported 0.1–1 V s^{-1} rates of oxide pseudocapacitors.[27,195,210] The current showed relatively sharp switches at the boundaries of potential window, which could be attributed to the fast ion diffusion[211] and low electrode resistance[204] as a result of the branched hierarchical nanoarchitecture, the reduced vanadium valence states, and the highly conductive Si backbone.

The VO_x phase-related electrochemical performance was then studied on hydrogen- and oxygen-treated samples. CV curves of H_2-VO_x NRs were shown in Figure 6.4 b. The broad peak in the central region of the curve was typically related to battery-like Faradaic reactions.[27] Such reactions were proposed to be the manifestation of

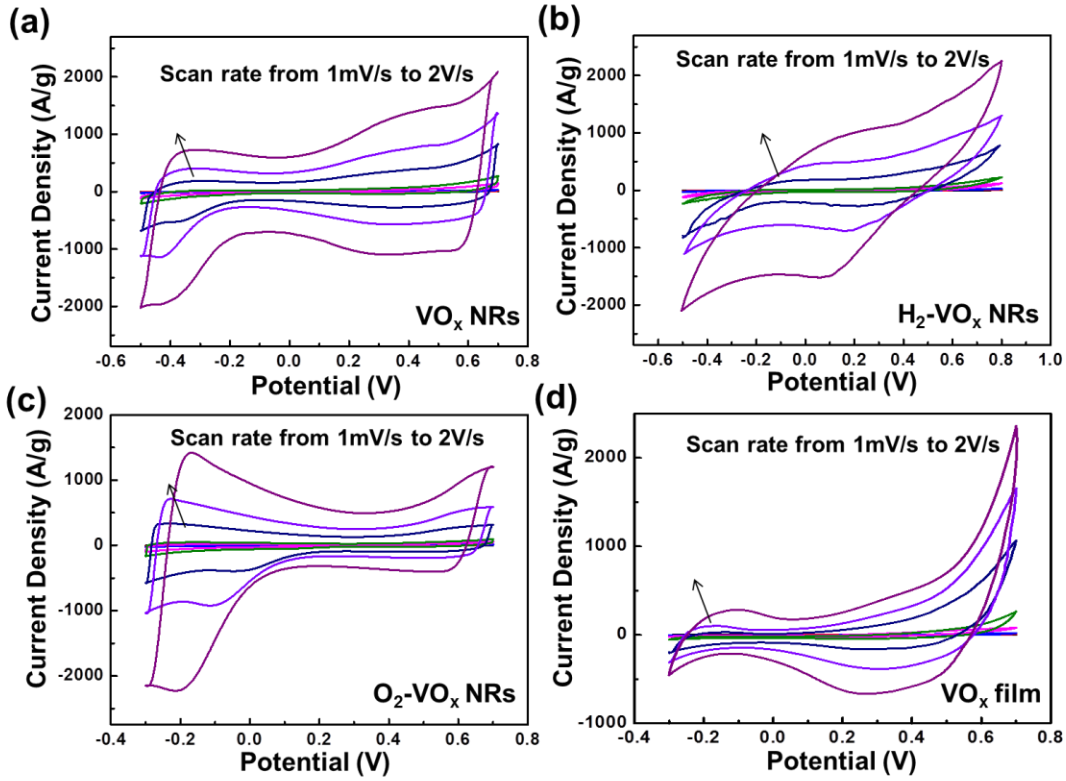

Figure 6.4. Cyclic voltammograms of different VOx-Si electrodes: (a) VO_x NRs@Si; (b) H_2-VO_x NRs@Si; (c) O_2-VO_x NRs@Si; (d) VO_x films@Si. Scan rates in the range of 1–2000 mVs^{-1}

.

intercalating process. This is possibly due to the existence of surface percolated layer, which might facilitate the insertion of Li ions into the VO_x NRs and may even reach the Si underneath. The H_2-VO_x NRs therefore exhibited a relatively poor stability in electrochemical reactions and higher degree of deviation from a rectangular CV curve. However, the synergistic effect of VO_x and Si was likely introduced in the electrochemical reaction.[212] Thus, larger potential window of 1.3 V was obtained compared to the as-synthesized VO_x NRs. When the VO_x NRs were converted to V_2O_5 NRs through oxygen annealing, the capacitance value significantly decreased as evidenced by the lower current density and narrower potential window (Figure 6.4 c). This behavior could be explained by the contribution of decreased electron transport due to the high resistivity of V_2O_5. Nonetheless, V_2O_5 is more chemical stable, which could be beneficial to the conservation of 3D hierarchical nanoarchitecture in electrochemical charging/discharging process. For comparison, the CV measurement was also applied on VO_x film samples (Figure 6.4 d). The same 1V potential window was obtained due to its pure V_2O_5 component. However, the capacitance of ALD VO_x film was much lower, which was mainly because of the low conductivity of the polycrystalline film and the decreased surface area of the film geometry. Meanwhile, the unsymmetrical curve indicated that the redox reaction was not very reversible, inferring the low chemical stability of the ALD VO_x film during charging/discharging processes.

Galvanostatic C-D was further conducted to reveal the specific capacitance of the supercapacitors at a constant current. The C-D profiles of each sample at different current

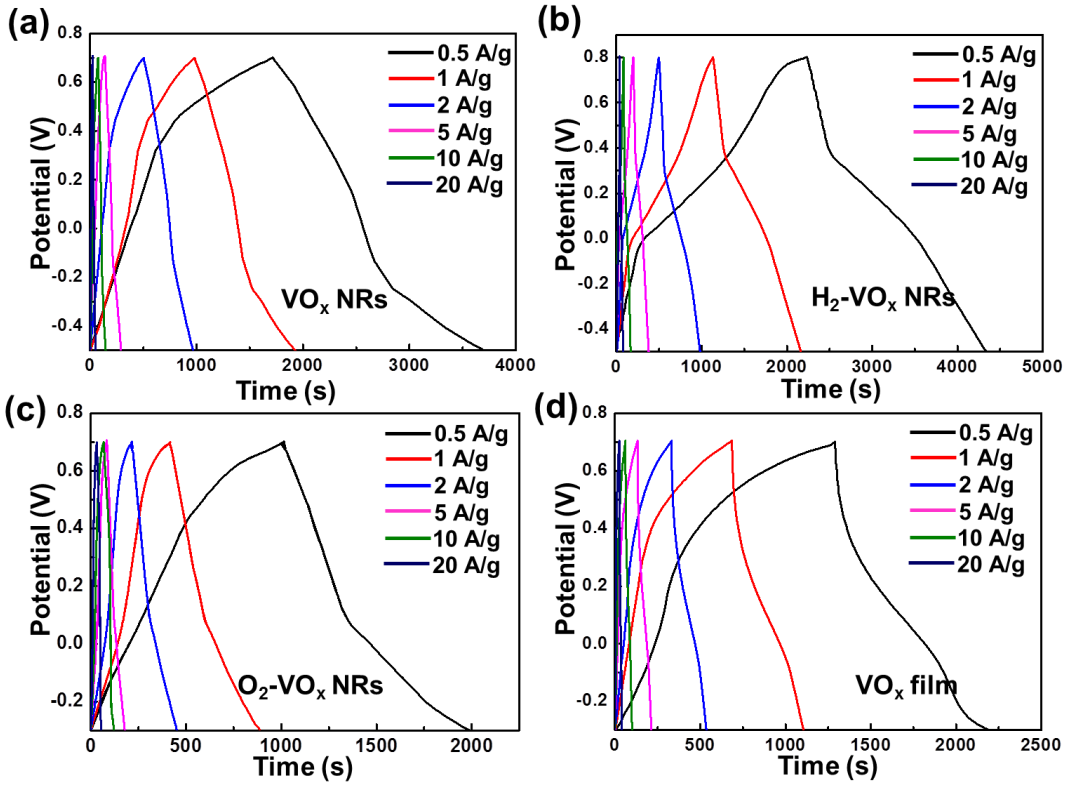

Figure 6.5. Charge–discharge profiles of different VO_x-Si electrodes: (a) VO_x NRs@Si; (b) H_2-VO_x NRs@Si; (c) O_2-VO_x NRs@Si; (d) VO_x films@Si. Current density in the range of 0.5–20 A g^{-1}.

.

densities from 0.5 to 20 Ag^{-1} were shown in Figure 6.5. The distorted linear shapes referred to the operation of pseudocapacitance for all samples, which further confirmed the faradaic pseudocapacitive appearance of the CV curves. It is noteworthy that a clear platform appeared when the charging process of H_2-VO_x NRs reached the positive potential boundary (Figure 6.5 b). Such a platform could be a result of ion intercalation and was usually observed in battery characterizations, which was consistent to the battery-like CV curves of H_2-VO_x NRs.[213-215] In generally, all electrodes exhibited good recyclability at high-current charging/discharging processes (Figure 6.6).

The specific capacitance as a function of the scanning rate and current density was calculated from the CV curves. First, the area mass densities (σ) of the active materials were determined by the following equation:

$$\sigma = \frac{m_{elec} - m_{Si\ NWs}}{A} \qquad (6.1)$$

where m_{elec} is the total mass of the electrode, $m_{Si\ NWs}$ is the mass of corresponding Si NWs substrate before the VO_x growth, A is the area of the electrode. The active mass area density were calculated to be 1.35×10^{-6} g cm^{-2} (VO_x NRs@Si NWs), 1.12×10^{-6} g cm^{-2} (H_2-VO_x NRs@Si NWs), 1.65×10^{-6} g cm^{-2} (O_2-VO_x NRs@Si NWs), and 7.79×10^{-5} g cm^{-2} (VO_x films@Si NWs). In the three-electrode system, the specific capacitance based on the total mass of active material from CV data was calculated according to the equation:

$$C = \frac{\Delta t}{2m\Delta V}\left(\int_{V^-}^{V^+} I(V)dV - \int_{V^+}^{V^-} I(V)dV\right) \qquad (6.2)$$

where Δt is the discharging time; m is the total mass of active material which can be

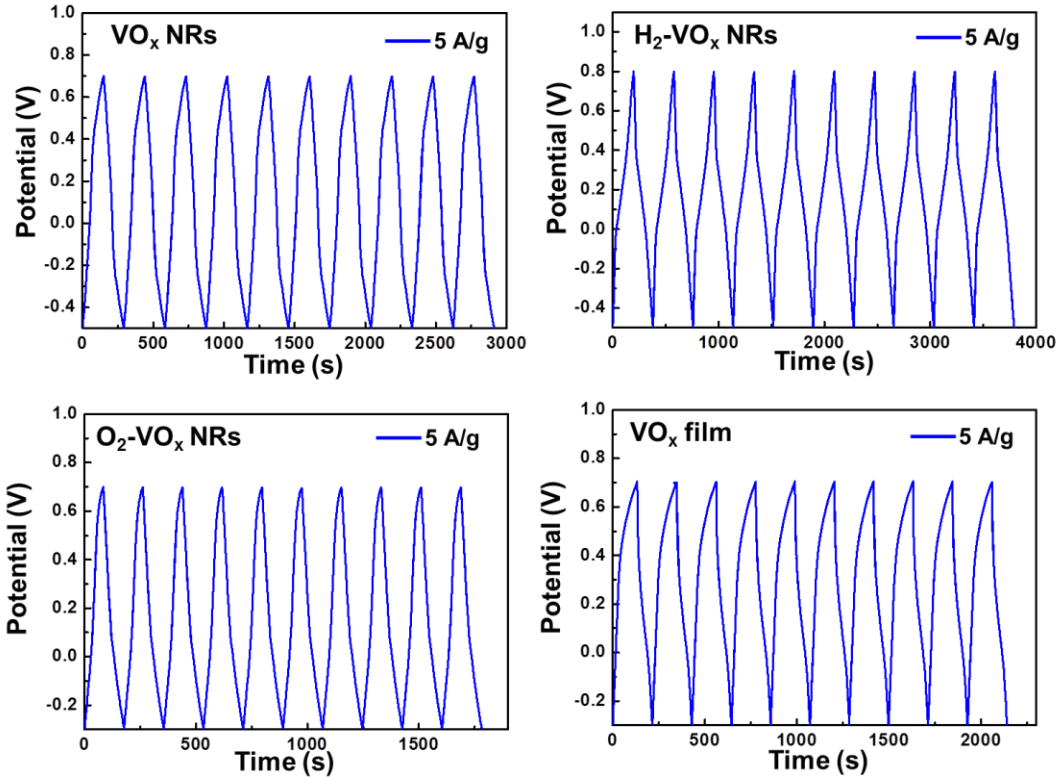

Figure 6.6. Repeated Charge-discharge behavior of fabricated VO_x-Si supercapacitor electrodes, which exhibited good recyclability at high-current (~5Ag^{-1}) charging/discharging processes.

determined from the product of the area mass densities and active area of each electrode; ΔV is the potential window of discharge; V^- and V^+ are the negative and positive boundary values of the potential window, respectively; I is the discharge current.

As shown in Figure 6.7 a, the as-received 3D hierarchical VO_x NRs@Si NWs electrode exhibited the highest specific capacitance of ~710 F g^{-1} at the scan rate of 1 mVs^{-1}. Even at the ultra-high sweeping rate of 2 Vs^{-1}, the capacitance remains as high as ~580 F g^{-1}, which was much higher than the reported values (~450 to 530 F g^{-1}) of VO_x-based supercapacitor electrodes.[27,53,204,216] Hydrogen treatment further improved the specific capacitance over all scan rates. A specific capacitance of ~930 F g^{-1} was achieved at 1 mVs^{-1} while the value decreased to ~590 F g^{-1} at a scan rate of 2 Vs^{-1}. However, the high-rate storage capability of the H_2-VO_xNRs electrode was suffered by its unstable structures as discussed above. The most stable high-rate storage capability was obtained from the oxygen-treated VO_x NRs, whereas the specific capacitance was much lower due to its resistive V_2O_5 component. The value was ~490 F g^{-1} at 1 mVs^{-1} and remained at ~450 F g^{-1} when the scan rate increased up to 2 Vs^{-1}. Although the ALD VO_x film had the same V_2O_5 component and lower exposed surface area compared to the O_2-VO_x NRs, the specific capacitance obtained at small scan rates was higher than that of O_2-VO_x NRs. It is known that the pseudocapacitance of oxides can approach a very high value at low scan rate (~ 1 mV s^{-1}) or when the particle sizes were very small, because under these two conditions, electrolyte ions and electrons can both penetrate to the entire volume of oxides.[204] The less condensed polycrystalline V_2O_5 film produced by ALD at 350 ℃

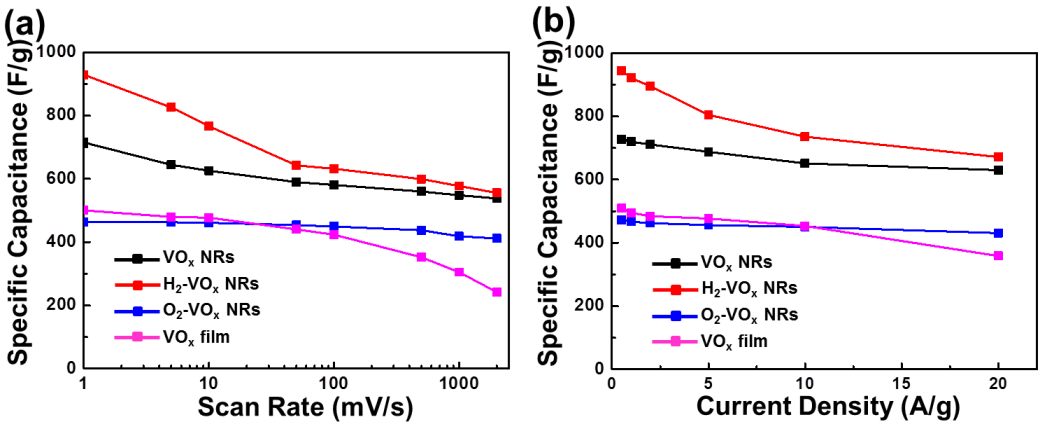

Figure 6.7. (a) Specific capacitances calculated from the cyclic voltammetry curves measured with various scan rates shown in Figure 6.4. (b) Specific capacitances calculated from galvanostatic charge/discharge with various current densities. H_2 and O_2 annealing were found to improve the specific capacitance and high-rate capability, respectively.

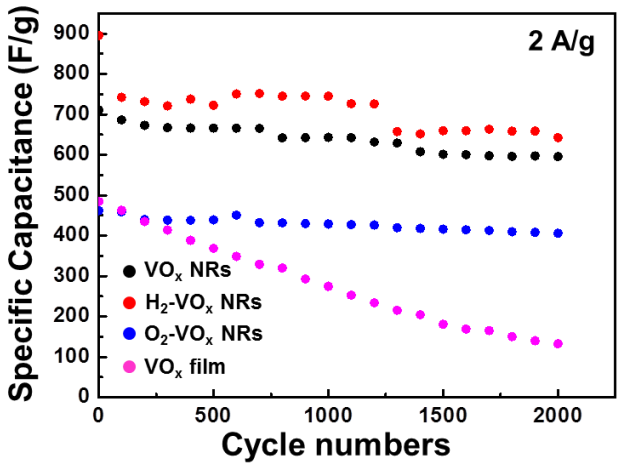

Figure 6.8. A typical specific capacitance values of different VO_x-Si electrodes as a function of charge–discharge cycle numbers.

would promote the penetration of ions and electrons into the metal oxide. When the scan rate was high, the specific capacitance of ALD film significantly decreased due to its low stability under faster redox reactions.

The specific capacitance as a function of the discharging current density was calculated from the C-D curves according to:

$$C = \frac{I\Delta t}{m\Delta V} \qquad (6.3)$$

As shown in Figure 6.7 b, with increasing current densities, the specific capacitance of all four samples decreased gradually. This observation revealed an excellent high-rate capability of the as-synthesized VO_x NRs@Si NWs as high-performance supercapacitor electrodes. Meanwhile, H_2 and O_2 annealing would further improve its specific capacitance and high-rate capability, respectively. The long-term capacitance retentions of all electrodes were evaluated by C–D characterization for 2000 cycles at a constant current density of 2 Ag^{-1} (Figure 6.8). The supercapacitor based on the as-synthesized VO_x NRs retained ~85% of the initial capacitance after 2000 cycles. Oxygen-treated sample showed the best stability with 93% capacity retained after the same number of charging/discharging cycles; while hydrogen-treated VO_x NRs had 71% capacity retained. The poorest stability was obtained from the VO_x films@Si NWs electrode, which only retained 31% of its original capacitance.

Electrochemical impedance spectroscopy (EIS) was further performed to understand the electronic or charge-carrier transport behavior of 3D hierarchical VO_x NRs@Si NWs structures. Nyquist plots derived from the EIS data were presented in

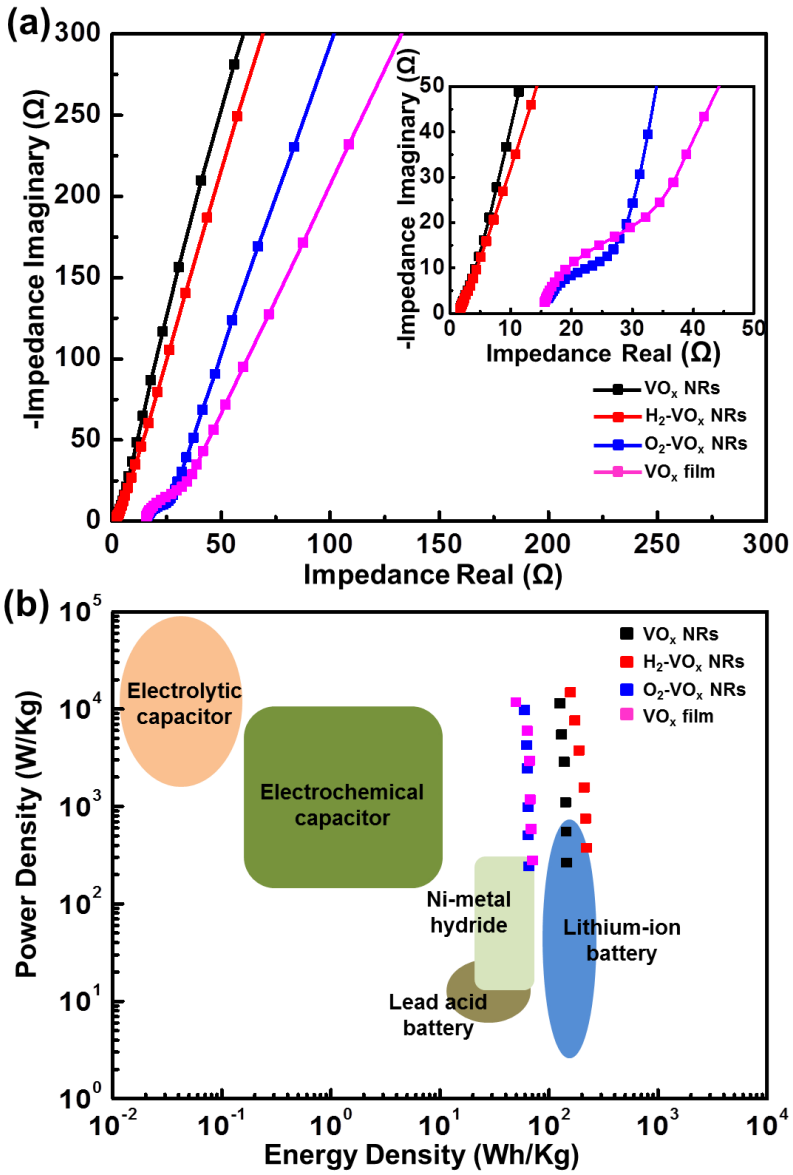

Figure 6.9. (a) Nyquist plots of different VO_x-Si electrodes obtained over the frequency range of 100 kHz to 0.01 Hz by applying 10 mV alternative signal versus the open-circuit voltage; the smallest circle diameter indicates the lowest of resistance in all VO_x NRs@Si NW electrode (inset is magnified figure at the high frequency). (b) Ragone plots of supercapacitors fabricated from different VO_x-Si architectures.

Figure 6.9a with enlarged details shown in the inset. All four electrodes in this work showed typical features of supercapacitors. In the high-frequency region, the size of the semicircle implied the existence of charge-transfer resistance. As shown in the inset of Figure 6.9 a, very small semicircles of both as-prepared and H_2 treated samples evidenced the rapid charge transport in these two electrodes. Besides, the charge-transfer resistances of all VO_x NRs samples in this work were found to be ranging from ~6 to ~16 Ω, which were comparable to the reported values (10-20 Ω) of vanadium oxide-carbon based electrodes and much lower than those of stacked and bulk V_2O_5 electrodes (30-60 Ω).[53,195] The equivalent series resistance (ESR) was determined from the first interception on the real axis of the Nyquist curve, which represents on the total resistance from electrolyte, electrodes, and the contact between the electrode and current collectors.[204,217,218] Small ESR was found from the as-synthesized and hydrogen-treated electrodes due to their better charge transport behavior. In addition, the increased slope of the line in the low-frequency region suggested an increased capacitive behavior for the as-synthesized and H_2 treated VO_x NRs.[219,220]

From the galvanostatic C-D results, the energy density (E) and power density (P) of each 3D hierarchical VO_x NRs@Si NWs structures were evaluated with a Ragone plot (Figure 6.9 b). The energy and power densities were calculated from the charge/discharge curves by the equations:

$$\mathrm{E} = \frac{C(\Delta V)^2}{2} \qquad (6.4)$$

$$P = \frac{E}{t} \qquad (6.5)$$

where E is the average energy density, C is the specific capacitance, ΔV is the discharge potential window, P is the average power density, and t is the discharge time. Strikingly, the as-synthesized 3D VO_x NRs@Si NWs structure exhibited a very high energy density of 145.5 W h kg^{-1} at a power density of 264.1 W kg^{-1}, and 126.0 W h kg^{-1} at a power density of 11.4 kW kg^{-1}. Both energy density and power density were even slightly higher for H_2-treated samples. Although the energy densities were significantly decreased from V_2O_5 based electrodes, these values were still better than the reported values of commercial supercapacitors.

6.4 Conclusion

In summary, we successfully synthesized high-density 3D hierarchical VO_x NRs@SiNWs structure for supercapacitor electrode development. The NW architecture could offer large surface areas, good charge transport properties, and mix-valance vanadium compositions. A 720 F g^{-1} specific capacitance was achieved from such 3D NW architecture at a discharging current density of 0.5A g^{-1}, which was 38.5 % higher than that of VO_x films@Si NWs structure. This comparison evidenced that a 3D NW architecture was superior to straight NW arrays for supercapacitor electrode design. Moreover, calcination of VO_x NRs in different atmospheres was able to engineer the valence state and phase of VO_x NRs, and thus tuned their supercapacitor performance. The specific capacitance could be further improved by introducing more mix-valence vanadium compositions through H_2 annealing, with the maximum value approached 950

F g^{-1} at 0.5A g^{-1}. O_2 annealing was able to convert all NRs to the pure V_2O_5 phase, which exhibited lower specific capacitances but enhanced high-rate capability and stability. The as-synthesized VO_x NRs had good cyclability with ~85% of the initial capacitance retained after 2000 cycles. Both energy density and power density were significantly improved by the 3D NW architectures compared to other reported regular geometries. This facile and low-cost technique introduced a novel route toward high-performance supercapacitor electrodes design using high-density 3D hierarchical NWs.

Chapter 7. Conclusion Remarks

ALD and SPCVD have been successfully utilized for the synthesis of various 3D nanoarchitectures with enhanced performance in the fields of solar energy harvesting and electrical energy storage. Accompanied with the rapid evolution of energy harvesting and storage technologies, the ALD-based nanomanufacturing technique is showing great potential to conduct large-area, low-cost, and simple fabrication of 3D mesoporous nanomaterials in these rapidly growing fields.

Innovative strategies were developed in this dissertation to address the existing challenges in photo-induced water splitting field and supercapacitor field in the following three aspects.

First, nitrogen-doped 3D TiO_2 nanorods architecture was synthesized to overcome the intrinsically light absorption constrains of metal oxide semiconductors. By introducing both TiN and TiO_2 growth cycles during the SPCVD process, the PEC activity was largely broaden to the visible light regime, and thus improved the overall solar-to-chemical energy conversion efficiency.

Second, to further improve the porosity and surface area while maintain good redox reaction kinetics, several 3D CNFs templated fibrous TiO_2 nanoarchitectures were synthesized with enhanced PEC performance. By further taking the advantage of the extreme hydrophilicity of CNF film, a novel capillary PEC process was invented. In this approach, the redox reactions were implemented outside of the electrolyte body, and thus

the water splitting reaction was no longer limited by the volume of water. The capillary design was applied to PEC photoanode and direct hydrogen generation, where the enhanced reaction kinetics and higher efficiency were obtained.

Third, to further explore the application potential of SPCVD in different material systems and application directions, high-density VO_x NRs were successfully synthesized by SPCVD on dense Si NW forests. Yielding a 3D hierarchical VO_x@Si NW architecture. This structure was applied to supercapacitor development, which exhibited high energy density, high-rate performance, and good stability.

The achievements presented in this dissertation open a new avenue of ALD toward large-area and low-cost nanomanufacture of novel nanostructured functional materials into the 3D space. Follow-up research along this line would have fundamental and practical study two aspects. Fundamentally, more comprehensive understanding of the nucleation and crystal growth kinetics, particularly to the atomic level is desired. Combining with atomistic simulation, this understanding can lead to a more general and versatile nanomanufacturing technique for different materials and different 3D geometries. Practically, understanding of the complex nanoscale morphology-related electronic, electrochemical, optical and mechanical properties will guide the design and development of more advanced nanomaterial systems for next generation energy harvesting and storage applications.

Reference

(1) Taniguchi, S.; Shibata, T.; Takeuchi, K. *Materials Transactions, JIM* **1991**, *32*, 299.

(2) Kordina, O.; Hallin, C.; Ellison, A.; Bakin, A. S.; Ivanov, I. G.; Henry, A.; Yakimova, R.; Touminen, M.; Vehanen, A.; Janzén, E. *Applied Physics Letters* **1996**, *69*, 1456.

(3) Knotek, O.; Löffler, F.; Bosserhoff, B. *Surface and Coatings Technology* **1993**, *62*, 630.

(4) Mattox, D. M. *Metal Finishing* **2001**, *99*, 409.

(5) Riihelä, D.; Ritala, M.; Matero, R.; Leskelä, M. *Thin Solid Films* **1996**, *289*, 250.

(6) T., S.; A., L.; J., W.; X., L.; S., R. *Solid State Technology* **2003**, *46*, 4.

(7) Ritala, M.; Leskelä, M. *Nanotechnology* **1999**, *10*, 19.

(8) Biener, M. M.; Biener, J.; Wichmann, A.; Wittstock, A.; Baumann, T. F.; Baumer, M.; Hamza, A. V. *Nano letters* **2011**, *11*, 3085.

(9) Puurunen, R. L. *Chemical Vapor Deposition* **2014**, *20*, 332.

(10) Goodman, C. H. L.; Pessa, M. V. *Journal of Applied Physics* **1986**, *60*, R65.

(11) Niinisto, L. *Current Opinion in Solid State & Materials Science* **1998**, *3*, 147.

(12) Niinisto, L.; Leskela, M. *Thin Solid Films* **1993**, *225*, 130.

(13) Suntola, T. *Thin Solid Films* **1992**, *216*, 84.

(14) Nishizawa, J.; Abe, H.; Kurabayashi, T. *Journal of the Electrochemical Society* **1985**, *132*, 1197.

(15) Fajula, F. *Journal of Catalysis* **1982**, *73*, 237.

(16) Nicolau, Y. F. *Applications of Surface Science* **1985**, *22-23*, 1061.

(17) Ito, K.; Nakazawa, T. *Japanese Journal of Applied Physics* **1988**, *27*, 2094.

(18) George, S. M. *Chemical reviews* **2010**, *110*, 111.

(19) George, S. M. *Chemical Reviews* **2010**, *110*, 111.

(20) Sneh, O.; Clark-Phelps, R. B.; Londergan, A. R.; Winkler, J.; Seidel, T. E. *Thin Solid Films* **2002**, *402*, 248.

(21) Yu, Y.; Li, Z.; Wang, Y.; Gong, S.; Wang, X. *Adv Mater* **2015**, *27*, 4938.

(22) Hu, S.; Lewis, N. S.; Ager, J. W.; Yang, J.; McKone, J. R.; Strandwitz, N. C. *The Journal of Physical Chemistry C* **2015**, *119*, 24201.

(23) Lewis, N. S. *Science* **2016**, *351*, aad1920.

(24) Lichterman, M. F.; Sun, K.; Hu, S.; Zhou, X.; McDowell, M. T.; Shaner, M. R.; Richter, M. H.; Crumlin, E. J.; Carim, A. I.; Saadi, F. H.; Brunschwig, B. S.; Lewis, N. S. *Catalysis Today* **2016**, *262*, 11.

(25) Paranjpe, A.; Gopinath, S.; Omstead, T.; Bubber, R. *Journal of The Electrochemical Society* **2001**, *148*, G465.

(26) Panwar, N. L.; Kaushik, S. C.; Kothari, S. *Renewable and Sustainable Energy Reviews* **2011**, *15*, 1513.

(27) Boukhalfa, S.; Evanoff, K.; Yushin, G. *Energy & Environmental Science* **2012**, *5*, 6872.

(28) Donders, M. E.; Arnoldbik, W. M.; Knoops, H. C. M.; Kessels, W. M. M.; Notten, P. H. L. *Journal of the Electrochemical Society* **2013**, *160*, A3066.

(29) Peng, Q.; Kalanyan, B.; Hoertz, P. G.; Miller, A.; Kim do, H.; Hanson, K.; Alibabaei, L.; Liu, J.; Meyer, T. J.; Parsons, G. N.; Glass, J. T. *Nano Lett* **2013**, *13*, 1481.

(30) Yu, Y.; Wang, X. *Extreme Mechanics Letters* **2016**.

(31) Chaaban, M. A.; El Chaar, L.; Alahmad, M. *International Journal of Photoenergy* **2015**, *2015*, 1.

(32) Yin, W.-J.; Tang, H.; Wei, S.-H.; Al-Jassim, M. M.; Turner, J.; Yan, Y. *Physical Review B* **2010**, *82*.

(33) Boettcher, S. W.; Spurgeon, J. M.; Putnam, M. C.; Warren, E. L.; Turner-Evans, D. B.; Kelzenberg, M. D.; Maiolo, J. R.; Atwater, H. A.; Lewis, N. S. *Science* **2010**, *327*, 185.

(34) Shi, J.; Hara, Y.; Sun, C.; Anderson, M. A.; Wang, X. *Nano letters* **2011**, *11*, 3413.

(35) Wang, F.; Seo, J. H.; Li, Z.; Kvit, A. V.; Ma, Z.; Wang, X. *ACS applied materials & interfaces* **2014**, *6*, 1288.

(36) Wang, T.; Luo, Z.; Li, C.; Gong, J. *Chemical Society reviews* **2014**, *43*, 7469.

(37) Wang, X.; Li, Z.; Shi, J.; Yu, Y. *Chem Rev* **2014**, *114*, 9346.

(38) Nozik, A. J. *Ann. Rev. Phys. Cher.* **1978**, *29*, 34.

(39) Cheng, H.-E.; Chen, C.-C. *Journal of The Electrochemical Society* **2008**, *155*, D604.

(40) Noh, J. H.; Ding, B.; Soo Han, H.; Seong Kim, J. *Applied Physics Letters* **2012**, *100*, 084104.

(41) Weng, B.; Xu, F.; Xu, J. *Nanotechnology* **2014**, *25*, 455402.

(42) Yongjing, L.; Sa, Z.; Sheehan, S. W.; Dunwei, W. *J Am Chem Soc* **2011**, *133*, 2398.

(43) Pore, V.; Heikkilä, M.; Ritala, M.; Leskelä, M.; Areva, S. *Journal of Photochemistry and Photobiology A: Chemistry* **2006**, *177*, 68.

(44) Lin, Y.; Yang, X.; Mayer, M. T.; Simpson, Z. I.; Mcmahon, G.; Zhou, S.; Wang, D. *J Am Chem Soc* **2012**, *134*, 5508.

(45) Walter, M. G.; Warren, E. L.; McKone, J. R.; Boettcher, S. W.; Mi, Q.; Santori, E. A.; Lewis, N. S. *Chem Rev* **2010**, *110*, 6446.

(46) Kenney, M. J.; Gong, M.; Li, Y.; Wu, J. Z.; Feng, J.; Lanza, M.; Dai, H. *Science* **2013**, *342*, 836.

(47) Ji, L.; McDaniel, M. D.; Wang, S.; Posadas, A. B.; Li, X.; Huang, H.; Lee, J. C.; Demkov, A. A.; Bard, A. J.; Ekerdt, J. G.; Yu, E. T. *Nat Nanotechnol* **2015**, *10*, 84.

(48) Sun, K.; Saadi, F. H.; Lichterman, M. F.; Hale, W. G.; Wang, H. P.; Zhou, X.; Plymale, N. T.; Omelchenko, S. T.; He, J. H.; Papadantonakis, K. M.; Brunschwig, B. S.; Lewis, N. S. *Proc Natl Acad Sci U S A* **2015**, *112*, 3612.

(49) Hu, S.; Shaner, M. R.; Beardslee, J. A.; Lichterman, M.; Brunschwig, B. S.; Lewis, N. S. *Science* **2014**, *344*, 1005.

(50) Shaner, M. R.; Hu, S.; Sun, K.; Lewis, N. S. *Energy Environ. Sci.* **2015**, *8*, 203.

(51) Wei, D.; Scherer, M. R.; Bower, C.; Andrew, P.; Ryhanen, T.; Steiner, U. *Nano Lett* **2012**, *12*, 1857.

(52) Song, M. K.; Cheng, S.; Chen, H.; Qin, W.; Nam, K. W.; Xu, S.; Yang, X. Q.; Bongiorno, A.; Lee, J.; Bai, J.; Tyson, T. A.; Cho, J.; Liu, M. *Nano letters* **2012**, *12*, 3483.

(53) Zhu, J.; Cao, L.; Wu, Y.; Gong, Y.; Liu, Z.; Hoster, H. E.; Zhang, Y.; Zhang, S.; Yang, S.; Yan, Q.; Ajayan, P. M.; Vajtai, R. *Nano letters* **2013**, *13*, 5408.

(54) Gnerlich, M.; Pomerantseva, E.; Gregorczyk, K.; Ketchum, D.; Rubloff, G.; Ghodssi, R. *Journal of Micromechanics and Microengineering* **2013**, *23*, 114014.

(55) Warren, R.; Sammoura, F.; Kozinda, A.; Lin, L. In *Micro Electro Mechanical Systems (MEMS), 2014 IEEE 27th International Conference on* 2014, p 167.

(56) Warren, R.; Sammoura, F.; Tounsi, F.; Sanghadasa, M.; Lin, L. *Journal of Materials Chemistry A* **2015**, *3*, 15568.

(57) L. Kavan, §; M. Grätzel, †; S. E. Gilbert; C. Klemenz, a.; Scheel‡, H. J. *J.am.chem.soc* **1996**, *118*, 6716.

(58) Zhang, M.; Fang, S.; Zakhidov, A. A.; Lee, S. B.; Aliev, A. E.; Williams, C. D.; Atkinson, K. R.; Baughman, R. H. *Science* **2005**, *309*, 1215.

(59) Lota, G.; Fic, K.; Frackowiak, E. *Energy & Environmental Science* **2011**, *4*, 1592.

(60) Zheng, G.; Hu, L.; Wu, H.; Xie, X.; Cui, Y. *Energy & Environmental Science* **2011**, *4*, 3368.

(61) Barisci*, J. N.; Wallace*, G. G.; Baughman, R. H. *Journal of Electroanalytical Chemistry* **2000**, *488*, 92.

(62) Sun, X.; Xie, M.; Wang, G.; Sun, H.; Cavanagh, A. S.; Travis, J. J.; George, S. M.; Lian, J. *Journal of The Electrochemical Society* **2012**, *159*, A364.

(63) Li, H.; Gao, Y.; Shao, Y.; Su, Y.; Wang, X. *Nano Letters* **2015**, *15*.

(64) Guan, C.; Xia, X.; Meng, N.; Zeng, Z.; Cao, X.; Soci, C.; Zhang, H.; Fan, H. J. *Energy & Environmental Science* **2012**, *5*, 9085.

(65) Zhang, X.; Lu, X.; Shen, Y.; Han, J.; Yuan, L.; Gong, L.; Xu, Z.; Bai, X.; Wei, M.; Tong, Y. *Chemical communications* **2011**, *47*, 5804.

(66) Yang, J.-S.; Liao, W.-P.; Wu, J.-J. *ACS applied materials & interfaces* **2013**, *5*, 7425.

(67) Noh, S. Y.; Sun, K.; Choi, C.; Niu, M.; Yang, M.; Xu, K.; Jin, S.; Wang, D. *Nano Energy* **2013**, *2*, 351.

(68) Wang, X.; Li, X.; Li, X.; Xu, L.; Liu, Z.; Duan, L.; Liu, J. *Journal of Materials Chemistry A* **2014**, *2*, 12304.

(69) Cao, F.; Shi, W.; Zhao, L.; Song, S.; Yang, J.; Lei, Y.; Zhang, H. *The Journal of Physical Chemistry C* **2008**, *112*, 17095.

(70) Shi, J.; Sun, C.; Starr, M. B.; Wang, X. *Nano letters* **2011**, *11*, 624.

(71) Shi, J.; Li, Z.; Kvit, A.; Krylyuk, S.; Davydov, A. V.; Wang, X. *Nano letters* **2013**, *13*, 5727.

(72) Shi, J.; Wang, X. *Energy & Environmental Science* **2012**, *5*, 7918.

(73) Yu, Y.; Yin, X.; Kvit, A.; Wang, X. *Nano letters* **2014**, *14*, 2528.

(74) Xiong, Z.; Zhao, X. S. *Journal of the American Chemical Society* **2012**, *134*, 5754.

(75) Wang, J.; Tafen de, N.; Lewis, J. P.; Hong, Z.; Manivannan, A.; Zhi, M.; Li, M.; Wu, N. *Journal of the American Chemical Society* **2009**, *131*, 12290.

(76) Li, Z.; Yao, C.; Yu, Y.; Cai, Z.; Wang, X. *Adv Mater* **2014**, *26*, 2262.

(77) Cho, I. S.; Chen, Z.; Forman, A. J.; Kim, D. R.; Rao, P. M.; Jaramillo, T. F.; Zheng, X. *Nano letters* **2011**, *11*, 4978.

(78) Fujishima, A.; Honda, K. *Nature* **1972**, *238*, 37.

(79) Cho, I. S.; Lee, C. H.; Feng, Y.; Logar, M.; Rao, P. M.; Cai, L.; Kim, D. R.; Sinclair, R.; Zheng, X. *Nature communications* **2013**, *4*, 1723.

(80) Ohno, T.; Murakami, N. *Current Organic Chemistry* **2010**, *14*, 699.

(81) Park, J. H.; Kim, S.; Bard, A. J. *Nano letters* **2006**, *6*, 24.

(82) Khan, S. U.; Al-Shahry, M.; Ingler, W. B., Jr. *Science* **2002**, *297*, 2243.

(83) Chen, X.; Burda, C. *Journal of the American Chemical Society* **2008**, *130*, 5018.

(84) Morikawa, T.; Asahi, R.; Ohwaki, T.; Aoki, K.; Taga, Y. *Japanese Journal of Applied Physics* **2001**, *40*, L561.

(85) Burda, C.; Lou, Y.; Chen, X.; Samia, A. C. S.; Stout, J.; Gole, J. L. *Nano letters* **2003**, *3*, 1049.

(86) Asahi, R.; Morikawa, T.; Ohwaki, T.; Aoki, K.; Taga, Y. *Science* **2001**, *293*, 269.

(87) Tang, Y.-C.; Huang, X.-H.; Yu, H.-Q.; Tang, L.-H. *International Journal of Photoenergy* **2012**, *2012*, 1.

(88) Dunnill, C. W.; Parkin, I. P. *Chemical Vapor Deposition* **2009**, *15*, 171.

(89) Shen, H.; Mi, L.; Xu, P.; Shen, W.; Wang, P.-N. *Applied Surface Science* **2007**, *253*, 7024.

(90) Yang, Y.; Zhong, H.; Tian, C. *Research on Chemical Intermediates* **2010**, *37*, 91.

(91) Morikawa, T.; Asahi, R.; Ohwaki, T.; Aoki, K.; Suzuki, K.; Taga, Y. *R&D Review of Toyota CRDL* **2005**, *40*.

(92) Burda, C.; El-Sayed, M. A. *Pure and Applied Chemistry* **2000**, *72*.

(93) Devi, L. G.; Kavitha, R. *Applied Catalysis B: Environmental* **2013**, *140-141*, 559.

(94) Hoang, S.; Berglund, S. P.; Hahn, N. T.; Bard, A. J.; Mullins, C. B. *Journal of the American Chemical Society* **2012**, *134*, 3659.

(95) Tian, H.; Hu, L.; Zhang, C.; Liu, W.; Huang, Y.; Mo, L.; Guo, L.; Sheng, J.; Dai, S. *The Journal of Physical Chemistry C* **2010**, *114*, 1627.

(96) Choi, W.; Termin, A.; Hoffmann, M. R. *The Journal of Physical Chemistry* **1994**, *98*, 13669.

(97) Liu, B.; Chen, H. M.; Liu, C.; Andrews, S. C.; Hahn, C.; Yang, P. *Journal of the American Chemical Society* **2013**, *135*, 9995.

(98) Devi, L. G.; Kottam, N.; Kumar, S. G. *The Journal of Physical Chemistry C* **2009**, *113*, 15593.

(99) Yu, J.; Xiang, Q.; Zhou, M. *Applied Catalysis B: Environmental* **2009**, *90*, 595.

(100) Chen, X.; Liu, L.; Yu, P. Y.; Mao, S. S. *Science* **2011**, *331*, 746.

(101) Devi, L. G.; Kumar, S. G. *Applied Surface Science* **2011**, *257*, 2779.

(102) Ma, X.; Wu, Y.; Lu, Y.; Xu, J.; Wang, Y.; Zhu, Y. *The Journal of Physical Chemistry C* **2011**, *115*, 16963.

(103) Elers, K.-E.; Winkler, J.; Weeks, K.; Marcus, S. *Journal of The Electrochemical Society* **2005**, *152*, G589.

(104) Wang, F.; Hwang, Y.; Qian, P. Z.; Wang, X. *ACS nano* **2010**, *4*, 855.

(105) Saha, N. C.; Tompkins, H. G. *Journal of Applied Physics* **1992**, *72*, 3072.

(106) Chen, X.; Burda, C. *The Journal of Physical Chemistry B* **2004**, *108*, 15446.

(107) Jagadale, T. C.; Takale, S. P.; Sonawane, R. S.; Joshi, H. M.; Patil, S. I.; Kale, B. B.; Ogale, S. B. *The Journal of Physical Chemistry C* **2008**, *112*, 14595.

(108) Sham, T. K.; Lazarus, M. S. *Chemical Physics Letters* **1979**, *68*, 426.

(109) Hashimoto, S.; Murata, A.; Sakurada, T.; Tanaka, A. *Journal of Surface Analysis* **2002**, *9*, 459.

(110) Cai, J.; Huang, Z. a.; Lv, K.; Sun, J.; Deng, K. *RSC Advances* **2014**, *4*, 19588.

(111) Shi, J.; Sun, C.; Starr, M. B.; Wang, X. *Nano letters* **2011**, *11*, 624.

(112) Dalpian, G.; Chelikowsky, J. *Physical Review Letters* **2006**, *96*.

(113) Norris, D. J.; Efros, A. L.; Erwin, S. C. *Science* **2008**, *319*, 1776.

(114) Yankovich, A. B.; Puchala, B.; Wang, F.; Seo, J. H.; Morgan, D.; Wang, X.; Ma, Z.; Kvit, A. V.; Voyles, P. M. *Nano letters* **2012**, *12*, 1311.

(115) Rosenberg, R. *Journal of Vacuum Science and Technology* **1972**, *9*, 263.

(116) Morisaki, H.; Hariya, M.; Yazawa, K. *Applied Physics Letters* **1977**, *30*, 7.

(117) Wang, G.; Wang, H.; Ling, Y.; Tang, Y.; Yang, X.; Fitzmorris, R. C.; Wang, C.; Zhang, J. Z.; Li, Y.

Nano letters **2011**, *11*, 3026.

(118) Murphy, A.; Barnes, P.; Randeniya, L.; Plumb, I.; Grey, I.; Horne, M.; Glasscock, J. *International Journal of Hydrogen Energy* **2006**, *31*, 1999.

(119) Rao, P. M.; Cai, L.; Liu, C.; Cho, I. S.; Lee, C. H.; Weisse, J. M.; Yang, P.; Zheng, X. *Nano letters* **2014**, *14*, 1099.

(120) Zhang, Z.; Yang, X.; Hedhili, M. N.; Ahmed, E.; Shi, L.; Wang, P. *ACS applied materials & interfaces* **2014**, *6*, 691.

(121) Ventosa, E.; Xia, W.; Klink, S.; La Mantia, F.; Mei, B.; Muhler, M.; Schuhmann, W. *Chemistry* **2013**, *19*, 14194.

(122) Maeda, K.; Domen, K. *J Phys Chem Lett* **2010**, *1*, 2655.

(123) Su, J.; Feng, X.; Sloppy, J. D.; Guo, L.; Grimes, C. A. *Nano letters* **2011**, *11*, 203.

(124) Chen, X.; Shen, S.; Guo, L.; Mao, S. S. *Chemical reviews* **2010**, *110*, 6503.

(125) Yin, W.-J.; Tang, H.; Wei, S.-H.; Al-Jassim, M. M.; Turner, J.; Yan, Y. *Physical Review B* **2010**, *82*.

(126) Hwang, Y. J.; Boukai, A.; Yang, P. *Nano letters* **2009**, *9*, 410.

(127) Kim, J.-H.; Yun, T. K.; Bae, J.-Y.; Ahn, K.-S. *Japanese Journal of Applied Physics* **2009**, *48*, 120204.

(128) Shen, X.; Sun, B.; Yan, F.; Zhao, J.; Zhang, F.; Wang, S.; Zhu, X.; Lee, S. *ACS nano* **2010**, *4*, 5869.

(129) Cheng, C.; Fan, H. J. *Nano Today* **2012**, *7*, 327.

(130) Zeng, J.; Li, R.; Liu, S.; Zhang, L. *ACS applied materials & interfaces* **2011**, *3*, 2074.

(131) Liu, S.; Tao, D.; Bai, H.; Liu, X. *Journal of Applied Polymer Science* **2012**, *126*, E282.

(132) Moon, R. J.; Martini, A.; Nairn, J.; Simonsen, J.; Youngblood, J. *Chemical Society reviews* **2011**, *40*, 3941.

(133) Wang, B. *PhD Thesis, University of Toronto* **2008**.

(134) Serizawa, T.; Sawada, T.; Okura, H.; Wada, M. *Biomacromolecules* **2013**, *14*, 613.

(135) Jabbour, L.; Gerbaldi, C.; Chaussy, D.; Zeno, E.; Bodoardo, S.; Beneventi, D. *Journal of Materials Chemistry* **2010**, *20*, 7344.

(136) Jabbour, L.; Destro, M.; Gerbaldi, C.; Chaussy, D.; Penazzi, N.; Beneventi, D. *Nord Pulp Pap Res J* **2012**, *27*, 472.

(137) Kemell, M.; Pore, V.; Ritala, M.; Leskela, M.; Linden, M. *Journal of the American Chemical Society* **2005**, *127*, 14178.

(138) Ghadiri, E.; Taghavinia, N.; Zakeeruddin, S. M.; Gratzel, M.; Moser, J. E. *Nano letters* **2010**, *10*, 1632.

(139) Wang, H. H.; Zhu, E. W.; Yang, J. Z.; Zhou, P. P.; Sun, D. P.; Tang, W. H. *Journal of Physical Chemistry C* **2012**, *116*, 13013.

(140) Qing, Y.; Sabo, R.; Cai, Z.; Wu, Y. *Cellulose* **2012**, *20*, 303.

(141) Saito, T.; Hirota, M.; Tamura, N.; Kimura, S.; Fukuzumi, H.; Heux, L.; Isogai, A. *Biomacromolecules* **2009**, *10*, 1992.

(142) Korhonen, J. T.; Hiekkataipale, P.; Malm, J.; Karppinen, M.; Ikkala, O.; Ras, R. H. *ACS nano* **2011**, *5*, 1967.

(143) Shi, J. A.; Wang, X. D. *Cryst Growth Des* **2011**, *11*, 949.

(144) Liu, C.; Tang, J.; Chen, H. M.; Liu, B.; Yang, P. *Nano letters* **2013**, *13*, 2989.

(145) Kargar, A.; Sun, K.; Jing, Y.; Choi, C.; Jeong, H.; Zhou, Y.; Madsen, K.; Naughton, P.; Jin, S.; Jung, G. Y.; Wang, D. *Nano letters* **2013**, *13*, 3017.

(146) Kargar, A.; Sun, K.; Jing, Y.; Choi, C.; Jeong, H.; Jung, G. Y.; Jin, S.; Wang, D. *ACS nano* **2013**, *7*, 9407.

(147) Morgan, B. J.; Watson, G. W. *The Journal of Physical Chemistry C* **2010**, *114*, 2321.

(148) Wu, N.; Wang, J.; Tafen de, N.; Wang, H.; Zheng, J. G.; Lewis, J. P.; Liu, X.; Leonard, S. S.; Manivannan, A. *Journal of the American Chemical Society* **2010**, *132*, 6679.

(149) Nozik, A. J. *Annual Review of Physical Chemistry* **1978**, *29*, 189.

(150) Le Formal, F.; Tétreault, N.; Cornuz, M.; Moehl, T.; Grätzel, M.; Sivula, K. *Chem. Sci.* **2011**, *2*, 737.

(151) Sanchez, C.; Sieber, K. D.; Somorjai, G. A. *Journal of Electroanalytical Chemistry and Interfacial Electrochemistry* **1988**, *252*, 269.

(152) Kale, S. S.; Pathan, H. M.; Lokhande, C. D. *J Mater Sci* **2005**, *40*, 2635.

(153) Liu, C.-h. J. *Journal of The Electrochemical Society* **1982**, *129*, 719.

(154) Horowitz, G. *Journal of Electroanalytical Chemistry and Interfacial Electrochemistry* **1983**, *159*, 421.

(155) Dare-Edwards, M. P.; Goodenough, J. B.; Hamnett, A.; Trevellick, P. R. *Journal of the Chemical Society, Faraday Transactions 1: Physical Chemistry in Condensed Phases* **1983**, *79*, 2027.

(156) Ono, K. *Electrical Engineering in Japan* **2015**, *190*, 1.

(157) Rausch, B.; Symes, M. D.; Chisholm, G.; Cronin, L. *Science* **2014**, *345*, 1326.

(158) Vorontsov, A. V.; Savinov, E. N.; Zhensheng, J. *Journal of Photochemistry and Photobiology A: Chemistry* **1999**, *125*, 113.

(159) Hoffmann, M. R.; Martin, S. T.; Choi, W.; Bahnemann, D. W. *Chemical reviews* **1995**, *95*, 69.

(160) Moon, S.-C.; Mametsuka, H.; Tabata, S.; Suzuki, E. *Catalysis Today* **2000**, *58*, 125.

(161) Abe, R.; Sayama, K.; Arakawa, H. *Chemical Physics Letters* **2003**, *371*, 360.

(162) Galińska, A.; Walendziewski, J. *Energy & Fuels* **2005**, *19*, 1143.

(163) Chen, T.; Feng, Z.; Wu, G.; Shi, J.; Ma, G.; Ying, P.; Li, C. *Journal of Physical Chemistry C* **2007**, *111*, 8005.

(164) Yu, J.; Qi, L.; Jaroniec, M. *The Journal of Physical Chemistry C* **2010**, *114*, 13118.

(165) Tabata, S.; Nishida, H.; Masaki, Y.; Tabata, K. *Catalysis Letters* **1995**, *34*, 245.

(166) Herrmann, J. M.; Disdier, J.; Pichat, P. *The Journal of Physical Chemistry* **1986**, *90*, 6028.

(167) Wang, C.; Yin, L.; Zhang, L.; Liu, N.; Lun, N.; Qi, Y. *ACS applied materials & interfaces* **2010**, *2*, 3373.

(168) Sayama, K.; Arakawa, H. *Journal of the Chemical Society, Faraday Transactions* **1997**, *93*, 1647.

(169) Zhang, F.; Chen, J.; Zhang, X.; Gao, W.; Jin, R.; Guan, N.; Li, Y. *Langmuir : the ACS journal of surfaces and colloids* **2004**, *20*, 9329.

(170) Li, Z.; Yao, C.; Yu, Y.; Cai, Z.; Wang, X. *Advanced materials* **2014**, *26*, 2262.

(171) Huang, X.-J.; Chen, P.-C.; Huang, F.; Ou, Y.; Chen, M.-R.; Xu, Z.-K. *Journal of Molecular*

Catalysis B: Enzymatic **2011**, *70*, 95.

(172) Young, J. K.; Lewinski, N. A.; Langsner, R. J.; Kennedy, L. C.; Satyanarayan, A.; Nammalvar, V.; Lin, A. Y.; Drezek, R. A. *Nanoscale research letters* **2011**, *6*, 428.

(173) Shields, S. P.; Richards, V. N.; Buhro, W. E. *Chemistry of Materials* **2010**, *22*, 3212.

(174) Li, Z.; Yao, C.; Wang, F.; Cai, Z.; Wang, X. *Nanotechnology* **2014**, *25*, 504005.

(175) Antonucci, P. L.; Alderucci, V.; Giordano, N.; Cocke, D. L.; Kim, H. *Journal of Applied Electrochemistry* **1994**, *24*.

(176) Chebbi, R.; Beicha, A.; Daud, W. R. W.; Zaamouche, R. *Applied Surface Science* **2009**, *255*, 6367.

(177) Qi, L.; Cheng, B.; Ho, W.; Liu, G.; Yu, J. *ChemNanoMat* **2015**, *1*, 58.

(178) Yu, R.; Chen, L.; Liu, Q.; Lin, J.; Tan, K.-L.; Ng, S. C.; Chan, H. S. O.; Xu, G.-Q.; Hor, T. S. A. *Chemistry of Materials* **1998**, *10*, 718.

(179) Powell, C. J. *Journal of Electron Spectroscopy and Related Phenomena* **2012**, *185*, 1.

(180) Powell, C. J. *Journal of Electron Spectroscopy and Related Phenomena* **2010**, *182*, 11.

(181) Brunauer, S.; Emmett, P. H.; Teller, E. *Journal of the American Chemical Society* **1938**, *60*, 309.

(182) Lin, C. H.; Lee, C. H.; Chao, J. H.; Kuo, C. Y.; Cheng, Y. C.; Huang, W. N.; Chang, H. W.; Huang, Y. M.; Shih, M. K. *Catalysis Letters* **2004**, *98*, 61.

(183) Chen, H.; Rui, Z.; Ji, H. *Industrial & Engineering Chemistry Research* **2014**, *53*, 7629.

(184) Sing, K. S. W. *Pure and Applied Chemistry* **1985**, *57*.

(185) Koga, H.; Tokunaga, E.; Hidaka, M.; Umemura, Y.; Saito, T.; Isogai, A.; Kitaoka, T. *Chemical communications* **2010**, *46*, 8567.

(186) Subero, J.; Ning, Z.; Ghadiri, M.; Thornton, C. *Powder Technology* **1999**, *105*, 66.

(187) Cammarata, R. C. *Materials Science and Engineering: A* **1997**, *237*, 180.

(188) Tao, Q.; Jursich, G.; Takoudis, C. *Applied Physics Letters* **2010**, *96*, 192105.

(189) Overhage, K.; Tao, Q.; Jursich, G.; Takoudis, C. G. *Journal of Undergraduate Research* **2011**, *4*.

(190) Sheng, W.; Gasteiger, H. A.; Shao-Horn, Y. *Journal of The Electrochemical Society* **2010**, *157*, B1529.

(191) Nugent, J. M.; Santhanam, K. S. V.; Rubio, A.; Ajayan, P. M. *Nano letters* **2001**, *1*, 87.

(192) Adanuvor, P. K. *Journal of The Electrochemical Society* **1987**, *134*, 625.

(193) Bard, A. J.; Faulkner, L. R. *Electrochemical Methods: Fundamentals and Applications*; Wiley, 2000.

(194) Huang, B.-S.; Chang, F.-Y.; Wey, M.-Y. *International Journal of Hydrogen Energy* **2010**, *35*, 7699.

(195) Li, M.; Sun, G.; Yin, P.; Ruan, C.; Ai, K. *ACS applied materials & interfaces* **2013**, *5*, 11462.

(196) Mai, L. Q.; Yang, F.; Zhao, Y. L.; Xu, X.; Xu, L.; Luo, Y. Z. *Nature communications* **2011**, *2*, 381.

(197) Liu, C.; Yu, Z.; Neff, D.; Zhamu, A.; Jang, B. Z. *Nano letters* **2010**, *10*, 4863.

(198) Kim, J. H.; Lee, K. H.; Overzet, L. J.; Lee, G. S. *Nano letters* **2011**, *11*, 2611.

(199) Yang, L.; Cheng, S.; Ding, Y.; Zhu, X.; Wang, Z. L.; Liu, M. *Nano letters* **2011**, *12*, 321.

(200) Li, J. F.; Huang, Y. F.; Ding, Y.; Yang, Z. L.; Li, S. B.; Zhou, X. S.; Fan, F. R.; Zhang, W.; Zhou, Z. Y.;

Wu de, Y.; Ren, B.; Wang, Z. L.; Tian, Z. Q. *Nature* **2010**, *464*, 392.

(201) Bae, J.; Song, M. K.; Park, Y. J.; Kim, J. M.; Liu, M.; Wang, Z. L. *Angewandte Chemie* **2011**, *50*, 1683.

(202) Dong, Y.; Yu, G.; McAlpine, M. C.; Lu, W.; Lieber, C. M. *Nano letters* **2008**, *8*, 386.

(203) Liang, W.; Yuhas, B. D.; Yang, P. *Nano letters* **2009**, *9*, 892.

(204) Pan, X.; Ren, G.; Hoque, M. N. F.; Bayne, S.; Zhu, K.; Fan, Z. *Advanced Materials Interfaces* **2014**, *1*, n/a.

(205) Manning, T. D.; Parkin, I. P. *Polyhedron* **2004**, *23*, 3087.

(206) Field, M. N.; Parkin, I. P. *Journal of Materials Chemistry* **2000**, *10*, 1863.

(207) Wang, G.; Lu, X.; Ling, Y.; Zhai, T.; Wang, H.; Tong, Y.; Li, Y. *ACS nano* **2012**, *6*, 10296.

(208) Dubal, D. P.; Aradilla, D.; Bidan, G.; Gentile, P.; Schubert, T. J.; Wimberg, J.; Sadki, S.; Gomez-Romero, P. *Scientific reports* **2015**, *5*, 9771.

(209) Zheng, J. P. *Journal of The Electrochemical Society* **1995**, *142*, 2699.

(210) Li, H.; Gao, Y.; Shao, Y.; Su, Y.; Wang, X. *Nano letters* **2015**, *15*, 6689.

(211) Mak, W. F.; Wee, G.; Aravindan, V.; Gupta, N.; Mhaisalkar, S. G.; Madhavi, S. *Journal of the Electrochemical Society* **2012**, *159*, A1481.

(212) Demarconnay, L.; Raymundo-Piñero, E.; Béguin, F. *Journal of Power Sources* **2011**, *196*, 580.

(213) Huang, S.; Wen, Z.; Zhu, X.; Gu, Z. *Electrochemistry Communications* **2004**, *6*, 1093.

(214) Ji, S.; Zhang, J.; Wang, W.; Huang, Y.; Feng, Z.; Zhang, Z.; Tang, Z. *Materials Chemistry and Physics* **2010**, *123*, 510.

(215) Yao, Y.; McDowell, M. T.; Ryu, I.; Wu, H.; Liu, N.; Hu, L.; Nix, W. D.; Cui, Y. *Nano letters* **2011**, *11*, 2949.

(216) Qu, Q. T.; Liu, L. L.; Wu, Y. P.; Holze, R. *Electrochimica Acta* **2013**, *96*, 8.

(217) Perera, S. D.; Patel, B.; Nijem, N.; Roodenko, K.; Seitz, O.; Ferraris, J. P.; Chabal, Y. J.; Balkus, K. J. *Advanced Energy Materials* **2011**, *1*, 936.

(218) Perera, S. D.; Liyanage, A. D.; Nijem, N.; Ferraris, J. P.; Chabal, Y. J.; Balkus, K. J. *Journal of Power Sources* **2013**, *230*, 130.

(219) Beidaghi, M.; Wang, C. *Advanced Functional Materials* **2012**, *22*, 4501.

(220) Pan, X.; Zhao, Y.; Ren, G.; Fan, Z. *Chemical communications* **2013**, *49*, 3943.